Towards a universal nuclear density functional

S. A. Fayans

Kurchatov Institute Russian Science Center, 123182 Moscow, Russia

A new form of the nuclear energy-density functional for describing the ground-state properties of finite nuclei up to the drip lines and beyond is proposed. The volume part in this functional is fit to the Friedman–Pandharipande and Wiringa–Fiks–Fabrocini equation of state for the UV14 plus TNI model up to densities $\rho \approx 1 \, \text{fm}^{-3}$ by a fractional expression in ρ which can be extended to higher densities while preserving causality. For inhomogeneous systems, a surface energy-density term is added, with two free parameters, which also has a fractional form like the Padé approximant containing $(\nabla \rho)^2$ in both the numerator and denominator. In addition to the Coulomb direct and exchange interaction energy, an effective ρ-dependent Coulomb-nuclear correlation term is included with one more free parameter. A three-parameter fit to the masses and radii of real nuclei shows that the latter term gives a contribution to the Coulomb displacement energy of the same order of magnitude as the Nolen–Schiffer anomaly. The first self-consistent run with the proposed functional, performed for about 100 spherical nuclei, gives rms deviations from experiment of $\approx 1.2 \, \text{MeV}$ in the masses and $\approx 0.01 \, \text{fm}$ in the radii, which are about a factor of two better than those obtained with the Skyrme functionals or with the Gogny force. The extrapolation to the drip lines lies in between the ETFSI and the macroscopic–microscopic model predictions. © *1998 American Institute of Physics.* [S0021-3640(98)00115-7]

PACS numbers: 21.60.−n, 21.10.−k

Recent progress in measuring basic nuclear properties such as nuclear masses and radii and in accumulating nuclear data is very impressive. Physics with radioactive beams has opened up a new era in experimental studies of nuclei not too far from the beta stability valley and of nuclear exotica at extreme N/Z ratios up to the drip lines and beyond. From the theoretical side, unfortunately, the present-day microscopic approaches are not able either to describe the properties of already known nuclei with sufficient accuracy to meet modern experiments or to give reliable predictions for nuclear *terra incognita*, specifically, the data needed in astrophysical applications but which are not expected to be measured in the immediate future. Among the existing approaches, the most successful are the self-consistent mean-field microscopic models based on effective energy-density functionals (EDFs) incorporating forces of the Skyrme type with zero range or of the Gogny type with finite range, and also the relativistic mean field (RMF)

model with classical meson fields. These models can give the masses and radii of measured nuclei with rms deviations from experiment no better than about 2 MeV and 0.02 fm, respectively.[1] While they may differ in the extrapolation behavior,[2] most importantly, all their predictions, even for nuclei not too far from stability, are in striking deviation from those of the macroscopic–microscopic (MM) models[3] or of the extended Thomas–Fermi model with Strutinsky integral (ETFSI).[4] These latter models are able to reproduce the measured nuclear masses and charge radii with the rms error down to ≈ 0.6 MeV and ≈ 0.02 fm, respectively, and their predictions are currently considered to be the most reliable. Such a large disagreement between the two approaches may indicate that some important physical ingredients are missing in the EDF construction, and perhaps the form of the EDF used so far in the microscopic calculations is not flexible enough to incorporate them effectively. Searches for a better parameter set for these ''old'' functionals are still continuing (see, e.g., a very recent paper[5] where the Skyrme functionals are revisited with respect to the isovector $\propto (N-Z)^2$ component, but it is hard to believe that this revision would cure the above disagreement).

In suggesting a new EDF, two issues should be kept in mind. Firstly, in changing the conventional EDF form in an attempt to improve the description of nuclear masses and radii, it is highly desirable to reach a mutually consistent result: the relative error for both these quantities should be of the same order. As one may notice, this is not the case with all available calculations, since they yield relative rms deviations for radii that are a factor of 4 worse than those for the binding energies. Secondly, it would be of great advantage if a new EDF could be used not only for nuclei throughout the nuclear chart but also for describing such objects as neutron stars, with the crystal structure in their crust. The present paper is an attempt towards such a universal nuclear density functional.

The total energy density of a nuclear system is represented as

$$\varepsilon = \varepsilon_{\text{kin}} + \varepsilon_v + \varepsilon_s + \varepsilon_{\text{Coul}} + \varepsilon_{sl} + \varepsilon_{\text{anom}}, \tag{1}$$

where ε_{kin} is the kinetic energy term which, since we are constructing a Kohn–Sham type functional, is taken with the free operator $t = p^2/2m$, i.e., with the effective mass $m^* = m$; all the other terms are discussed below.

The volume term in (1) is chosen to be in the form

$$\varepsilon_v = \frac{2}{3} \epsilon_F^0 \rho_0 \left[a_+^v \frac{1 - h_{1+}^v x_+^\sigma}{1 + h_{2+}^v x_+^\sigma} x_+^2 + a_-^v \frac{1 - h_{1-}^v x_+}{1 + h_{2-}^v x_+} x_-^2 \right]. \tag{2}$$

Here and in the following $x_\pm = (\rho_n \pm \rho_p)/2\rho_0$, $\rho_{n(p)}$ is the neutron (proton) density, and $2\rho_0$ is the equilibrium density of symmetric nuclear matter with Fermi energy $\varepsilon_F^0 = (9\pi/8)^{2/3}\hbar^2/2mr_0^2$ and radius parameter $r_0 = (3\pi\rho_0/8)^{1/3}$. Fractional expressions of the type in Eq. (2) were introduced in Ref. 6 for the EDF with application to finite systems with pairing correlations. Such expressions allow an extrapolation of the nuclear equation of state (EOS) to very high densities while preserving causal behavior. This might be of advantage, since the available microscopic nuclear-matter equations of state often violate causality at $\rho > 1$ fm^{-3}. Thus, in deriving the parameters of Eq. (2), we shall use the EOS of Refs. 7 and 8 only in a region of up to about six times the saturation density.

The four parameters in the isoscalar volume energy density $\propto a_+^v$ are fixed by fitting to the EOS of symmetric infinite nuclear matter[7,8] for the UV14 plus TNI model. The
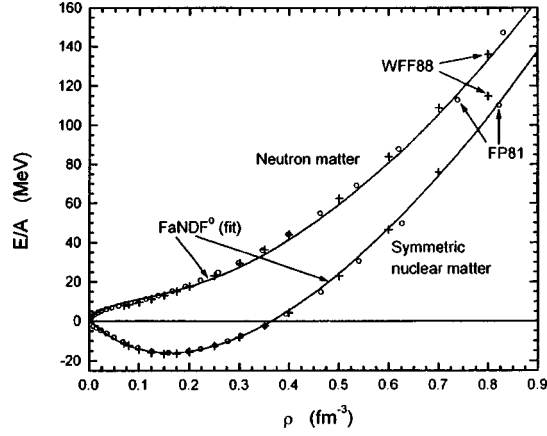
FIG. 1. Binding energy per nucleon in symmetric nuclear matter and in neutron matter. The open circles and crosses are the calculations of Ref. 7 and Ref. 8, respectively. The solid lines show the fit by fractional expressions of the type in Eq. (2).

result shown in Fig. 1 by the lower solid curve is obtained for values of the exponent $\sigma = 1/3$, compression modulus $K_0 = 220\,\text{MeV}$, equilibrium density $2\rho_0 = 0.16\,\text{fm}^{-3}$ ($r_0 = 1.143\,\text{fm}$), and chemical potential $\mu = -16.0\,\text{MeV}$ (the energy per nucleon at the saturation point). The dimensionless parameters are $a_+^v = -9.559, h_{1+}^v = 0.633, h_{2+}^v = 0.131$. Keeping them fixed, a fit to the neutron matter EOS from the same papers[7,8] is performed to determine the three parameters of the isovector part $\propto a_-^v$ in Eq. (1). The good description presented by the upper solid curve in Fig. 1 is obtained with $a_-^v = 4.428$, $h_{1-}^v = 0.250, h_{2-}^v = 1.300$. This corresponds to an asymmetry energy coefficient $\beta_0 = 30.0\,\text{MeV}$. Note that, according to our fit, the asymmetry energy decreases with ρ, changing sign at four times saturation density. Such behavior might lead to the neutron–proton separation instability in dense matter.[9]

The surface part in Eq. (1) is meant to describe the finite-range and nonlocal in-medium effects which may presumably be incorporated phenomenologically within the EDF framework in a localized form by introducing a dependence on density gradients. It is taken as follows:

$$\varepsilon_s = \frac{2}{3}\epsilon_F^0\rho_0\frac{a_+^s r_0^2(\nabla x_+)^2}{1 + h_+^s x_+^\sigma + h_\nabla^s r_0^2(\nabla x_+)^2}, \tag{3}$$

with $h_+^s = h_{2+}^v$, a_+^s and h_∇^s the two free parameters. Such a form is obtained by adding the terms $\propto(\nabla x_+)^2$ in both the numerator and denominator of the isoscalar volume energy density of Eq. (2). Alternatively, this peculiar surface term may be regarded as the Padé approximant for the (unknown) expansion in $(\nabla\rho)^2/(1 + h_+^s x_+^\sigma)$ where the form factor $1/(1 + h_+^s x_+^\sigma)$ imitates a transformation to Migdal quasiparticles (cf. Ref. 10). In fact, h_+^s is also a free parameter, but here we prefer to keep it fixed by the above condition.
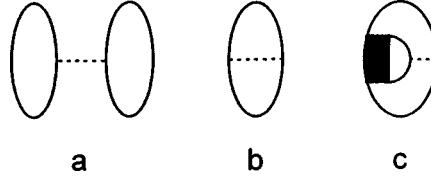
The Coulomb part in Eq. (1) is approximated by

FIG. 2. Representative diagrams that can contribute to the Coulomb-induced binding energy. Diagrams a and b correspond to the direct and exchange Coulomb terms, respectively, whereas diagram c shows the Coulomb–nuclear correlation term. The solid lines represent the nucleon (proton) Green's function, the dashed lines the Coulomb interaction, and the black square the total amplitude of NN (proton–proton) interaction.

$$\varepsilon_{\mathrm{Coul}} = 2\pi e^2 \rho_{\mathrm{ch}}(r)\left(\frac{1}{r}\int_0^r \rho_{\mathrm{ch}}(r)r^2\,dr + \int_r^\infty \rho_{\mathrm{ch}}(r)r\,dr\right) - \frac{3}{4}\left(\frac{3}{\pi}\right)^{1/3}e^2\rho_p^{4/3}(1-h_{\mathrm{Coul}}x_+^\sigma)\,,$$

(4)

where the first term, the diagram in Fig. 2a, is the direct Coulomb contribution (expressed through charge density ρ_{ch} and written, for simplicity, for the case of spherical symmetry), while the second term is the exchange part, Fig. 2b, taken in the Slater approximation and combined with the Coulomb–nuclear correlation term $\propto h_{\mathrm{Coul}}$, Fig. 2c. The latter is believed to account for the correlated motion of protons in nuclei beyond the direct (Hartree) and exchange (Fock) Coulomb interaction.[11,12]

The spin–orbit term ε_{sl} in Eq. (1) comes from the two-body spin–orbit interaction $\propto(\kappa+\kappa'\boldsymbol{\tau}_1\cdot\boldsymbol{\tau}_2)[\nabla_1\delta(\mathbf{r}_1-\mathbf{r}_2)\times(\mathbf{p}_1-\mathbf{p}_2)]\cdot(\boldsymbol{\sigma}_1+\boldsymbol{\sigma}_2)$. For spherical nuclei one gets

$$\varepsilon_{sl} = C_0 r_0^2 \sum_{i,k=n,p} \frac{1}{r}\rho_{sl}^i \kappa^{ik}\frac{d\rho^k}{dr}\,,$$

(5)

where ρ_{sl} is the spin–orbit density, $\rho_{sl}^{n;p}(\mathbf{r}) = \Sigma_\lambda n_\lambda \langle\boldsymbol{\sigma}\cdot\mathbf{l}\rangle_\lambda|\varphi_\lambda^{n,p}(\mathbf{r})|^2$; here n_λ is the occupation number of the single-particle level λ, φ_λ is its wave function, $\langle\boldsymbol{\sigma}\cdot\mathbf{l}\rangle_\lambda = j(j+1)-l(l+1)-3/4$, $\kappa^{nn}=\kappa^{pp}=\kappa+\kappa'$, $\kappa^{np}=\kappa^{pn}=\kappa-\kappa'$, and $C_0 = 2\varepsilon_F^0/3\rho_0$ is the inverse density of states on the Fermi surface ($C_0=307.2\,\mathrm{MeV}\cdot\mathrm{fm}^{-3}$). It is known from the RMF theory that the isovector spin–orbit force is very small compared to the isoscalar one.[13] Thus we set $\kappa'=0$ and derive the isoscalar strength $\kappa=0.19$ from the average description of the splitting of the single-particle states in ^{208}Pb.

The last term in Eq. (1), the anomalous energy density, is represented as

$$\varepsilon_{\mathrm{anom}} = \sum_{i=n,p} C_0 \nu^{\dagger i}(\mathbf{r})f^\xi(x_+(\mathbf{r}))\nu^i(\mathbf{r})\,,$$

(6)

where $\nu(\mathbf{r})$ is the anomalous density and $C_0 f^\xi$ is the effective force in the particle–particle channel with the dimensionless form factor[14] $f^\xi(x_+) = f_{ex}^\xi + h^\xi x_+ + f_\nabla^\xi r_0^2(\nabla x_+)^2$. The strength parameters $f_{ex}^\xi = -2.8$, $h^\xi = 2.8$ and $f_\nabla^\xi = 2.2$ are extracted from a fit to the neutron separation energies and charge radii of lead isotopes.[14]

The three parameters a_+^s, h_∇^s and h_{Coul} remain to be determined. This was done through a χ^2 fit to the masses and radii of about 100 spherical nuclei from ^{38}Ca to ^{220}Th, with the result $a_+^s = 0.600$, $h_\nabla^s = 0.440$ and $h_{\mathrm{Coul}} = 0.941$, the rms deviations being 1.2 MeV and 0.01 fm for the masses and radii, respectively. We shall call the EDF in the proposed form, with the just parameters just determined, the nuclear density functional
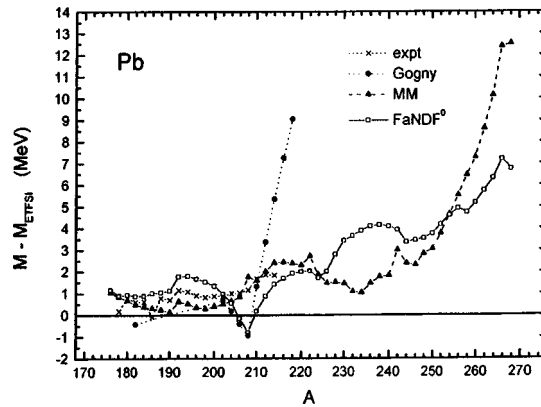
FIG. 3. Deviations of various theoretical masses from the ETFSI mass[4] for a long chain of lead isotopes. Black triangles correspond to the MM model,[3] solid dots to the Gogny force (from Ref. 2). The results obtained with FaNDF^0 are shown by open squares. The experimentally known masses including those derived from systematics[15] are presented by crosses.

FaNDF^0 (the superscript 0 means a ''zeroth'' approximation in the sense that other parameter sets FaNDF^i, $i = 2, 3, \ldots$ might be found which lead to a better fit).

Typical results of the spherical HF+BCS calculations with FaNDF^0 are shown in Fig. 3 for even Pb isotopes, from the proton drip line to the neutron drip line (47 nuclides), in comparison with experimental data and other model predictions. The ETFSI model is chosen as a reference. The nuclei in the $A \approx 222$ to 248 region might have a static deformation,[3,4] so one expects that, with a deformed code, the results for FaNDF^0 in this region will be shifted down closer to the MM or ETFSI results. Analogous calculations for tin isotopes are presented in Fig. 4. It is seen that the predictions obtained with the Gogny force just outside the measured regions are in strong disagreement with other models. Approaching the neutron drip line, the masses obtained with FaNDF^0 fall in between the MM and ETFSI predictions.
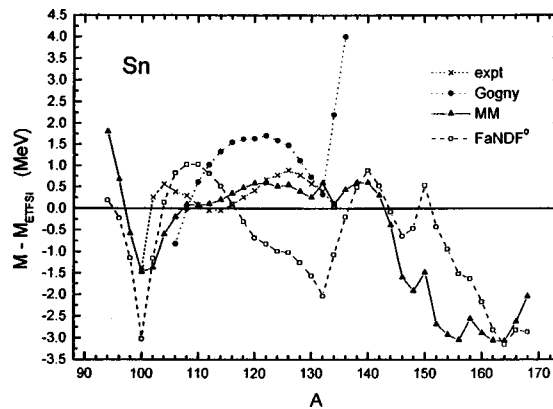
FIG. 4. The same as in Fig. 3 but for the chain of tin isotopes.

Finally, the mass differences for the mirror nuclei ^{17}F–^{17}O and ^{41}Sc–^{41}Ca calculated with FaNDF^0 in the uniform filling approximation are 3.546 MeV and 7.174 MeV, respectively, whereas the corresponding experimental values are 3.543 MeV and 7.278 MeV. In all calculations the nucleon charge form factors in the direct Coulomb term and neutron–proton mass difference in the free kinetic energy operator are always taken into account. If the Coulomb–nuclear correlation term were omitted by setting $h_{Coul}=0$, the calculated mass differences for these mirror pairs would be 3.300 MeV and 6.872 MeV, respectively, leading to a 6–7% discrepancy; this kind of discrepancy is known as the Nolen–Schiffer anomaly. It follows that Coulomb–nuclear correlations play an important role in finite nuclei. Incorporating the corresponding term in the EDF improves the description of the nuclear ground-state properties and greatly reduces the severity of the Nolen–Schiffer anomaly.

To summarize, we have shown that the agreement between the microscopic self-consistent theory and experiment is significantly improved with the proposed EDF, in which the volume part fits the microscopic EOS for infinite uniform matter, the surface term has the peculiar form given by Eq. (3), and for finite systems the Coulomb part contains an additional Coulomb–nuclear correlation term. The first results obtained with the FaNDF^0 parametrization are encouraging. The proposed construction of the EDF seems to be an important step towards a universal nuclear density functional.

[1] K. Pomorski, P. Ring, G. A. Lalazissis *et al.*, Nucl. Phys. A **624**, 349 (1997).

[2] Z. Patyk, A. Baran, J. F. Berger *et al.*, GSI-Preprint-97–40, August 1997.

[3] P. Möller, J. R. Nix, W. D. Myers, and W. J. Swiatecki, At. Data Nucl. Data Tables **59**, 185 (1995).

[4] Y. Aboussir, J. M. Pearson, A. K. Dutta, and F. Tondeur, At. Data Nucl. Data Tables **61**, 127 (1995).

[5] E. Chabanat, P. Bonche, P. Haensel *et al.*, Nucl. Phys. A **627**, 710 (1997).

[6] A. V. Smirnov, S. V. Tolokonnikov, and S. A. Fayans, Yad. Fiz. **48**, 1661 (1988) [Sov. J. Nucl. Phys. **48**, 995 (1988)].

[7] B. Friedman and V. R. Pandharipande, Nucl. Phys. A **361**, 502 (1981).

[8] R. B. Wiringa, V. Fiks, and A. Fabrocini, Phys. Rev. **38**, 1010 (1988).

[9] M. Kutschera, Phys. Lett. B **340**, 1 (1994).

[10] V. A. Khodel and E. E. Saperstein, Phys. Rep. **92**, 183 (1982).

[11] V. R. Shaginyan, Yad. Fiz. **40**, 1144 (1984) [Sov. J. Nucl. Phys. **40**, 728 (1984)].

[12] A. Bulgac and V. R. Shaginyan, Nucl. Phys. A **601**, 103 (1996).

[13] P. Ring, Prog. Part. Nucl. Phys. **37**, 193 (1996).

[14] S. A. Fayans and D. Zawischa, Phys. Lett. B **383**, 19 (1996).

[15] G. Audi and A. H. Wapstra, Nucl. Phys. A **565**, 1 (1993).

Experimental determination of the difference of the beta-decay constants for atomic and molecular tritium

Yu. A. Akulov[a] and B. A. Mamyrin

A. F. Ioffe Physicotechnical Institute, Russian Academy of Sciences, 194021
St. Petersburg, Russia

The results of an experiment measuring the difference $\Delta\lambda = \lambda_a - \lambda_m$ of the beta-decay constants of atomic and molecular tritium are reported. The difference $\Delta\lambda$ is determined by comparing the rates of growth of the relative content of radiogenic helium-3 in samples containing atomic and molecular tritium. The result $\Delta\lambda = (4.6 \pm 0.8) \times 10^{-12}\,\mathrm{s}^{-1}$ corresponds to a relative change of the decay constant by $\sim 0.26\%$. © *1998 American Institute of Physics.* [S0021-3640(98)00215-1]

PACS numbers: 23.40.−s, 33.15.−e, 32.10.−f

According to the Fermi theory of beta decay, the probability of electron emission by nuclei and the spectrum of the electrons depend on the structure of the electronic phase space accessible to the beta electron in the atomic–molecular system including the beta-active nucleus. The experimentally determined values of the fundamental parameters of a beta transition — the decay constant λ and the maximum energy of the beta spectrum — are sensitive to the state of the electronic environment of the nucleus — the so-called chemical shift of nuclear characteristics. Since the energy released in the beta decay of tritium is relatively low $({}^3\mathrm{H} \rightarrow {}^3\mathrm{He} + e^- + \tilde{\nu} + 18.6\,\mathrm{keV})$, an appreciable fraction of the virtual beta electrons is generated with wavelengths characteristic for atomic electronic systems. This leads to considerable changes in the real beta spectrum and makes the chemical shifts of the decay constant measurable. According to preliminary theoretical estimates,[1,2] the chemical shifts of the decay constant for different configurations of the electronic environment of the triton lie in the range (0.1–0.7)%. In the present letter we report the results of an experiment measuring the difference of the decay constants for atomic (λ_a) and molecular (λ_m) tritium: $\Delta\lambda = \lambda_a - \lambda_m$.

The helium differential isotopic mass-spectrometric method was used to determine $\Delta\lambda$.[3] The crux of the method consists in the fact that the rates of growth of the ratios of the content of radiogenic helium-3 to the content of helium-4 are compared for two samples, each of which contains helium-4 and some chemical compound of tritium. An important advantage of this approach is that absolute measurements are completely eliminated and the helium losses are much easier to take into account — the basic sources of the systematic error are thereby eliminated. In the case studied the experimental arrangement presupposed that two identical samples of a gas mixture containing helium-4 and molecular tritium are produced at a moment t_0 and that subsequently an action is exerted

on one of the samples so as to convert the tritium into an atomic state. Time is measured from the moment at which the pressure of molecular tritium is switched on at the entrance surface of a 0.01-cm-thick palladium membrane with an active area of 12 cm^2 and a temperature $\sim 530\,°C$. The tritium which is passed through the membrane was mixed with helium-4, after which the mixture was distributed over 350-mm-long molybdenum glass ampoules with an inner diameter of 8 mm. The tritium partial pressure in the ampoules was equal to 93 Pa, and the helium-4 partial pressure was equal to 6 Pa. Dissociation of $^3H_2$ molecules was accomplished by an rf discharge produced in the ampoule by a 1 MHz sinusoidal field with intensity $\sim 100\,V/cm$, produced by ring-shaped outer electrodes. The resonance dissociation mechanism was used to obtain thermalized free tritium atoms. In this method the energy required to break the interatomic bond in $^3H_2$ molecules is supplied by superelastic collisions (''collisions of the second kind'') in interactions with mercury atoms which are excited in the discharge up to levels 6^3P_1 and 6^3P_0. The mercury atoms are introduced into the ampoule beforehand and the mercury is evaporated by the discharge itself. The effective current in the discharge was maintained at the level $\sim 40\,mA$. The power released in the discharge was equal to 140–145 W.

The procedure for obtaining atomic tritium was simulated in special experiments with molecular protium. Mass-spectrometric and optical methods were developed to determine the degree of dissociation of the molecules. In the mass-spectrometric measurements, free hydrogen atoms flowed from the discharge cell along a fluoroplastic antire-combination channel in a free molecular flow regime into the ionization chamber of the mass spectrometer. The degree of dissociation ϵ was determined from the dependence of the current I of atomic hydrogen ions on the power P absorbed in the discharge cell. For the above-indicated values of the current and field intensity in the discharge, a horizontal plateau corresponding to nearly 100% dissociation of hydrogen was achieved on a plot of the function $I(P)$.[4] The optical method of determining ϵ was based on comparing the intensities of the monochromator-identified spectral lines of the Balmer series H_α, H_β, H_γ, and H_δ and bands with wavelengths $\sim 652\,nm$, $\sim 580\,nm$, and $\sim 410\,nm$ from the spectrum of molecular hydrogen for two regimes of the rf discharge — flow-through, in which the gas is pumped continuously through the discharge tube, and static. The residence time of a molecule in the interelectrode space was equal to 0.003–0.01 s in the flow-through regime. In this case, there is virtually no time for the hydrogen to dissociate and molecular bands predominate in the spectrum of the discharge. In the static regime (i.e., no gas flow), however, for the same pressures and power dissipated in the discharge, the intensity of the Balmer lines is 10–15 times higher, while the intensity of the molecular bands is 25 or more times lower. Comparing the coefficients of the relative change in the intensities, it can be shown that in the static discharge the degree of dissociation of hydrogen exceeds 93%. The static weights of the ionized and excited states of hydrogen in the discharge, calculated using estimates of the current, density, and energy of the electrons, did not exceed 10^{-3}%. Therefore the experimental conditions made it possible to observe the beta decay of tritium in the ground atomic and ground molecular states.

The measurement equation in the helium differential method of determining $\Delta\lambda$ for the pair ^3H atom plus $^3H_2$ molecule has the form[3]

$$\frac{(^3\mathrm{He}/^4\mathrm{He})_a}{(^3\mathrm{He}/^4\mathrm{He})_m} = \frac{\tau_a}{\tau_m}\left(k\epsilon\frac{\Delta\lambda}{\lambda_m} + 1 \right).$$

Here $(^3\mathrm{He}/^4\mathrm{He})_{m,a}$ are the mass-spectrometrically measured values of the helium isotopic ratios in samples with molecular and atomic tritium; τ_m and τ_a are the effective exposure times of the samples, and the residence time of part of the tritium in an atomic state (i.e., the discharge lifetime) is $\tau_a k$, where $k<1$ is a dimensionless factor. The time intervals τ_m and τ_a were calculated from the relations $\tau_{m,a}=(t_{m,a}-t_0)+\delta_{m,a}\eta_{m,a}$, where the time readings t_m and t_a correspond to the moments when tritium is separated from the samples; η_m and η_a are the time intervals between the readings t_m and t_a and the moment when helium isotopic ratios in the samples are measured; and, δ_m and δ_a are the relative residual specific activities of tritium, determining the rate of accumulation of helium-3 in the ''molecular'' and ''atomic'' samples during the time intervals η_m and η_a. The tritium was separated from the samples during the interaction of the gas mixture with the palladium membrane, similar to membrane used when the ampoules were filled. The uncertainty in the reference time t_0, just as in the values of t_m and t_a, did not exceed 8 s. The relative residual activity due to incomplete removal of tritium through the membrane was measured with an internal-fill proportional counter with sensitivity $\sim 10^6$ tritium atoms[5] and was equal to $\delta_m=0.00115$ and $\delta_a=0.00095$ of the initial specific activity of the mixture. The permeability of palladium membranes for helium and other factors determining the nonradiogenic variation in the ratio $^3\mathrm{He}/^4\mathrm{He}$ in mixtures were monitored with a mass spectrometer with a sensitivity with respect to $^3\mathrm{He}$ of $\sim 3\times 10^4$ atoms.[6] The amount of helium-3 formed in samples during their exposure time exceeded 2×10^{13} atoms. Therefore the possible systematic errors due to helium leaks were detected at the level $\sim 10^{-6}\%$.

The ratios of the helium isotopes in the samples, close to 0.001 in absolute value, were measured with a modified MI-1201 two-beam isotopic mass spectrometer.[7] The $^3\mathrm{He}^+$ and $^4\mathrm{He}^+$ ion currents were measured with continuous evacuation of the mass spectrometer chamber by a titanium getter pump, which stabilized the background content in the apparatus of hydrogen molecules with mass number 3 ($^1\mathrm{H}^2\mathrm{H}$, $^1\mathrm{H}_3$) at the level 10^{-3} of the $^3\mathrm{He}$ content in a single admission. Five series of measurements were performed. In each series, samples of a helium mixture from ''molecular'' and ''atomic'' samples were successively admitted into the chamber. As a result, the value 0.90257 with a standard deviation of 0.00021 was obtained for the ratio $(^3\mathrm{He}/^4\mathrm{He})_a/(^3\mathrm{He}/^4\mathrm{He})_m$ from the left-hand side of the measurement equation. The effective exposure times were $\tau_m=271.80$ min and $\tau_a=244.90$ min; the coefficient $k=0.70$, i.e., the discharge was maintained for 171 min. The degree of dissociation ϵ was taken to be $0.95^{+0.05}_{-0.02}$.

The ratio $\Delta\lambda/\lambda$, determined from the measurement equation with the above-indicated values of the parameters entering in the equation, equals 0.00257 ± 0.00045. The error in the result, corresponding to one standard deviation, was determined by a quadratic form which included the variances of all parameters of the measurement equation. The variance of the ratio τ_a/τ_m was calculated taking account of the 95% positive correlation of the random quantities t_m and t_a, which is due to the fact that identical procedures were used to remove tritium from both samples. To calculate, on the basis of the measured relative shift of the decay constant, the absolute value of the difference $\Delta T_{1/2}$ of the half-lives of molecular and atomic tritium, it is best to use the value $T_{1/2m}$

$=(12.296 \pm 0.017)$ yr — the weighted-mean of the latest two published estimates of the half-life for molecular tritium, which also agree well with one another. One of these estimates was obtained by the isotopic-helium method[8] and the other was obtained from the decay curve obtained by the bremsstrahlung detection method.[9] Since $\Delta T_{1/2}/T_{1/2} = -\Delta\lambda/\lambda$ for $\Delta\lambda/\lambda \ll 1$, we find $T_{1/2m} - T_{1/2a} = (0.0316 \pm 0.0055)$ yr $= (11.5 \pm 2.0)$ days. We obtain for the absolute value of the difference of the decay constants λ_a and λ_m

$$\Delta\lambda = \lambda_a - \lambda_m = \frac{\ln 2}{T_{1/2m}}(0.00257 \pm 0.00045) = (4.6 \pm 0.8) \times 10^{-12}\,\mathrm{s}^{-1}.$$

Methods of fast tritiation of different hydrogen-containing compounds are being developed on the basis of the method developed for obtaining, stabilizing, and performing diagnostics on atomic hydrogen. This will make it possible to measure the chemical shifts of the decay constant for a wide class of atomic–molecular systems. The experiment determining $\Delta\lambda$ in molecular–atomic tritium vapor showed that the accuracy achievable in measurements of the chemical shifts of the decay constant by the helium differential isotopic mass-spectrometric method is sufficient for determining the role of diverse through which the electronic cloud surrounding the beta-active nucleus influences the beta electron, and therefore separate beta-electron production channels can be studied theoretically: decay in bound states, screening of the nuclear charge by atomic electrons, excitation of atomic electrons, exchange effect. The goal of the development of precision measurement methods and an adequate technique for calculating the chemical shifts of the decay constant is to construct on the basis of the chemical shift a new method for determining the energy and spatial characteristics of electronic states in atomic–molecular and other quantum-size systems.

[a])e-mail: akulov@mass.ioffe.rssi.ru

[1] E. G. Drukarev and M. I. Strikman, Zh. Éksp. Teor. Fiz. **91**, 1160 (1986) [Sov. Phys. JETP **64**, 686 (1986)].
[2] B. Budick, Phys. Rev. Lett. **51**, 1034 (1983).
[3] Yu. A. Akulov, B. A. Mamyrin, and P. M. Shikhaliev, Pis'ma Zh. Tekh. Fiz. **19**(18), 72 (1993) [Tech. Phys. Lett. **19**(9), 594 (1993)].
[4] Yu. A. Akulov, B. A. Mamyrin, and P. M. Shikhaliev, Zh. Tekh. Fiz. **67**(5), 140 (1997) [Tech. Phys. **42**, 584 (1997)].
[5] B. A. Mamyrin, Yu. A. Akulov, L. V. Khabarin, and V. S. Yudenich, Prib. Tekh. Éksp., No. 2, 151 (1982).
[6] Yu. A. Akulov, B. A. Mamyrin, L. V. Khabarin, and V. S. Yudenich, Prib. Tekh. Éksp., No. 2, 173 (1985).
[7] Yu. A. Akulov, B. A. Mamyrin, and P. M. Shikhaliev, Prib. Tekh. Éksp., No. 3, 114 (1995).
[8] Yu. A. Akulov, B. A. Mamyrin, L. V. Khabarin *et al.*, Pis'ma Zh. Tekh. Fiz. **14**, 940 (1988) [Sov. Tech. Phys. Lett. **14**, 416 (1988)].
[9] B. Budick, J. Chen, and H. Lin, Phys. Rev. Lett. **67**, 2630 (1991).

Translated by M. E. Alferieff

Shift and broadening of hadronic resonances formed in nuclear interactions

D. V. Dobrokhotov, V. M. Kolybasov, and I. S. Shapiro
P. N. Lebedev Physics Institute, Russian Academy of Sciences, 117924 Moscow, Russia

The mass shift and broadening of the isobar $\Delta(1232)$ formed in the reaction $^{12}C(p,n)\Delta^{++}\,^{11}B^*$, are explained by taking into account the elastic and inelastic rescattering of the isobar decay products by the residual nuclear system. The computational results for the mass decrease and broadening of the peak are in good agreement with the experimental data. Predictions are given for a process of the same type on the deuteron, $pd \rightarrow nn\Delta^{++}$. © *1998 American Institute of Physics.*
[S0021-3640(98)00315-6]

PACS numbers: 25.40.Ep, 27.20.+n

Recent investigations of the production of wide resonances in nuclear interactions conducted in an exclusive or semiexclusive arrangement[1–4] have shown that in a number of cases the observed parameters of the resonance (the position of the maximum and the shape and width of the line) differ appreciably from the parameters of a free resonance. It seems likely that the simplest and most universal reason is that a resonance with a width greater than several tens of MeV decays predominantly within the range of the nuclear forces, and the products of its decay are highly likely to interact with the residual nuclear system, transferring part of the energy and momentum to it; this decreases the observed mass and broadens the peak.

The problem of the properties of hadronic resonances formed in nuclear reactions has attracted in recent years the attention of theorists, and there are a large number of publications concerning this question (see Refs. 5 and 6 and the references cited there). Even a brief review of the corresponding theoretical models and results falls outside the scope of the present letter. We note only that most of them are based on the idea of a change in the effective mass of the hadron, propagating (before decaying) in the nuclear medium, on account of the interaction with the surrounding matter. We shall employ a completely different approach. Since the transit time of a wide hadronic resonance in a nucleus is of the same order of magnitude as the lifetime, to a first approximation we neglect the change in its properties as a result of collisions with the nucleons in the nucleus. The only, and seemingly the most important, dynamical effect that will be taken into account is the interaction of the decay products of a resonance with the residual nuclear system. In other words, we proceed from the fact that the physical nature of the observed shift does not signify a change in the position of the pole in the production

amplitude as a result of hadron-nuclear interaction and that it is a simple consequence of the interaction of the decay particles with the spectator nucleus.

The effect mentioned above has been observed in the reaction whereby the stopped antiprotons are captured by deuterons $\bar{p}d \rightarrow p_s 2\pi^+ 3\pi^-$ (Ref. 3), where a peak is present in the mass distribution of the system $(2\pi^+ 2\pi^-)$ (the so-called resonance $\zeta(1480)$ or $X(1500)$, possibly a $\bar{p}n$ bound state). The surprise was that the position of the peak was substantially different for small ($p_s < 200$ MeV/c) and large ($p_s > 200$ MeV/c) momenta of the spectator proton. The shift was equal to about 120 MeV. Both the appreciable high-momentum ''tail'' in the momentum distribution of the spectator and the shift and broadening of the peak in the mass spectrum of the system $(2\pi^+ 2\pi^-)$ in different regions of the momentum of the final proton were successfully explained in Ref. 7 in a model of a quasifree $\bar{p}n$ capture and rescattering of one of the pions from the decay of $X(1500)$ by the proton. The idea was that the pion gives up a portion of its energy and momentum to the spectator proton, as a result of which the invariant mass of the system $(2\pi^+ 2\pi^-)$ becomes smaller by an amount of the order of 120–140 MeV. This interpretation was later confirmed by new data on $\bar{p}d$ capture,[8] where a Δ-isobar peak was observed in the mass distribution of $(\pi^+ p)$, in agreement with the theoretical predictions[9] obtained in the same model.

There arises the conjecture that this is a universal effect for all wide resonances produced in nuclear interactions. It is natural to raise the question of whether or not the effect appears for the best known of these resonances — the Δ isobar. To find the answer to this question was the main goal of our investigation. There exists a large quantity of data on the inclusive spectra of tritons and neutrons from the reactions (^{3}He, t) and (p,n) in the region of Δ excitation of nuclei.[10] For our purposes, we require data on exclusive or semiexclusive investigations with simultaneous detection of both products of the decay $\Delta(p + \pi^+)$. There are few such data, and the best data are apparently for the process $p + {}^{12}\text{C} \rightarrow n + p + \pi^+ \ldots$ at 1.5 GeV/c,[1] where it was found that the distribution over the invariant mass of the system $(\pi^+ p)$ differs substantially from the case of the reaction on hydrogen. In what follows we shall examine the reaction on ^{12}C, we shall compare the theoretical results with the data of Ref. 1, and we shall give theoretical predictions for the case of the deuteron.

We underscore that the question investigated here (distribution over the invariant mass of the system $\pi^+ p$) is considerably different from the question investigated in Refs. 6 (distribution of the missing triton or neutron mass). These are completely different distributions, entailing different physics. This is especially well illustrated by the radical change in the form of the spectrum of neutrons and tritons accompanying the transition from one channel of the reaction (^{3}He, t) or (p,n) to other channels.[1,2] We note that the distribution over the invariant mass of the system πp has not been previously investigated either at the quantitative or semiquantitative levels.

We begin by presenting the formulas for the most transparent case — a deuteron, examining the contribution of the pole diagram (Fig. 1a) and the diagram with rescattering of the pion (Fig. 1b). (The rescattering of the pion is the most important process, since the pion is located in the resonance region, where the pion–nucleon cross section is several times greater than the nucleon–nucleon cross section.) The amplitude M_{pol}, corresponding to Fig. 1a, can be represented in the form
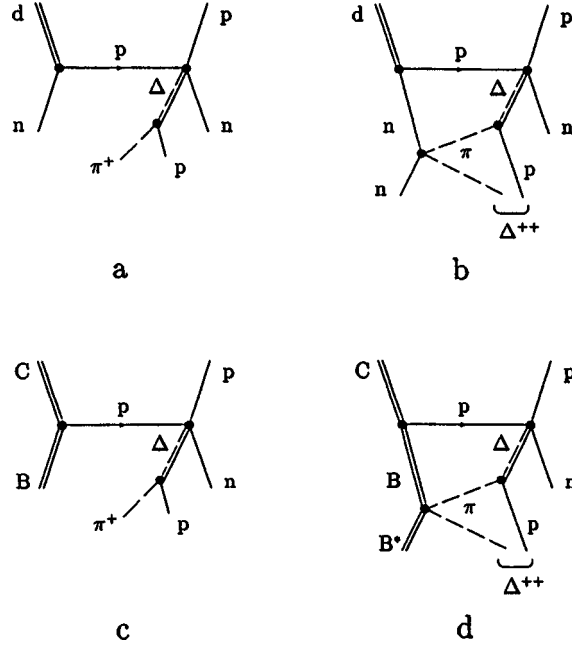
FIG. 1. Diagrams of the processes $d(p,n)\Delta^{++}n$ (a,b) and $^{12}C(p,n)B^*\Delta^{++}$ (c,d).

$$M_{\text{pol}} = \varphi_d(p_s) M_1 , \tag{1}$$

where M_1 is the amplitude of the process $pp \to n\Delta^{++}$, p_s is the momentum of the spectator, and $\varphi_d(p)$ is the wave function of the deuteron in momentum space. Using the expressions from Ref. 7 and the method of Ref. 11 to transform the integral of a triangular diagram and using the form of the pion–nucleon amplitude in the Δ-resonance region, we can represent the squared amplitude (Fig. 1b) in the form

$$|M_\triangle|^2 = \frac{\pi}{2} \frac{(\varepsilon_s + \varepsilon_{pi})^2}{(m_n + \varepsilon_{pi})^2} \frac{\sigma_{\pi^+ n}(1 + 3\cos^2\theta)}{k^2} |M_1|^2 |I_\triangle|^2 , \tag{2}$$

where θ and k are, respectively, the angle between the initial deuteron and the final pion and the momentum of the pion in the center-of-mass system of the $\pi^+ n$ system, $\sigma_{\pi^+ n}$ is the total cross section of the interaction $\pi^+ n$, ε_s and ε_{pi} are the energies of the spectator and final pion, m_n is the nucleon mass, and

$$I_\triangle = \int \varphi_d(r) j_1\left(\frac{Qr}{2}\right) \left\{ (1 - ikr)e^{ikr} - \left(1 + \frac{r}{a}\right)e^{-r/a} \right\} dr; \tag{3}$$

$\varphi_d(r)$ is the wave function of the deuteron, normalized to 1, j_1 is a spherical Bessel function, and a is a parameter appearing in the parametrization of the width Γ of the Breit–Wigner Δ-resonance amplitude:

$$\Gamma = 2\gamma \frac{(ka)^3}{(1 + (ka)^2)^2} . \tag{4}$$

Fitting free $\pi^+ n$ scattering gives $\gamma = 195$ MeV, $a = 5.7 \times 10^{-3}$ MeV^{-1} and 1225 MeV for the mass of the Δ resonance. Using also the parametrization of the Paris wave function of the deuteron in the form[12]

$$\varphi_d(r) = \sum C_n \frac{e^{-m_n r}}{r}, \tag{5}$$

the integration in Eq. (3) can be performed explicitly:

$$I_\triangle = 2\sum_n C_n \left\{ \frac{m_n^2 - 1/a^2 + Q^2/4}{Q^2} \arctan\left(2\frac{m_n + 1/a}{Q} \right) \right.$$

$$\left. - \frac{m_n^2 + k^2 + Q^2/4}{Q^2} \arctan\left(2\frac{m_n - ik}{Q} \right) \right\}. \tag{6}$$

We have now obtained expressions for the squared amplitudes (2), (3), and (6) and we can calculated any distribution in the phase space of the reaction by the Monte Carlo procedure.[13]

In the case of the formation of a Δ isobar on ^{12}C nucleus, the diagrams in Figs. 1c and 1d must be taken into account. In contrast to the deuteron case, in Fig. 1d the pion can be rescattered by the residual nuclear system not only elastically but also inelastically with excitation of discrete levels or the continuous spectrum (i.e., with breakup of the residual nucleus). Such inelastic processes are very important. To perform a strict calculation it is necessary to know the angular distributions of the inelastic scattering of pions by the ^{11}B nucleus (or closed nuclei) for different excitation energies. Unfortunately, data on these processes are incomplete (see, for example, Ref. 13). As a result, our results must be viewed as preliminary estimates. We took account of three components: (i) quasifree production of a Δ^{++} plus elastic scattering of the pion; (ii) inelastic rescattering of a pion by the residual nucleus with excitation of discrete levels with average excitation energy of about 15 MeV; and, (iii) inelastic scattering with excitation of states of the continuous spectrum with average excitation energy of about 65 MeV. The relative contributions of these components were treated as free parameters. We employed an oscillator wave function of the ^{12}C nucleus with the parameter $p_0 = 120$ MeV/c. The amplitude of the elementary process $p + p \to n + \Delta^{++}$ was assumed to be constant, i.e., the amplitude of the entire process $p + p \to n + p + \pi^+$ contains only a pole responsible for Δ and the corresponding form factor. Despite its simplicity, such an amplitude gives a good description of the data on the invariant-mass distribution of the system $\pi^+ p$ for the reaction on hydrogen (see Fig. 2a).

The computational results for the invariant-mass distribution for the pion and proton for the case of carbon are presented in Fig. 2b. The contributions of three components are shown: quasifree production of the isobar plus elastic scattering of the pion (dotted curve); same with rescattering of the pion by the residual nucleus with excitation of discrete levels (dashed curve); same for inelastic scattering in the continuous spectrum (dot-dashed curve). The ratio of the areas under the dotted, dashed, and dot-dashed curves are consistent with existing data on inelastic pion–nuclear scattering.[14] The solid curve shows the total theoretical result and describes the experimental data very well. Therefore the proposed interpretation is entirely plausible. We note that the SATURN data for the
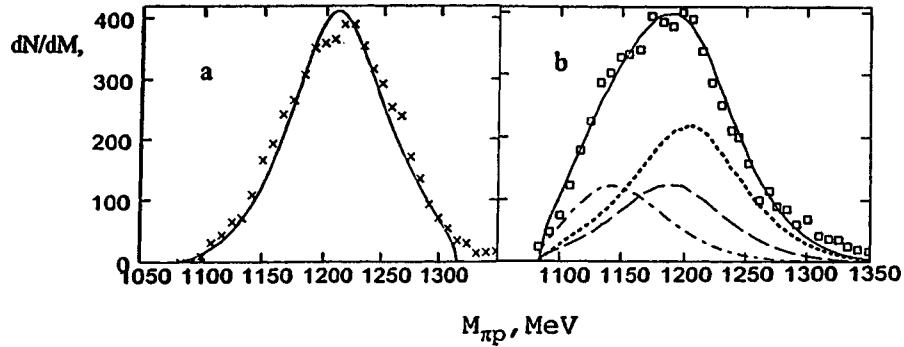
FIG. 2. Mass distribution of the system $\pi^+ p$ for the reactions $H(p,n)\Delta^{++}$ (a) and $^{12}C(p,n)B^*\Delta^{++}$ (b). Data from Ref. 1. The solid curve for case b is the total theoretical curve. The meaning of the other curves is explained in the text.

process $^{12}C(^3He,\ t)\Delta^{++}\ \dots$ also show an appreciable shift of the position of Δ^{++} in the direction of smaller masses.[2] Of course, it would be interesting to study in the future the additional influence of the nuclear medium on the mass distribution of $(\pi^+ p)$, though it is unlikely to be large because of the short lifetime of the isobar.

In the case of reactions leading to the formation of a Δ isobar, many questions can be solved more easily by investigating the charge-exchange reaction (p,n) on a deuteron, for example, the reaction $d(p,n)np\pi^+$, since here the theoretical estimates are more transparent (see diagrams in Figs. 1a and 1b and Eqs. (2)–(6)). The inclusive neutron spectrum from such a process was studied earlier in Ref. 15 (πp mass distribution was not investigated). It was shown there that the (πp) channel makes the dominant contribution to the cross section, which confirms once again the dominant role of the processes in Fig. 1a and 1b. Our theoretical predictions are presented in Fig. 3. Figure 3a shows the momentum distribution of the spectator on a logarithmic scale. The dotted curve represents the contribution of the pole graph in Fig. 1a, while the continuous curve represents
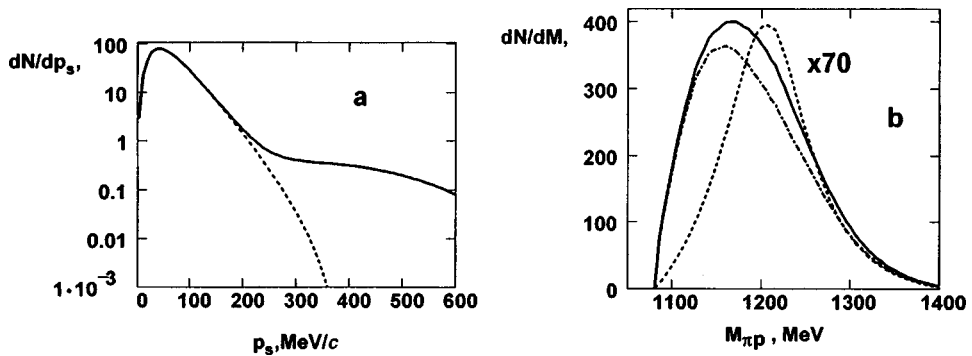

FIG. 3. Theoretical predictions for the process $pd \rightarrow nn\Delta^{++}$: a) spectator momentum distribution on a logarithmic scale. The dotted curve shows the contribution of the pole diagram in Fig. 1a; the solid curve is the total contribution of the diagrams in Figs. 1a and 1b. b) $\pi^+ p$ mass distribution. The meaning of the curves is explained in the text.

the total contribution of the diagrams in Figs. 1a and 1b. One can see that the tail in the momentum distribution, containing about 2% of all events, is determined completely by the contribution of the pion rescattering process, which predominates for spectator momenta greater than 230 MeV/c. It is obvious that a clear shift of the maximum and change in the shape of the mass distribution of the system $\pi^+ p$ can be observed only for $p_s > 230$ MeV/c. Figure 3b shows the mass distribution of $\pi^+ p$. The dotted curve corresponds to the pole diagram of Fig. 1a, the dot-and-dash curve corresponds to the diagram of Fig. 2b for events with spectator momentum $p_s > 230$ MeV/c, while the solid curve corresponds to the total contribution of the diagrams in Figs. 1a and 1b with the same limit on the spectator momentum. We note that the total curve for momenta $p_s > 300$ MeV/c will be virtually identical to the dot-and-dash curve in Fig. 3b. We note that the downward shift of the maximum by 50 MeV agrees with simple semiquantitative estimates of the average energy transfer from the pion to the spectator.[7] Estimates show that under the kinematic conditions of Ref. 1 the total cross section corresponding to the dot-and-dash curve in Fig. 3b will be of the order of several tens of μb.

In closing, we note that the proposed simple interpretation enabled us to obtain a good description of the exclusive formation of Δ in the reaction (p,n) on ^{12}C nucleus. This shows that we are dealing here with a universal physical phenomenon, which can provide new possibilities for studying nuclear structure and reaction mechanisms. The same effect is most likely observed in ρ meson production[4] and in the suppression near the threshold production of ω-mesons.[16]

[1] J. Chiba *et al.*, Phys. Rev. Lett. **67**, 1982 (1991).

[2] T. Hennino *et al.*, Phys. Lett. B **283**, 42 (1992).

[3] S. Ahmad *et al.*, in *Physics at LEAR with Low Energy Antiprotons* (*Proceedings of the Fourth LEAR Workshop*, Villars-sur-Ollon, Switzerland, 6–13 September 1987), edited by C. Amsler, *et al.*, Harwood, New York, 1988, p. 447.

[4] G. L. Lolos *et al.*, Phys. Rev. Lett. **80**, 241 (1998).

[5] V. I. Eletsky and B. L. Ioffe, Phys. Rev. Lett. **78**, 1010 (1997).

[6] F. Osterfeld *et al.*, Rev. Mod. Phys. **64**, 491 (1992); T. Udagava *et al.*, Phys. Rev. C **49**, 3162 (1994); P. Fernandez de Cordoba *et al.*, Nucl. Phys. A **592**, 472 (1995); B. Kërfgen *et al.*, Phys. Rev. C **55**, 1819 (1997).

[7] V. M. Kolybasov, I. S. Shapiro, and Yu. N. Sokolskikh, Phys. Lett. B **222**, 135 (1989).

[8] OBELIX Collaboration, Nucl. Phys. A **585**, 577 (1995); Phys. Lett. B **403**, 177 (1997).

[9] D. V. Voronov and V. M. Kolybasov, JETP Lett. **57**, 162 (1993); V. M. Kolybasov, I. S. Shapiro and D. V. Voronov, in *Mesons and Nuclei at Intermediate Energies*, World Scientific, 1995, p. 749.

[10] C. Gaarde, Annu. Rev. Nucl. Part. Sci. **41**, 187 (1991); E. A. Strokovskiĭ, F. A. Gareev, and Yu. L. Ratis, Fiz. Elem. Chastits. At. Yadra **24**, 603 (1993) [Phys. Part. Nuclei **24**, 255 (1993)].

[11] V. M. Kolybasov, FIAN Preprint No. 42 [in Russian], P. N. Lebedev Physics Institute, Russian Academy of Sciences, Moscow, 1997; Yad. Fiz., in press.

[12] M. Lacombe *et al.*, Phys. Lett. B **101**, 139 (1981).

[13] E. Byckling and K. Kajantie, *Particle Kinematics*, Wiley, New York, 1973.

[14] C. H. Q. Ingram, Nucl. Phys. A **374**, 319c (1982).

[15] C. A. Mosbacher and F. Osterfeld, Phys. Rev. C **56**, 2014 (1997).

[16] R. Wurzinger *et al.*, Phys. Rev. C **51**, 443 (1995).

Translated by M. E. Alferieff

Separation of positive and negative muons in a giant shower by the geomagnetic field

E. E. Antonov, L. G. Dedenko, and Yu. P. Pyt'ev

Department of Physics, M. V. Lomonosov Moscow State University, 119899 Moscow, Russia

A. V. Glushkov, M. I. Pravdin, and I. E. Sleptsov

Institute of Space Physics and Aeronomy, Siberian Branch of the Russian Academy of Sciences, 677891 Yakutsk, Russia

T. M. Roganova and G. F. Fedorova

Scientific and Research Institute of Nuclear Physics, M. V. Lomonosov Moscow State University, 119899 Moscow, Russia

The separation of positive and negative muons in a giant shower by the geomagnetic field is observed at a very high level of significance 0.03%. This result is obtained by interpreting in terms of the quark–gluon string model the indications of all detector stations that were triggered in this shower (which was detected at the Yakutsk array) on the basis of calculations of the responses of these stations both with and without taking the Earth's magnetic field into account. © *1998 American Institute of Physics.* [S0021-3640(98)00415-0]

PACS numbers: 13.85.Tp, 96.40.Tv

1. INTRODUCTION

The observation of giant atmospheric showers (GASs) with energies above $\sim 10^{20}$ eV[1–3] is extremely interesting for elementary particle physics and astrophysics. This energy range lies beyond the threshold for the ''cutoff'' of the cosmic ray energy spectrum on account of the interaction of protons (or nuclei) with the relic microwave photons (according to the Greisen–Zatsepin–Kuz'min idea, see Refs. 4 and 5).

Estimates of the energy of particles in the primary cosmic radiation (PCR) that generate GASs provide evidence for the possible existence of either unusually efficient mechanisms of acceleration of charged particles all the way up to energies $\geq 3 \times 10^{20}$ eV or new, unknown generation processes, for example, decays of hypothetical superheavy particles and topological defects (superconducting cosmic strings, and so on) or annihilation processes (magnetic monopoles).[6] The arrival directions of GASs indicate possible sources of generation of superhigh-energy particles, since for such particles the deviations from rectilinear propagation in the known intergalactic magnetic fields are small.

Investigations of the nature of the particles with giant energies are extremely inter-

esting. Possible candidates are protons, iron nuclei, cosmic neutrinos, γ rays (one primary γ ray splits in the geomagnetic field outside the atmosphere into a broad spectrum of secondary γ rays and electrons with energies $\sim 10^{18}$ eV). These primary particles generate in the atmosphere cascades of secondary particles with different positions of the maximum and different widths of the cascade curve, with different angular distributions of the shower axes relative to the vertical direction, and so on. Investigations of the interactions of the particles in the PCR with the atomic nuclei in air at such extreme energies could yield unique information for elementary-particle physics.

The experimental data on extensive atmospheric showers can be interpreted on the basis of a definite model of the interaction of hadrons at superhigh energies and various assumptions about external factors influencing the dynamics of shower development. It has been shown in many works (see, for example, Ref. 7) that the quark–gluon string model[8] makes it possible to give a good description of the experimental data. Specifically, it was demonstrated in Refs. 9 and 10 that the quark–gluon string model gives agreement between the calculations and experimental data on the muon component of showers detected at the Yakutsk extensive atmospheric shower array in a wide range of PCR particle energies.

An important aspect of the detailing of the model of shower development is the calculation of the distributions of the transit times of particles through a detector.[11] The average delay time and the width of the shower front at different distances from the axis depend on the position of the shower maximum and the nature of the primary particle. For this reason, the correlation between the computed and experimental values of the temporal parameters of a shower provides an additional test of the computational model for hadronic interactions and conjectures about the nature of the primary particle. Moreover, the interpretation of the experimental data in the time channel on the basis of the computed spatiotemporal structure of the shower front by the minimum-χ^2 and minimax methods[12,13] makes it possible to decrease severalfold the error in determining the shower arrival direction.

At the same time, improvements in experimental techniques and the accumulation of statistical data on the showers detected place increasingly higher demands on the accuracy of calculations of the shower parameters, the degree of detailing of the dynamics of the development of secondary-particle cascades, and taking account of external factors (for example, the Earth's magnetic and electric fields) that influence the distribution of the detected charged particles in the plane of the array. Deflections in the magnetic field destroy the azimuthal symmetry of the spatial distribution of the charged particles and change the dependence of their density on the distance from the shower axis,[9] which directly influences estimates of the energy of the primary particle. It is certainly of practical interest to correlate an improved model of shower development with the experimental data. However, it should be kept in mind that a large increase in computational time is required in order to take account of the geomagnetic field. For this reason, many years have passed from the time when the possible influence of the geomagnetic field on the spatial distribution of muons was first mentioned[14] to implementation in practice.

In the present letter the data for the most intense shower detected on the Yakutsk array[1] are interpreted taking account of the measured geomagnetic field and the spatiotemporal structure of the shower front, calculated in the quark–gluon strong model, from a primary proton. It is demonstrated that muons are separated according to the sign

of their charge by the earth's magnetic field in extensive atmospheric showers.

2. COMPUTATIONAL METHODS AND INTERPRETATION

In the quark–gluon string model[8], a matrix of 80×80 elements was calculated by a hybrid method[15] for muons which enter a 50×50 m cells in the array plane. Thus the total area for whose cells the muon density was known equals 4×4 km. The calculation was performed by the method of groups[9] on a grid of directions of motion of the muons relative to the shower axis (80×80 elements), energies of the muons (30 elements), and depths (50 elements). The average values for each group — an element of a four-dimensional array — determine the energy E_μ of a muon, the altitude h at which the muon was generated, and the direction of flight (zenith angle θ and azimuthal angle ϕ) relative to the shower axis. The number of muons with such parameters in each group was determined by solving cascade equations. Therefore all muons produced in a shower were divided into groups in accordance with the parameters determined above. The direction of the GAS axis[1] was refined as a result of interpretation of the experimental data by the minimum-χ^2 and minimax methods[12,13] on the basis of the computed spatiotemporal structure of the shower front. For each group of muons from the four-dimensional array, the relativistic Newton's equation

$$m_0 \gamma \frac{d\mathbf{V}}{dt} = e(\mathbf{V} \times \mathbf{B}),$$ (1)

where m_0 is the muon mass, γ is the Lorentz factor, e is the charge, $\mathbf{V}$ is the velocity, and $\mathbf{B}$ is the magnetic field, was solved. The equation (1) was solved taking account of the ionization losses, i.e., the Lorentz factor γ and the velocity $\mathbf{V}$ decreased as the muons propagated in the atmosphere.

At the location of the Yakutsk array the modulus of the magnetic field is $|\mathbf{B}| = 0.6$ G and the field has a declination of $19°$ westward from the northward direction and an inclination of $76°$. Control calculations were performed for the case when the geomagnetic field is neglected ($B = 0$). The indications of the detector stations were interpreted by the minimum-χ^2 method in two models (with and without the magnetic field).

3. COMPUTATIONAL RESULTS AND CONCLUSIONS

Figure 1 illustrates the separation of the positively and negatively charged muons in the GAS by the Earth's magnetic field:[1] The solid curves show the lines of constant density for positive muons, while the dashed lines correspond to negative muons. The arrows indicate the projection of the magnetic field $\mathbf{B}$ and the shower axis on the array plane. The separation of the positively and negatively charged muons is obvious. One can see that, in the first place, the centers of the distributions are displaced relative to one another by 125 m and, in the second place, more importantly, the curves at large distances from the shower axis, for example, for density $\rho_\mu = 10$ m^{-2}, are shifted leftward and upward for negative muons and rightward and downward for positive muons by 600–700 m. Quantitatively, the separation of positively and negatively charged muons at different points on the array plane can be characterized by a quantity k defined as the ratio of the difference and sum of the densities of muons with different signs at a prescribed point:

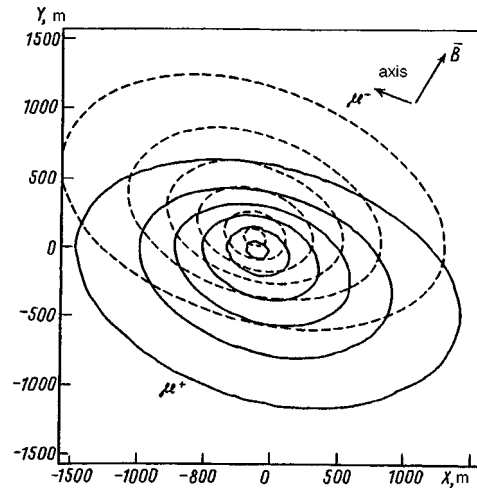$$k = (\rho_{\mu^+} - \rho_{\mu^-}) / (\rho_{\mu^+} + \rho_{\mu^-}).$$ (2)

FIG. 1. Constant density contours for positive (solid curves) and negative (dashed curves) muons in a GAS.

Curves of constant values $k=$ const are displayed in Fig. 2. In the case $|k| \geqslant 0.33$ the density of muons of one sign is at least two times higher than that of the other sign, while for $|k| \geqslant 0.82$ the fraction of muons of the one sign is less than 10%. One can see from Fig. 2 that at distances $r \geqslant 300$ m from the projection of the shower axis on the array plane $|k| \geqslant 0.3$, i.e., the separation of positively and negatively charged muons is already considerable. This muon separation effect would have been discovered a long time ago, if measurements of the sign of the charge of the particles had been performed. However, such measurements are not made at the modern arrays. For this reason, at the present time the separation effect can be observed only according to changes in the distribution of the density of all particles in the detector plane as compared with the symmetric pattern that is expected in the case when the geomagnetic field is neglected.
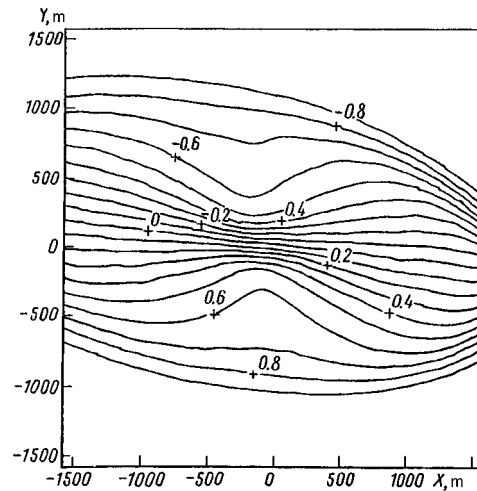

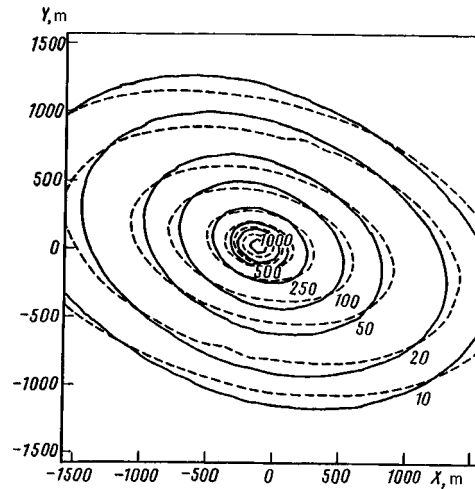FIG. 2. $k=$ const contours (see Eq. (2)) in a GAS.

FIG. 3. Constant muon density contours calculated taking account of (solid curves) and neglecting (dashed curves) the geomagnetic field in a GAS.

Figure 3 shows the contours of constant muon density, calculated taking account of (solid curves) and neglecting (dashed curves) the Earth's magnetic field. The numbers on the curves are the values of the muon density. One can see that near the shower axis the density maximum is greatly ''smeared'' by the magnetic field — the smallest continuous ring (i.e., of maximum density) lies inside the closest dashed ellipse. At large distances from the axis the eccentricity of the ''continuous'' ellipses is much smaller than for the ''dashed'' ellipses — the spatial distribution of the muons in a direction perpendicular to the projection of the axis on the array plane becomes wider. It is obvious that at the observation level chosen for comparison, the GAS should consist of essentially muons of the same sign and many detectors must be triggered in order to have the most complete information about the spatial distribution of muons in the array plane. Moreover, the shower axis should be approximately perpendicular to the direction of the magnetic field. The inclined GAS detected at the Yakutsk array satisfies all these conditions.[1]

The results of the quantitative comparison of the two distributions, presented in Fig. 3, with the experimental[1] data are given in Table I, which gives the number of triggered detector stations (the number of degrees of freedom is less by 3, since three parameters

TABLE I.

	with field			without field		
n	χ^2	X, m	Y, m	χ^2	X, m	Y, m
42	48.9	1143	-452	86.5	1147	-417
39	33.6	1112	-452	73.1	1147	-417
24	26.1	1012	-417	22.9	1147	-417
24	41.7	1055	-406			
(experiment of Ref. 1)						

were determined), the values of the minimum of χ^2, and the coordinates X and Y of the shower axis in the array plane. One can see from this table that when the indications of all triggered detectors are considered ($n=42$) χ_1^2 for one degree of freedom equals 2.22, if the magnetic field is neglected. The probability of such a model agreeing with experiment is less than 10^{-4}. In the case when the field is taken into account $\chi_1^2=1.25$, which is entirely acceptable. Our analysis revealed that the indications of the three detectors contradict the data from neighboring stations. If these detectors are excluded from the analysis, then $\chi_1^2=2.03$ in the model without a field. The probability of agreement equals $\sim 0.03\%$. For a model that takes account of the field we have $\chi_1^2=0.93$ — excellent confirmation of the separation of muons according to the sign of their charge by the geomagnetic field. We note that the very first interpretation was made on the basis of a symmetric distribution of muons in a plane perpendicular to the shower axis. According to this criterion, 24 detector stations were selected (i.e., the indications of 18 stations were discarded!) and the value $\chi_1^2=2$ was obtained in a model without the field. The likelihood of this value is no more than 0.5%. The interpretation of the indications of these stations on the basis of our calculations did not favor any particular model ($\chi_1^2 = 1.1$ neglecting the field and $\chi_1^2=1.24$ taking the field into account). This is natural, since stations whose indications would be symmetric in a plane perpendicular to the shower axis were specially selected.

In summary, as a result of interpreting in terms of the quark–gluon string model the indications of all triggered detector stations, the separation of positively and negatively charged muons by the geomagnetic field in the largest shower detected at the Yakutsk array was observed at a very high level of significance 0.03%.

In closing, we thank G. T. Zatsepin for a fruitful discussion of the results, for suggestions, and for support.

[1] N. N. Efimov, T. A. Egorov, A. V. Glushkov *et al.*, in *Proceedings of the International Workshop on Astrophysical Aspects of the Most Energetic Cosmic Rays*, Kofu 20, 1990.

[2] N. Hayashida, K. Honda, M. Honda *et al.*, ICRR Report 324-94-19, Tokyo, 1994.

[3] D. J. Bird, S. C. Corbato, H. U. Dai *et al.*, Astrophys. J. **424**, 491 (1994).

[4] K. Greisen, Phys. Rev. Lett. **2**, 748 (1966).

[5] G. T. Zatsepin and V. A. Kuz'min, JETP Lett. **4**, 78 (1966).

[6] C. T. Hill, D. N. Schramm, T. P. Walker *et al.*, Phys. Rev. D **36**, 1007 (1987).

[7] N. N. Kalmykov, G. B. Khristiansen, J. Phys. G **21**, 1279 (1995).

[8] A. V. Kaĭdalov, K. A. Ter-Martirosyan, and Yu. M. Shabel'skiĭ, Yad. Fiz. **43**, 1282 (1986) [Sov. J. Nucl. Phys. **43**, 822 (1986)].

[9] A. M. Anokhina, V. I. Galkin, L. G. Dedenko *et al.*, Yad. Fiz. **60**, 290 (1997) [Phys. At. Nucl. **60**, 230 (1997)].

[10] B. N. Afanasiev, M. N. Dyakonov, V. P. Egorova *et al.* in *Proceedings of the 25th International Conference on Cosm. Rays,* Durban **6**, 1997, p. 229.

[11] A. M. Anokhina, V. I. Galkin, L. G. Dedenko *et al.*, Yad. Fiz. **61**, 1 (1998) [*sic*].

[12] Yu. P. Pyt'ev, Mat. Model. **4**, 76 (1992).

[13] Yu. P. Pyt'ev, Mat. Model. **3**, 65 (1991).

[14] Yu. N. Anotonov, Yu. N. Vavilov, G. T. Zatspin *et al.*, Zh. Éksp. Teor. Fiz. **32**, 227 (1957) [Sov. Phys. JETP **5**, 172 (1957)].

[15] L. G. Dedenko, Can. J. Phys. **46**, 178 (1968).

Translated by M. E. Alferieff

Scaling properties of transverse flow in Bjorken's scenario for heavy ion collisions

P. Milyutin and V. E. Fortov

High Energy Density Research Center of the Russian Academy of Sciences, 127412 Moscow, Russia

N. Nikolaev

Institut für Kernphysik, Forschungszentrum Jülich, D-52425 Jülich, Germany; L. D. Landau Institute of Theoretical Physics, Russian Academy of Sciences, 117940 Moscow, Russia

We report a simple analytical solution for the velocity u of the transverse flow of quark–gluon plasma at a hadronization front in Bjorken's scenario. We establish scaling properties of the transverse flow as a function of the expansion time. We present simple scaling formula for the expansion velocity distribution. © *1998 American Institute of Physics.* [S0021-3640(98)00515-5]

PACS numbers: 12.38.Mh, 25.75.−q

Landau's hydrodynamic stage[1] is a part of all scenarios for the evolution of the hot and dense matter (quark–gluon plasma — QGP) formed in ultrarelativistic heavy ion collisions.[2] It is now well understood that Landau's complete stopping of Lorentz-contracted colliding nuclei is not feasible because of the Landau–Pomeranchuck–Migdal (LPM) effect, i.e., the finite proper formation time τ_0 (Ref. 3; for the modern quantum chromodynamics (QCD) approach to the LPM effect see Ref. 4; the early works on LPM phenomenology of nuclear collisions are reviewed in Ref. 5), although evaluations of τ_0 and of the initial energy density $\epsilon_{\max}$ remain controversial.[2] A corollary of the LPM effect in conjunction with the approximate central rapidity plateau is the rapidity-boost invariance of initial conditions. The corresponding solution for a longitudinal expansion in an $1+1$-dimensional approximation, neglecting the transverse flow, was found by Bjorken (Ref. 6; see also Ref. 7). There is some experimental evidence,[8,9] although disputed,[10,11] for a transverse flow which must develop if the lifetime of the hydrodynamic stage is sufficiently long.

In this communication we present a simple solution of the Euler–Landau equation for the velocity of transverse expansion, u, gained in the hydrodynamic expansion of QGP before the hadronization phase transition. Our solution shows that for the usually considered lifetime τ_B of QGP the transverse flow is nonrelativistic. It is only marginally sensitive to properties of the hot stage and offers a reliable determination of τ_B if the radial profile of the initial energy density is known. We find that the u distribution is a scaling function of u/u_m, where u_m is a maximal velocity of expansion. We also com-

191

ment on the impact of the LPM effect on the buildup of the initial energy/matter density.

We start with the familiar Landau relativistic hydrodynamics equations

$$\partial_\mu T_{\mu\nu} = 0 ,\tag{1}$$

for the energy–momentum tensor $T_{\mu\nu} = (\epsilon + p)u_\mu u_\nu - p\delta_{\mu\nu}$, where ϵ and p are the energy density and pressure in the comoving frame, and u_μ is the 4-velocity of the element of fluid.[1,12] The initial state is formed from subcollisions of constituents (nucleons, constituent quarks and/or partons) of colliding nuclei and is glue dominated at early stages. The LPM effect implies that for a subcollision at the origin, $x = (t, z, \mathbf{r}) = 0$, the secondary particle formation vertices lie on a hyperbola of constant proper time τ, $\tau^2 = t^2 - z^2 \sim \tau_0^2$, and ϵ, p do not depend on the space–time rapidity $\eta = \frac{1}{2}\ln(t+z/t-z)$ of the comoving reference frame.[6,7] In the $1+1$-dimensional approximation, this leads to the celebrated Bjorken equation

$$\frac{\partial\epsilon}{\partial\tau} + \frac{\epsilon+p}{\tau} = 0 .\tag{2}$$

According to the lattice QCD studies, the familiar expression[12] $c_s^2 = \frac{1}{3}$ holds for the sound velocity c_s in the QGP except in a negligible narrow region of the hadronization transition temperature $T_h \sim 160\,\mathrm{MeV}$ and energy density $\epsilon_h \sim 1.5\,\mathrm{GeV/fm}^3$ (Refs. 13,14). With the equation of state $p = c_s^2\epsilon$, the Bjorken equation has a solution

$$\epsilon \propto \tau^{-(1+c_s^2)}.\tag{3}$$

Widely varying estimates for $\epsilon_{\max}$ and the proper time τ_0 are found in the literature.[2,14–16] However, as Bjorken has argued,[6] $\epsilon_{\max} \propto 1/\tau_0$, and the actual dependence of the Bjorken lifetime τ_B on $\epsilon_{\max}$ is rather weak:

$$\tau_B = \tau_0\left[\left(\frac{T_{\max}}{T_h}\right)^{4/(1+c_s^2)} - 1\right] = \frac{\tau_0\epsilon_{\max}}{\epsilon_h}\left[\left(\frac{\epsilon_{\max}}{\epsilon_h}\right)^{c_s^2/(1+c_s^2)} - \frac{\epsilon_h}{\epsilon_{\max}}\right].\tag{4}$$

For central Pb+Pb collisions, for which there is some experimental evidence for the QGP formation,[2] the typical estimates are $\tau_B \approx 3$ f/c at SPS[14,17] and $\tau_B \approx 6$ f/c at RHIC,[2] which are much larger than the standard estimate $\tau_0 \sim 0.5$ f/c.

Let us first comment briefly on two sources of substantial dilution of the initial energy density: the LPM effect and the finite Lorentz-contracted thickness of colliding nuclei. Because of the LPM effect, the density of produced matter vanishes at $\tau = 0$ and builds up on the time scale $\tau \sim \tau_0$. The buildup of energy density $E(\tau)$ from a superposition of elementary subcollisions in an absence of expansion can be modeled by the inclusion of a source term $f(\tau) = dE(\tau)/d\tau$ on the right-hand side. of the Bjorken equation (2), which then has the solution

$$\epsilon(\tau) = \tau^{-(1+c_s^2)}\int_0^\tau dt\, t^{(1+c_s^2)}\frac{dE}{dt} .\tag{5}$$

For the plausible parametrization $E(\tau) = E_0[1 - \exp(-\tau/\tau_0)]$ such an interplay of the formation and expansion of the hadronic matter dilutes the energy density substantially at

short times $\tau \sim \tau_0$. Furthermore, at finite energies the Lorentz-contracted thickness d $= 4R_A(m_p/W)$ of the colliding nuclei cannot be neglected and leads to a further dilution of the attainable energy density:

$$\langle \epsilon(\tau) \rangle = \int_0^d dt\, w(t)\, \epsilon(\tau - t) , \tag{6}$$

where the temporal distribution of subcollision vertices for central collisions can be estimated as $w(t) \approx (1/d)(1 - |2t - d|/d)\,\theta(d - t)\,\theta(t)$. The result of temporal smearing (6) only depends on $\gamma = d/\tau_0$. For instance, in central lead-on-lead fixed target collision at SPS energy $E/A = 160\,\text{GeV}$ we have $d \approx 1.3\,\text{fm}$, which is not small compared to the standard estimate $\tau_0 = 0.5\,\text{fm}$. The both dilution (5) and smearing (6) are short-time effects and have only a marginal impact on the dynamics of expansion at τ $\gtrsim \max\{\tau_0, d\}$ and are negligible at RHIC energies. Their impact at energy densities close to the threshold for QGP formation can be substantial, though, which may be the case for the SPS.

Now we turn to the major theme of collective transverse expansion, which is driven by radial gradient of pressure. As we shall see, the radial flow is nonrelativistic. Then, to the first order in radial velocity u_r, the radial projection of (1) gives the Euler–Landau equation

$$(\epsilon + p)\frac{\partial u_r}{\partial \tau} + u_r\left(\frac{\partial(\epsilon + p)}{\partial \tau} + \frac{(\epsilon + p)}{\tau}\right) + \frac{\partial p}{\partial r} = 0 , \tag{7}$$

in which we can use the Bjorken solution for ϵ and $p = c_s^2 \epsilon$. Then the Euler–Landau equation can be cast in the simple form

$$\frac{\partial u_r}{\partial \tau} - \frac{c_s^2}{\tau} u_r = -\frac{c_s^2}{(1 + c_s^2)}\frac{\partial \log p}{\partial r} . \tag{8}$$

The important point is that the transverse expansion of the QGP fireball can be neglected, an assumption which we can justify *a posteriori*. For this reason the time dependence of the logarithmic derivative $D(r, \tau) = \partial \log p/\partial r$ can be neglected: it is completely determined by the initial density profile and depends neither on the temperature nor fugacities of quarks and gluons, which substantially reduces the model-dependence of the transverse velocity. Then the solution of (7) subject to the boundary condition $u_r(\tau_0) = 0$ is

$$u_r(r, \tau) = \frac{c_s^2 \tau^{c_s^2}}{1 - c_s^4}\int_{\tau_0}^\tau dt\, t^{-c_s^2} D(r, t) \approx \frac{c_s^2 \tau D(r, 0)}{1 - c_s^4}\left[1 - \left(\frac{\tau_0}{\tau}\right)^{1 - c_s^2}\right] . \tag{9}$$

Model-independent estimates for the initial density/pressure profile are as yet lacking. At RHIC and higher energies of the initial state it is expected to be formed by semihard parton–parton interactions for which nuclear shadowing effects can be neglected.[2,15] Then for central collisions $\epsilon(r, \tau_0) \propto T_A^k(r)$, where $k = 2$ and $T_A(r)$ $= \int dz\, n_A(\sqrt{z^2 + r^2})$ is the density of constituents, $T_A(r) \sim \exp(-r^2/R_A^2)$, where R_A $\approx 1.1 A^{-1/3}\,\text{fm}$ is the nuclear radius. In another extreme scenario of strong shadowing and of strong LPM effect the soft particle production is not proportional to the multiplicity of collisions of fast partons[4,5] and $k = 1$ is more appropriate. Hereafter we take $k = 2$. In any case, the logarithmic pressure gradient is approximately linear, $D(r, t) \approx 2kr/R_A^2$, and

according to the solution (9) the displacement of the fluid element Δr is proportional to the radius, $\Delta r \propto r \tau^2$. Consequently, we have the Hubble-type radial rescaling

$$\lambda(\tau) \approx 1 + \frac{\Delta r}{r} \approx 1 + \left(\frac{\tau}{\tau_T}\right)^2 , \tag{10}$$

where

$$\tau_T \approx R_A / \sqrt{k} c_s \tag{11}$$

has the meaning of the lifetime against transverse expansion. For central Pb+Pb collisions Eq. (11) gives $\tau_T \approx 10 k^{-0.5}$ f/c, which is larger than the above-cited estimates of τ_B, and at SPS and RHIC energies the transverse expansion of the fireball can be neglected.

In a quasi-uniform plasma the hydrodynamic expansion lasts until $\epsilon = \epsilon_h$. For long-lived QGP and $\tau \gg \tau_0$ we can use the Bjorken solution

$$\epsilon(r, \tau) = \epsilon_h \left(\frac{T_A(r)}{T_A(0)}\right)^k \left(\frac{\tau_B}{\tau}\right)^{1+c_s^2} , \tag{12}$$

which gives the position of the hadronization front

$$r_h(\tau) = R_A \sqrt{\frac{1 + c_s^2}{k} \ln \frac{\tau_B}{\tau}} \tag{13}$$

and the radial velocity at the hadronization front

$$u(\tau) = u_r(r_h(\tau), \tau) = \frac{c_s^2 \tau}{R_A(1 - c_s^4)} \sqrt{4k(1 + c_s^2)\ln \frac{\tau_B}{\tau}} \left[1 - \left(\frac{\tau_0}{\tau}\right)^{1 - c_s^2}\right] . \tag{14}$$

For the values of τ_B and τ_0 usually discussed we have $\tau_B \gg \tau_0$. For such a long-lived QGP, $\tau_B \gg \tau_0$, the radial velocity takes the maximal value u_m at $t \approx 1/\sqrt{e}$,

$$u_m = \frac{c_s^2 \tau_B}{R_A(1 - c_s^4)} \sqrt{\frac{2k(1 + c_s^2)}{e}} \left[1 - \left(\frac{\tau_0 \sqrt{e}}{\tau_B}\right)^{1 - c_s^2}\right] . \tag{15}$$

It is remarkable that the average radial acceleration u_m / τ_B is approximately constant. The solid line in Fig. 1 shows the maximal velocity u_m evaluated from (14). The large-τ_B approximation (15), shown by the dashed line, reproduces these results to better than $\sim 4\%$ at $\tau_B = 3$ f/c and better than $\sim 1\%$ at $\tau_B = 8$ f/c. For the above-cited estimates for τ_B in central Pb+Pb collisions we find $u_m(\text{SPS}) \approx 0.13$ and $u_m(\text{RHIC}) \approx 0.28$; consequently, the nonrelativistic expansion approximation is justified very well. Now notice that for a long-lived QGP the hadronization front (13), shown in Fig. 2, and $u(\tau)/u_m$ depend only on the scaling variable $t = \tau/\tau_B$, with the obvious exception of the short-time region $\tau \sim \tau_0$. This scaling property is clearly seen in Fig. 3, where we show u/u_m as a function of $t = \tau/\tau_B$. Notice the convergence to a universal curve with increasing τ_B.

The most interesting quantity is the radial velocity distribution, which can be evaluated experimentally from the Doppler modifications of the thermal spectrum. In order to test our results one needs particles which are radiated from the hadronization front. The
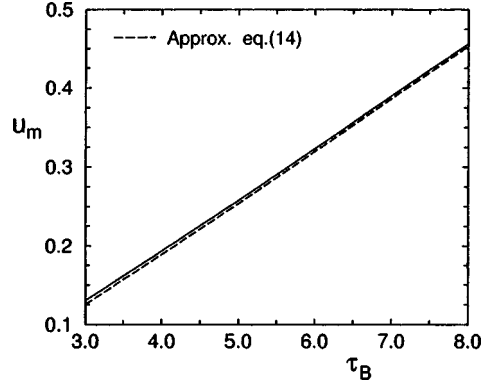
FIG. 1. The maximal velocity of radial expansion u_m for for central Pb+Pb collisions as a function of the expansion time τ_B. Shown by the dotted line is the large-τ_B formula (17).

standard scenario is that the hadronization transition is followed by an expanding mixed phase which, however, does not contribute to the transverse velocity because in the mixed phase $c_s^2 = 0$. The mixed phase is followed by a hydrodynamic expansion and post-acceleration of strongly interacting pions and baryons until the hadronic freeze-out temperature $T_f < T_h$ is reached.[18] Because this post-acceleration is negligible for weakly interacting K^+ and ϕ mesons, one obtains the desired access to the radial flow at the hadronization transition. In evaluating the modification of the thermal spectrum one needs to know the u distribution weighted with the particle multiplicity. For a constant hadronization temperature the contribution of the hadronization surface $r_h(\tau)$ to the particle multiplicity is

$$dw \propto r_h(\tau)d\tau. \tag{16}$$

With the use of the solutions (13) and (14), it can readily be transformed into $dw/du \propto r_h(du/d\tau)^{-1}$. The important point is that because of the above-discussed scaling properties of the transverse flow, the velocity distribution is a scaling function of $x = u/u_m$:
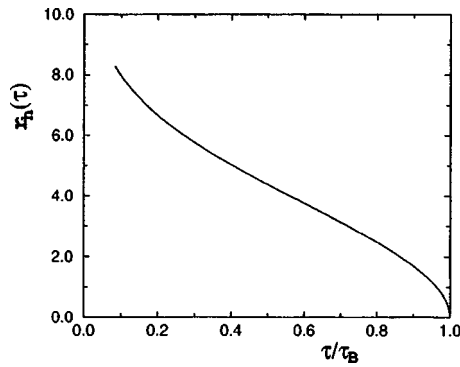
FIG. 2. The time dependence of the hadronization front for central Pb+Pb collisions.
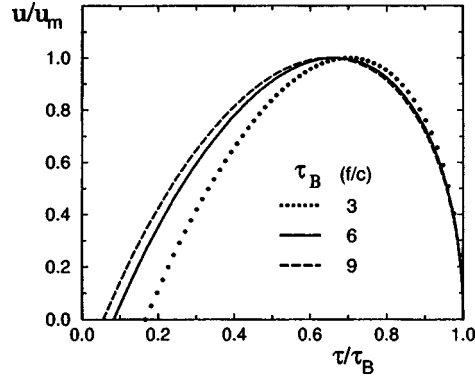
FIG. 3. The convergence to the scaling behavior of the time dependence of the relative radial velocity u/u_m for central Pb+Pb collisions.

$$\frac{dw}{du} = \frac{1}{u_m} \frac{f(x, \tau_B)}{\sqrt{1-x}}, \tag{17}$$

where for a long-lived QGP $f(x, \tau_B)$ does not depend on τ_B. The square-root singularity at $x=1$ is a trivial consequence of the vanishing derivative $du(\tau)/d\tau$ at $\tau \approx \tau_B/\sqrt{e}$. In Fig. 4 we show the scaling function $f(x, \tau_B)$ for $\tau_B = 6$ f/c. We don't show $f(x, \tau_B)$ for other values of τ_B, because the variations from $\tau_B = 6$ f/c to 3 f/c and 9 f/c do not exceed several percent and are confined to a narrow region $x \lesssim 0.2$. The approximation $f(x) = 0.5$ is good for all practical purposes.

In conclusion, we would like to argue that the shape of the velocity distribution is to a large extent model-independent. The generic origin of the square-root singularity at $x = 1$ has already been emphasized, the fact that $f(0) \neq 0$ is due to a radiation from the surface $r_h \sim R_A$ in the early stages of expansion. Above we assumed that hydrodynamic expansion continues until the hadronization transition. Following Pomeranchuk[19] one can argue that in the nonuniform plasma the hydrodynamic expansion stops when the mean free path
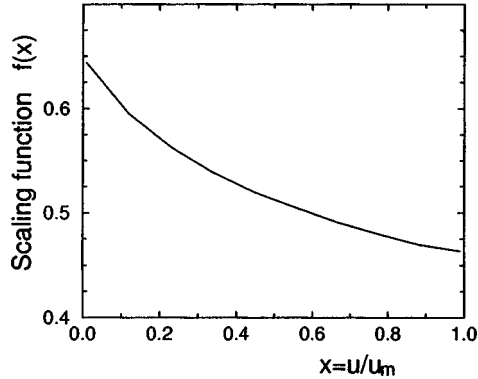

FIG. 4. The scaling function $f(x, \tau_B)$ of Eq. (17), shown for $\tau_B = 6$.

$$l_{\text{int}} = 1/n(r_c, \tau)\sigma_t \tag{18}$$

defined in terms of the transport cross section σ_t, is larger that the GQP density variation length $D(r,0)^{-1}$. In the partially equilibrated QGP $l_{\text{int}} \propto T^{-1}$. Then for the temperature T_P at which the hydrodynamic expansion stops, the Pomeranchuk condition gives $T_P \propto r/R_A^2$. The possibility remains open that in the early stages $T_P > T_h$, in which case $dw \propto r_h(\tau)(T_P/T_h)^3 d\tau$. This enhanced radiation at early stages at slow radial expansion but at higher temperatures T_P would mimic radiation at a lower temperature and higher radial velocity. This may result in the apparent depletion of $f(0)$; in order to explore this possibility one needs a better understanding of l_{int} near the hadronization transition.

The NA49 fits to the proton, kaon, and pion transverse mass m_T distributions in central Pb+Pb collisions at SPS assume an identical freeze-out temperature for all particle species.[8] For positive particles NA49 finds $T_f = 140 \pm 7$ MeV and the transverse velocity $\langle u \rangle = 0.41 \pm 0.11$. However, for the K^+ one must take the higher freeze-out temperature $T_f = T_h \approx 160$ MeV given by the lattice QCD. Because of the anti-correlation between the local temperature T_f and $\langle u_T \rangle$ (see Fig. 7 in Ref. 9), such a fit with larger T_f to the same m_T distribution would yield a smaller $\langle u \rangle$.

[1] L. D. Landau, Izv. Akad. Nauk SSSR, Ser. Fiz. **17**, 51 (1953).

[2] K. Geiger, Phys. Rep. C **258**, 237 (1995); J. W. Harris and B. Müller, Annu. Rev. Nucl. Part. Sci. **46**, 71 (1996); B. Müller, Nucl. Phys. A **630**, 461c (1998).

[3] L. D. Landau and I. Ya. Pomeranchuk, Dokl. Akad. Nauk **92**, 525, 735 (1953).

[4] B. G. Zakharov, JETP Lett. **63**, 952 (1996); **64**, 781 (1996); **65**, 615 (1997); Yad. Fiz. **61**, 924 (1998) [Phys. At. Nucl. **61**, 838 (1998)].

[5] N. N. Nikolaev, Usp. Fiz. Nauk **134**, 369 (1981) [Sov. Phys. Usp. **24**, 531 (1981)].

[6] J. D. Bjorken, Phys. Rev. D **27**, 140 (1983).

[7] E. V. Shuryak, Yad. Fiz. **28**, 706 (1978) [Sov. J. Nucl. Phys. **28**, 408 (1978)].

[8] I. G. Bearden, H. Bøggild, J. Boissevain *et al.*, Phys. Rev. Lett. **78**, 2080 (1997).

[9] H. Appelshäuser, J. Bachler, S. J. Bailey *et al.*, Eur. Phys. J. C **2**, 661 (1998).

[10] P. Braun-Munzinger and J. Stachel, http://xxx.lanl.gov/abs/nucl-ex/9803015.

[11] Jan-e Alam, J. Cleymans, K. Redlich, and H. Satz, http://xxx.lanl.gov/abs/nucl-th/9707042.

[12] L. D. Landau and E. M. Lifshitz, *Fluid Mechanics*, Course of Theoretical Physics, Vol. VI, Ch. 15, Pergamon Press, Oxford, 1960.

[13] C. M. Hung and E. V. Shuryak, Phys. Rev. Lett. **75**, 4003 (1995).

[14] B. R. Schlei, Heavy Ion Phys. **5**, 403 (1997).

[15] K. J. Eskola, B. Müller, and X. N. Wang, Phys. Lett. B **374**, 20 (1996); K. J. Eskola, K. Kajantie and P. V. Ruuskanen, Eur. J. Phys. C **1**, 627 (1998).

[16] U. Mayer and U. Heinz, Phys. Rev. C **56**, 439 (1997); J. Sollfrank *et al.*, Phys. Rev. C **55**, 392 (1997).

[17] A. Dumitru, J. Brachmann, M. Bleicher *et al.*, Workshop on Hydrodynamics at ECT*, Trento, May 1997, http://xxx.lanl.gov/abs/nucl-th/9705056.

[18] H. Bebie, P. Gerber, J. L. Goity, and H. Leutwyler, Nucl. Phys. B **378**, 95 (1992).

[19] I. Ya. Pomeranchuk, Dokl. AN SSSR **78**, 889 (1951).

New computational method for atoms in an intense electromagnetic field

L. P. Rapoport

Voronezh State University,[a) 394693 Voronezh, Russia

A new representation is found for the interaction of intense circularly polarized light with an atom. A stationary centrosymmetric part, which depends on the field parameter $a_0 = F/\omega^2$, is separated out from the atom–field interaction. The time-dependent part of the interaction is represented in the form of a multipole expansion with a_0 taken into account. The application of this representation for calculating the nonlinear dynamic polarizability of a complicated atom in the random-phase approximation with exchange is studied. © *1998 American Institute of Physics.* [S0021-3640(98)00615-X]

PACS numbers: 32.80.−t, 02.70.−c

In recent years a great deal of attention has been devoted to problems concerning the dynamics of atomic electrons in ultrahigh laser fields.[1] Two problems are encountered in the study of the properties of a complicated atom interacting with an intense electromagnetic field. First, it is impossible to use the standard nonstationary perturbation theory because there is no small perturbation parameter.[2] Second, the single-particle approximation for an electron in the atom — the Hartree–Fock (HF) approximation — is inadequate. Nor, however, can the random-phase approximation with exchange (RPAE) be used in its standard form to take into account the multiparticle interactions in the atom, since this approximation is applicable only for a weak external field.[3] An intense electromagnetic field acts not only directly on a definite electron but also on all the other electrons in the atom, giving rise to virtual excitations that depend on the frequency and strength of the field. There arises a nonlinear dynamic polarizability of the atomic shells that cannot be calculated in the standard RPAE method, since it must be taken into account both in the HF basis functions of the atom + field system and in the expression for the strong, transition-initiating field.

In the present letter a new expression that is suitable even for ultrahigh electromagnetic fields is obtained for the interaction of an atom with a circularly polarized field. It is shown how the HF equations for a ''field-dressed'' atom and the RPAE equations are modified in a strong field.

HAMILTONIAN OF A HYDROGENLIKE ATOM IN AN INTENSE ELECTROMAGNETIC FIELD

Let the solution of the Schrödinger equation (the atomic system of units $\hbar = e = m = 1$ is used)

198

$$i \frac{\partial \Psi}{\partial t} = \hat{H}(t)\Psi \tag{1}$$

be represented in the form $\Psi' = \hat{U}\Psi$, where $\hat{U}^{\dagger} = \hat{U}^{-1}$ is a unitary operator. Then we obtain for Ψ' an equation of the form (1) with the operator

$$\hat{H}' = i \left(\frac{\partial \hat{U}}{\partial t} \right) \hat{U}^{\dagger} + \hat{U}\hat{H}\hat{U}^{\dagger}. \tag{2}$$

Let us consider first a hydrogenlike atom with nuclear charge Z in a field described by the vector potential $\mathbf{A}(t)$ (dipole approximation):

$$\hat{H} = \frac{1}{2} \left(\hat{\mathbf{p}} + \frac{1}{c}\mathbf{A}(t) \right)^2 - \frac{Z}{r}. \tag{3}$$

In a circularly polarized field

$$\mathbf{A}(t) = -A_0(\mathbf{e}_x \sin \omega t + \eta \mathbf{e}_y \cos \omega t), \tag{4}$$

where $A_0 = Fc/\omega$, c is the velocity of light, $\eta = \pm 1$ for left- (right-) hand polarized waves, F is the intensity of the field, and ω is the frequency of the field.

Using Eq. (2), let us transform the Hamiltonian (3) by means of two successive unitary operators

$$\hat{U}_{K-H} = \exp\left[\frac{i}{c} \hat{\mathbf{p}} \int^t \mathbf{A}(t')dt' \right]. \tag{5}$$

We obtain

$$\hat{H}_{\mathrm{vib}} = \hat{U}_{K-H} \hat{H} \hat{U}_{K-H}^{\dagger} \tag{6}$$

(Kramers–Henneberger transformation[4]) and

$$\hat{U}_{\mathrm{rot}} = \exp(-i\eta\omega t \hat{L}_z), \tag{7}$$

where $\hat{L}_z = -i\partial/(\partial\varphi)$ is the angular momentum projection operator in a spherical coordinate system. The operator $\hat{U}_{\mathrm{rot}}$ effects a transformation into a rotating coordinate system

$$\hat{H}_{\mathrm{rot}} = \hat{U}_{\mathrm{rot}} \hat{H}_{\mathrm{vib}} \hat{U}_{\mathrm{rot}}^{\dagger}. \tag{8}$$

As a result of two transformations we have[5]

$$\hat{H}_{\mathrm{rot}}(\mathbf{r}, \mathbf{a}_0) = -\frac{1}{2}\nabla^2 - \frac{Z}{|\mathbf{r} - \mathbf{a}_0|} + \eta\omega L_z, \tag{9}$$

where $\mathbf{a}_0 = a_0 \mathbf{e}_x$ and $a_0 = F/\omega^2$. The operator (9) does not depend on the time, and Eq. (1) with the operator $\hat{H}_{\mathrm{rot}}$ (9) becomes a stationary Schrödinger equation with exact quasienergy E. It is important to note that $\hat{H}_{\mathrm{rot}}$ (9) has the same asymptotic behavior in the limit $r \to \infty$ as the Hamiltonian (3) without a field. The field parameter a_0 determines the dynamics of an electron and the quasienergy spectrum E in the atom + field system.

In Eq. (9) the potential $Z|\mathbf{r}-\mathbf{a}_0|^{-1}$ is a generating function for the Legendre polynomials. It can be represented in the form of the series expansion in terms of the spherical harmonics $Y_{lm}(\theta,\varphi)$ and $Y_{lm}(\mathbf{a}_0/a_0)$

$$Z|\mathbf{r}-\mathbf{a}_0|^{-1}=\sum_{l=0}^{\infty}\sum_{m=-l}^{l}\frac{4\pi Z}{2l+1}\xi_l(r,a_0)\,Y_{lm}(\theta,\varphi)\,Y_{lm}^*(\mathbf{a}_0/a_0),\qquad(10)$$

where $\xi_l(r,a_0)=r_<^l/r_>^{l+1}$, $r_<=\min(r,a_0)$, and $r_>=\max(r,a_0)$.

We now use the inverse unitary transformation $\hat{U}_{\text{rot}}^{-1}=\hat{U}_{\text{rot}}^{\dagger}$ (2) to return into the vibrating coordinate system. We obtain

$$\hat{H}_{\text{vib}}(\mathbf{r},\mathbf{a}_0;t)=-\frac{1}{2}\nabla^2-\sum_{l=0}^{\infty}\frac{4\pi Z}{2l+1}\xi_l(r,a_0)Y_{l0}(\theta,\varphi)\,Y_{l0}^*(\mathbf{a}_0/a_0)$$

$$-\sum_{l=1}^{\infty}\sum_{\substack{m=-l\\(m\neq0)}}^{l}\frac{4\pi Z}{2l+1}\xi_l(r,a0)\,Y_{lm}(\theta,\varphi)\,Y_{lm}^*(\mathbf{a}_0/a_0)\,e^{-i\eta m\omega t}.\qquad(11)$$

The second term in Eq. (11) does not depend on the time, but for $l>0$ it is noncentral. We extract from it the centrosymmetric part, multiply by $|Y_{l'0}|^2$, and integrate over the solid angle $d\Omega$. We obtain

$$\hat{V}_s^l(r,a_0)=Z\sqrt{4\pi}\,(2l+1)\sum_{k=0}^{2l}\xi_k(r,a_0)\,Y_{l0}^*(\mathbf{a}_0/a_0)(2k+1)^{-1}\begin{pmatrix}l&k&l\\0&0&0\end{pmatrix}^2.\qquad(12)$$

The difference between the time-independent potential term (11) and $\hat{V}_s^l$ is not centrosymmetric, and in the case of super-intense fields it can be taken into account by the coupled-channels method (or by stationary perturbation theory). In what follows we shall neglect it. Then $\hat{H}_{\text{vib}}(\mathbf{r},\mathbf{a}_0;t)$ can be represented in the form

$$\hat{H}_{\text{vib}}(\mathbf{r},\mathbf{a}_0;t)=-\frac{1}{2}\nabla^2-\hat{V}_s^l(r,a_0)-\hat{V}_{\text{int}}(\mathbf{r},\mathbf{a}_0;t),\qquad(13)$$

where

$$\hat{V}_{\text{int}}(\mathbf{r},\mathbf{a}_0;t)=\sum_{l=1}^{\infty}\sum_{\substack{m=-l\\(m\neq0)}}^{l}\frac{4\pi Z}{2l+1}\xi_l(r,a0)\,Y_{lm}(\theta,\varphi)\,Y_{lm}^*(\mathbf{a}_0/a_0)\,e^{-i\eta m\omega t}.\qquad(14)$$

Let us compare $\hat{V}_s^l+\hat{V}_{\text{int}}$, given by Eqs. (12) and (14), with the Fourier series expansion of $|\mathbf{r}-\mathbf{a}(t)|^{-1}$, ordinarily used in calculations with super-intense electromagnetic fields[4] in the quasienergy method.[6] In this case

$$|\mathbf{r}-\mathbf{a}(t)|^{-1}=\frac{1}{\pi}\sum_{n=-\infty}^{\infty}i^{-n}e^{in\omega t}\int_0^{\pi}\frac{\cos(n\alpha)\,d\alpha}{|\mathbf{r}-\mathbf{a}_0\cos\alpha|},\qquad(15)$$

where $\mathbf{a}_0$ can be used for both linear and circular polarization of light. The stationary part in the expansion (15) can be extracted by setting $n=0$:

$$\hat{V}^0=\frac{1}{\pi}\int_0^{\pi}\frac{d\alpha}{|\mathbf{r}-\mathbf{a}_0\cos\alpha|}.\qquad(16)$$

$\hat{V}_0$ is not centrosymmetric (it can be expressed in terms of a complete elliptic integral with arguments $\mathbf{r}, \mathbf{a}_0$), so that in Eq. (16) it is impossible to separate the radial and angular variables. Circularly polarized radiation has no advantages over linear polarization. The Fourier coefficients (15) for $n > 0$ also have a very complicated form. For this reason, expression (15) cannot be expanded in multipoles. The advantages of $\hat{V}_s^l + \hat{V}_{int}$, Eqs. (12) and (14), over the representation (15) for circularly polarized light are obvious.

HF EQUATIONS FOR THE ATOM+FIELD SYSTEM AND THE RPAE METHOD

The Coulomb interaction $|\mathbf{r}_k - \mathbf{r}_q|^{-1}$ between the electrons in a complicated atom does not change under unitary transformations by the operators (5) and (7). For this reason, the N-electron Hamiltonian $\hat{H}^{af}$ in the field (4) for a ''dressed'' atom has the form

$$\hat{H}_{vib}^{af} = \sum_{k=1}^{N} \left\{ -\frac{1}{2}\nabla_k^2 - V_{sk}^l(r,a_0) \right\} + \frac{1}{2}\sum_{k \neq q=1}^{N} \frac{1}{|\mathbf{r}_k - \mathbf{r}_q|}. \tag{17}$$

Since the potential $V_{sk}^l(r,a_0)$ (12) replacing the Coulomb interaction between the electrons and the nucleus is centrosymmetric, the system of HF equations for the Hamiltonian (17) can be derived by the standard variational procedure. Representing the trial function in the form $\Psi = \det\|\varphi_k(\mathbf{r},\mathbf{a}_0)\|$ we obtain

$$\left\{ -\frac{1}{2}\nabla^2 - \hat{V}_s^l \right\}\varphi_i(\mathbf{r},a_0) + \sum_{k=1}^{N} \int \frac{d\mathbf{r}'}{|\mathbf{r} - \mathbf{r}'|}\varphi_k^*(\mathbf{r}',a_0)$$

$$\times [\varphi_k(\mathbf{r}',a_0)\varphi_i(\mathbf{r},a_0) - \varphi_i(\mathbf{r}',a_0)\varphi_k(\mathbf{r},a_0)] = \varepsilon_i\varphi_i(\mathbf{r},a_0). \tag{18}$$

The angular parts in Eqs. (18) can be extracted and, integrating the equations for arbitrary field parameter $a_0 = F/\omega^2$ (except, of course, for the static limit $\omega \to 0$), $\varepsilon_i(a_0)$ and $\varphi_i(\mathbf{r},a_0)$ can be found for a ''field-dressed'' atom.

The RPAE equations can be easily found similarly to the HF method. Actually, the entire RPAE theory derived for a weak initiating external electromagnetic field in a stationary coordinate system can be applied in the case of a strong field in a coordinate system oscillating with the frequency of the field. For this, the dipole vertex, which is independent of the field F,

$$V(\mathbf{r}) = \pm\left(\frac{8\pi}{3}\right)^{1/2} r\, Y_{1,\mp 1}(\mathbf{n})$$

must be replaced by the (l,m)th component of the vertex (14) in a strong field

$$\hat{V}^{l,m}(\mathbf{r},a_0) = \frac{4\pi Z}{2l+1}\xi_l(r,a_0)\, Y_{lm}(\theta,\varphi)Y_{lm}^*(\mathbf{a}_0/a_0), \tag{19}$$

where $l, m > 0$. For multiphoton absorption ($l \gg 1$, $m \approx l$) an asymptotic representation can be used for the $Y_{lm}(\theta,\varphi)$ and $Y_{lm}^*(\mathbf{a}_0/a_0)$ appearing in Eq. (19):[7]

$$Y_{lm}(\theta,\varphi) \approx \frac{e^{im\varphi}}{\pi}\frac{\cos\left[(2l+1)\frac{\theta}{2} + (2m-1)\frac{\pi}{4}\right]}{\sqrt{\sin\theta}};$$

$$Y_{lm}^*(\mathbf{a}_0/a_0) = \begin{cases} (-1)^{(l+m)/2}\left[\dfrac{2l+1}{4\pi}\Phi(l,m)\right]^{1/2}, & l+m \quad \text{even}, \\ \\ 0, & l+m \quad \text{odd}. \end{cases}$$

Here

$$\Phi(l,m) = \frac{(l-m-1)!!}{(l-m)!!}\frac{(l+m-1)!!}{(l+m)!!}.$$

The zero-field HF wave functions must be replaced by the nonzero-field functions $\varphi_k(\mathbf{r},\mathbf{a}_0)$, and $\omega \to m\omega$. The well-known integral equation for the RPAE matrix elements[3] will become in the RPAE in a strong field:

$$\langle k_2|\hat{V}(m\omega,a_0)|k_1\rangle = \langle k_2|\hat{V}^{l,m}|k_1\rangle$$

$$+ \sum_{k_3,k_4} \frac{(n_{k_3}-n_{k_4})\langle k_1|\hat{V}(m\omega,a_0)|k_3\rangle\langle k_2 k_3|U|k_1 k_4\rangle}{\varepsilon_{k_3}(a_0)-\varepsilon_{k_4}(a_0)+m\omega+i\delta(1-2n_{k_4})}, \qquad (20)$$

where

$$n_\lambda = \begin{cases} 1, & \lambda \leqslant F, \\ 0, & \lambda > F, \end{cases}$$

F is the Fermi level and $U = |\mathbf{r}_k - \mathbf{r}_q|^{-1}$. In Eq. (20), the first term on the right-hand side describes the direct action of an external field on an electron, which is transferred from $|k_1\rangle$ into $|k_2\rangle$ in the "dressed" atom. The second term is a correlation term. It describes the excitation of another electron by an external field $\hat{V}^{l,m}$ with formation of an electron–hole pair, calculated using the HF functions of the "dressed" atom. The electron–electron interaction U in the last term in Eq. (20) leads to transfer of excitation from other atomic electrons (sum over k_3 and k_4) to the electron under study. Physically, the second term represents the polarization of an atom in a strong field a_0, $m\omega$, i.e., the nonlinear dynamic polarizability of the atom. To calculate it, the integral equation (20) must be solved for the effective vertex. The solution of this equation is simplified considerably by performing the integration over the angular variables analytically. As a result, Eq. (20) for $\hat{V}(m\omega;a_0)$ will become one-dimensional. The matrix elements will be expressed in terms of the reduced and $3j$- and $6j$-symbols.

In conclusion, we note that all known refinements of the RPAE method in a weak field can also be used for the RPAE in a strong field with the substitution indicated earlier.

a)e-mail: kornev@tooth.vsu.ru

[1] H. G. Muller and M. V. Fedorov (Eds.), *Super-Intense Laser-Atom Physics*, Vol. IV, Kluwer Academic, Dordrecht, 1996.
[2] N. L. Manakov, V. D. Ovsiannikov, and L. P. Rapoport, Phys. Rep. **141**, 320 (1986).
[3] M. Ya. Amus'ya, *The Photoeffect in Atoms* [in Russian], Nauka, Moscow, 1987.

[4] W. C. Henneberger, Phys. Rev. Lett. **21**, 838 (1968).

[5] L. P. Rapaport, Zh. Éksp. Teor. Fiz. **105**, 534 (1994) [JETP **78**, 284 (1994)].

[6] N. B. Delone and V. P. Krainov, *Multiphoton Processes in Atoms*, Springer-Verlag, Berlin, 1994.

[7] D. A. Varshalovich, A. N. Moskalev, and V. K. Khersonskiĭ, *The Quantum Theory of Angular Momentum* [in Russian], Nauka, Leningrad, 1975.

Translated by M. E. Alferieff

Parametrization and universal properties of turbulence of an incompressible fluid

S. N. Gordienko

L. D. Landau Institute of Theoretical Physics, Russian Academy of Sciences, 142432 Chernogolovka, Moscow Region, Russia

S. S. Moiseev

Institute of Space Research, Russian Academy of Sciences, 117810 Moscow, Russia

A relation is established between the properties of turbulent flow, the force f_0 setting the fluid in motion, and the spatial r_0 and temporal τ_0 turbulence scales. It is established that the Loĭtsyanskiĭ integral diverges for such turbulence. It is shown that the spectral properties of turbulence depend on the quantity $\gamma = f_0 \tau_0^2 / r_0$. The spectrum of turbulent pulsations consists of several universal segments, whose appearance and arrangement depend on γ. It is shown that the parameter $\Gamma = \gamma^{4/3} \mathrm{Re}$ determines the specific dissipation power. The cases of large and small parameters γ and Γ are studied in detail. The physical mechanism leading to "switching off" of dissipation in the limit $\Gamma \gg 1$ is determined. © *1998 American Institute of Physics.* [S0021-3640(98)00715-4]

PACS numbers: 47.27.Ak

The Kolmogorov spectrum and the associated ideas of universality, constant energy flux along the spectrum, and inertial range are the foundation of our current understanding of the nature of homogeneous turbulence of an incompressible fluid. At the same time, the Kolmogorov spectrum is not the only experimentally observed spectrum of turbulent pulsations in a turbulent incompressible fluid. For example, besides the 5/3 Kolmogorov spectrum, there is the well-known 7/3 spectrum associated with the flow of helicity.[1] Thus there arises the question of the conditions under which one or another spectrum is formed, i.e., the question of finding the parameters that determine the spectral composition of turbulent pulsations in one or another range of wave numbers. The present letter is devoted to the problem of determining the segments of the spectrum with universal behavior and the parameters responsible for the appearance of these segments.

1. Since we are interested only in fluid flows with large Reynolds numbers, as a first step we shall examine the Euler equation (Re $= +\infty$) with an external force $\mathbf{f}(\mathbf{r},t)$:

$$\frac{\partial \mathbf{v}}{\partial t} + (\mathbf{v} \cdot \nabla)\mathbf{v} = -\nabla p + \mathbf{f}(\mathbf{r},t), \quad \langle \mathbf{f}(\mathbf{r},t) \rangle = 0, \tag{1}$$

$$\langle \mathbf{f}(\mathbf{r}_1,t_1)\cdot\mathbf{f}(\mathbf{r}_2,t_2)\rangle = f_0^2 K\left(\frac{t_1-t_2}{\tau_0},\frac{\mathbf{r}_1-\mathbf{r}_2}{r_0}\right), \tag{2}$$

where K describes the correlation properties of the force $\mathbf{f}$ that sets the fluid in motion, and by definition of f_0^2

$$\int K\left(\frac{t}{\tau_0},\frac{\mathbf{r}}{r_0}\right) d\mathbf{r}\, dt = r_0^3 \tau_0.$$

For what follows, it is important that the last integral converges and is nonzero, i.e., the restrictions imposed on the force that sets the fluid in motion reduce to these. To avoid confusion, we emphasize that the equality $\langle \mathbf{f}(\mathbf{r},t)\rangle = 0$ does not imply that the above integral of the function K vanishes. Without loss of generality the force $\mathbf{f}$ can be assumed to be purely solenoidal, the potential part being included in the pressure gradient.

2. To study the spectral properties of the problem (1) and (2), we shall employ the kinetic equation obtained in Ref. 2 in the limit $\mathrm{Re}\to +\infty$ (see explanations below) for Lagrangian particles of an incompressible fluid:

$$\left(\frac{\partial}{\partial t}+\hat{L}_1+\hat{L}_2\right)F_2(t,1,2)=P(t,1,2)+P(t,2,1)+\hat{Q}(1,2)F_2, \tag{3}$$

where $F_2(t,1,2)=F_2(t,\mathbf{r}_1,\mathbf{v}_1,\mathbf{a}_1,\mathbf{r}_2,\mathbf{v}_2,\mathbf{a}_2)$ is the ''expanded'' (i.e., depending not only on the velocities but also the accelerations arising as a result of the interaction of the Lagrangian particles) two-particle distribution function,

$$\hat{L}_i=\mathbf{v}_i\cdot\frac{\partial}{\partial\mathbf{r}_i}+(\mathbf{a}_i+\mathbf{f}(\mathbf{r}_i,t))\cdot\frac{\partial}{\partial\mathbf{v}_i}, \quad i=1,2,$$

$$P(t,1,2)=\int_0^{+\infty}e^{-\tau\hat{L}_1}\left(\int\int \hat{Q}(1,3)\hat{Q}(2,4)F_2(t-\tau,1,3)F_2(t,2,4)\,d3\,d4\right)d\tau,$$

$$\hat{Q}(1,2)=2(a_{2,l}-a_{1,l})(v_{2,m}-v_{1,m})\frac{\partial^3}{\partial x_{1,l},\partial x_{1,m},\partial x_{1,p}}\frac{1}{|\mathbf{r}_1-\mathbf{r}_2|}\left(\frac{\partial}{\partial a_{1,p}}-\frac{\partial}{\partial a_{2,p}}\right)$$

$$-(v_{2,m}-v_{1,m})(v_{2,l}-v_{1,l})(v_{2,n}-v_{1,n})\frac{\partial^4}{\partial x_{1,l},\partial x_{1,m},\partial x_{1,n},\partial x_{1,p}}\frac{1}{|\mathbf{r}_1-\mathbf{r}_2|}$$

$$\times\left(\frac{\partial}{\partial a_{1,p}}-\frac{\partial}{\partial a_{2,p}}\right),$$

where in the last formula summation over repeated indices is assumed, and $v_{2,l}$, $a_{2,l}$ and $v_{1,l}$, $a_{1,l}$ are the lth components of the vectors $\mathbf{v}_2$, $\mathbf{a}_2$ and $\mathbf{v}_1$, $\mathbf{a}_1$, respectively.

Let us clarify the point of introducing distribution functions containing accelerations as additional arguments. Ordinarily, in constructing kinetic equations one endeavors to describe, on the basis of distribution functions, the processes associated with the inter-particle interaction. In Ref. 3 it was suggested that a kinetic equation be constructed by solving the inverse problem: Given the spatial distribution of the forces (in the case of a fluid — the pressure gradient), calculate multiparticle distribution functions which are consistent with the prescribed distribution of the ''force'' vectors. This leads to distribution functions that depend on the accelerations. Since no restrictions are imposed on the

initial spatial distributions of the ''forces,'' aside from the restrictions following from Newton's laws, such an approach makes it possible to describe fluctuations correctly on the basis of a kinetic equation.[4] What's more, any ''expanded'' distribution function also contains the information that is contained only in the entire infinite set of conventional distribution functions (for example, any ''expanded'' distribution function makes it possible to calculate $\langle \mathbf{a}^{2n} \rangle$ for arbitrary n). This explains why in a number of problems where it is impossible to truncate the standard BBGKY chain a closed equation can be obtained for the ''expanded'' two-particle distribution function.[2] We note that kinetic equations of this type have been used successfully to solve a number of problems of plasma physics.[5]

3. If the function $F_2(t,1,2)$ is the solution of Eq. (3), then the function

$$F_2^{(\Delta,\lambda)}(t,1,2) = \lambda^{18\Delta+12} F_2(\lambda^{1+\Delta}t, \lambda \mathbf{r}_1, \lambda^{\Delta}\mathbf{v}_1, \lambda^{2\Delta}\mathbf{a}_1, \lambda \mathbf{r}_2, \lambda^{\Delta}\mathbf{v}_2, \lambda^{2\Delta}\mathbf{a}_2) \tag{4}$$

is also the solution of Eq. (3) but with a different external force

$$\mathbf{f}^{(\Delta,\lambda)}(\mathbf{r},t) = \lambda^{2\Delta+1} \mathbf{f}(\lambda \mathbf{r}, \lambda^{1+\Delta}t), \tag{5}$$

where $\lambda > 0$ and Δ are arbitrary numbers.

To study the large-scale structure of the flow we choose the number Δ in a manner so that as $\lambda \to +\infty$ the function $F_2^{(\Delta,\lambda)}(t,1,2)$ approaches a finite limit. This requires that the correlation function of the force (5) have a finite limit as $\lambda \to +\infty$, i.e., in connection with the equality

$$\lim_{\lambda \to +\infty} \langle \mathbf{f}^{(\Delta,\lambda)}(\mathbf{r}_1,t_1) \cdot \mathbf{f}^{(\Delta,\lambda)}(\mathbf{r}_2,t_2) \rangle = f_0^2 r_0^3 \tau_0 \delta(\mathbf{r}_1 - \mathbf{r}_2) \delta(t_1 - t_2) \lim_{\lambda \to +\infty} \lambda^{3\Delta-2} \tag{6}$$

we must set $\Delta = \Delta_\infty = 2/3$. We call attention to the fact that the analysis of the limit $\lambda \to +\infty$ on the right-hand side of Eq. (6) made it possible to replace the correlation function K of the external force by a product of delta functions.

Therefore we arrive at the conclusion that $\lim_{\lambda \to +\infty} F_2^{(2/3,\lambda)}$ is a homogeneous function (to prove the homogeneity of the function $\lim_{\lambda \to +\infty} F_2^{(2/3,\lambda)}$ it is sufficient to note that by definition of the limit $\lim_{\lambda \to +\infty} F_2^{(2/3,\lambda)} = \lim_{\lambda \to +\infty} F_2^{(2/3,\lambda\lambda')}$, where λ' is an arbitrary positive number) and the relation

$$\langle \mathbf{v}(\mathbf{r},t) \cdot \mathbf{v}(0,t) \rangle = C_1 \left(\frac{f_0^2 r_0^3 \tau_0}{r^2} \right)^{2/3} \quad \text{for} \quad r \gg \max(r_0, f_0\tau_0^2), \tag{7}$$

where C_1 is a universal constant, holds. Actually, expressing the left-hand side of Eq. (7) as an integral of the function $\lim_{\lambda \to +\infty} F_2^{(2/3,\lambda)}$ and using the homogeneity of this function, it can be shown that the correlation function under study is a power-law function of r and the exponent can be determined. We note that the power-law behavior of the right-hand side of Eq. (7) follows from the homogeneity of the function $\lim_{\lambda \to +\infty} F_2^{(2/3,\lambda)}$, while the power of r on the right-hand side of Eq. (7) is determined uniquely by the number $\Delta_\infty = 2/3$. Of course, the functional dependence in Eq. (7) is consistent with the dimension of the parameter appearing in Eq. (6). We emphasize that we have not postulated but rather

we have proved the power-law character of the right-hand side of Eq. (7). The expression (7) describes the creation of large vortices (inverse cascade) and the long-wavelength correlations associated with these vortices.

The correlation function (7) enters in the so-called Loĭtsyanskiĭ integral[6]

$$\Lambda = -\frac{1}{4\pi}\int r^2 \langle \mathbf{v}(\mathbf{r},t)\cdot\mathbf{v}(0,t)\rangle\, d^3\mathbf{r}.$$

According to Eq. (7), the Loĭtsyanskiĭ integral diverges, $\Lambda = \infty$. Therefore a correct description of the inverse cascade for the method of turbulence excitation under study leads to the conclusion that the Loĭtsyanskiĭ integral diverges. Curiously, the question of the convergence of the Loĭtsyanskiĭ integral has been studied only for isotropic turbulent motion with the correlation function (7) initially decaying exponentially rapidly at large distances, i.e., under the assumption that it is possible to produce isotropic turbulence with negligible long-wavelength correlations. Under this assumption it can be shown that the Loĭtsyanskiĭ integral remains finite during further free evolution.[6] The expression (7) shows that the assumption that large-scale vortices (inverse cascade) play a negligible role is not always valid for isotropic turbulence.

Analysis of the small-scale structure of the flow (1) and (2) reduces to taking in Eq. (4) $\Delta = \Delta_0 = -1/2$, which ensures the existence of a finite homogeneous function $\lim\limits_{\lambda\to+0} F_2^{(-1/2,\lambda)}$. Hence follows

$$\langle (\mathbf{v}(\mathbf{r},t)-\mathbf{v}(0,t))^2\rangle = C_2 f_0 r \quad \text{for} \quad r\ll\min(r_0,f_0\tau_0^2), \tag{8}$$

where C_2 is a universal constant.

To study flow on scales from r_0 to $f_0\tau_0^2$, we shall consider two limiting cases: $\gamma = f_0\tau_0^2/r_0 \ll 1$ and $\gamma = f_0\tau_0^2/r_0 \gg 1$.

4. Let $\gamma\ll1$. Let us examine F_2 for $|\mathbf{r}_1-\mathbf{r}_2|\ll r_0$. For this region of distances the correlation function (2) of the force can be set equal to

$$\langle \mathbf{f}(\mathbf{r}_1,t_1)\cdot\mathbf{f}(\mathbf{r}_2,t_2)\rangle = f_0^2 K\!\left(\frac{t_1-t_2}{\tau_0},0\right). \tag{9}$$

Let us apply to the correlation function (9) the arguments leading to Eq. (7). We note that the use of Eq. (9) guarantees that distances in the range $|\mathbf{r}_1-\mathbf{r}_2|\ll r_0$ are studied, while the limit $\lambda\to+\infty$ ensures that $|\mathbf{r}_1-\mathbf{r}_2|\gg\gamma r_0$. Thus we find that for $\gamma r_0\ll|\mathbf{r}_1-\mathbf{r}_2|\ll r_0$ the flow can be described by a homogeneous function $\lim\limits_{\lambda\to+\infty} F_2^{(-1/3,\lambda)}$ and

$$\langle (\mathbf{v}(\mathbf{r},t)-\mathbf{v}(0,t))^2\rangle = C_3(f_0^2\tau_0 r)^{2/3} \quad \text{for} \quad \gamma r_0\ll r\ll r_0, \tag{10}$$

holds, i.e., the Kolmogorov–Obukhov law holds in this range of scales. The questions of the inviscid (but with finite dissipation) limit in the Euler equation and the formation of the Kolmogorov spectrum in this case were examined in Ref. 1.

5. Let $\gamma\gg1$. Let us study F_2 for $|\mathbf{r}_1-\mathbf{r}_2|\ll f_0\tau_0^2$. In this region of scales the correlation function (2) of the force can be rewritten as

$$\langle \mathbf{f}(\mathbf{r}_1,t_1)\cdot\mathbf{f}(\mathbf{r}_2,t_2)\rangle = f_0^2 K\!\left(0,\frac{\mathbf{r}_1-\mathbf{r}_2}{r_0}\right), \tag{11}$$

since according to Eq. (8) the characteristic value of the velocity of the Lagrangian particles of the fluid is not less than $(f_0 r_0)^{1/2}$ and a Lagrangian particle traverses in a time of the order of τ_0 a distance of the order of $\gamma^{1/2} r_0$.

Arguments similar to those presented in the preceding section show that for $r_0 \ll |\mathbf{r}_1 - \mathbf{r}_2| \ll \gamma r_0$ the homogeneous function $\lim_{\lambda \to +\infty} F_2^{(-1/4, \lambda)}$ can be used to describe turbulent fluid flow, and in addition

$$\langle \mathbf{v}(\mathbf{r}, t) \cdot \mathbf{v}(0, t) \rangle = C_4 \left(\frac{f_0^2 r_0^3}{r} \right)^{1/2} \quad \text{and} \quad r_0 \ll r \ll \gamma r_0. \tag{12}$$

Therefore the structure of turbulent flow in the region of spatial scales from r_0 to $f_0 \tau_0^2$ is determined by the value of the parameter $\gamma = f_0 \tau_0^2 / r_0$.

6. We shall now take account of the existence of a finite viscosity ν in the problem, i.e., the existence of another characteristic scale — the viscous length. We shall show that the energy dissipated per unit time and per unit mass (the specific dissipation rate ϵ) is determined by a new dimensionless parameter

$$\Gamma = \gamma^{4/3} \text{Re}, \tag{13}$$

where $\text{Re} = r_0 (f_0^2 r_0 \tau_0)^{1/3} / \nu$ for $\gamma \ll 1$ and $\text{Re} = r_0 (f_0 r_0)^{1/2} / \nu$ for $\gamma \gg 1$. We shall examine in detail three different cases that can arise in turbulent flows ($\text{Re} \gg 1$).

7. According to Eqs. (8) and (10), for $\gamma \ll 1$ and $\Gamma \ll 1$ the viscous length exceeds $f_0 \tau_0^2$, i.e., the Kolmogorov spectrum adjoins the viscous range. The specific dissipation rate ϵ in this case, estimated as the viscous losses on scales of the order of the viscous length, is

$$\epsilon \sim f_0^2 \tau_0, \tag{14}$$

i.e., it does not depend on the viscosity (compare with Eq. (10)).

8. Once again let $\gamma \ll 1$ but now $\Gamma \gg 1$. Then it follows from Eqs. (8) and (10) that $f_0 \tau_0^2$ is substantially greater than the viscous length, i.e., the Kolmogorov spectrum is separated from the viscous range by the spectrum (8). The specific dissipation rate can then be estimated as

$$\epsilon \sim \nu^{1/3} f_0^{4/3}, \tag{15}$$

i.e., it is approximately $\text{Re}^{1/3}$ times smaller than the energy flux along the Kolmogorov segment of the spectrum.

To understand the physical meaning of expression (15), we note that the external force $\mathbf{f}(\mathbf{r}, t)$ interacts most effectively with fluid pulsations which either have a ''resonant'' wave number $k \sim 1/r_0$ or a ''resonant'' frequency $\omega \sim 1/\tau_0$ ($k \sim 1/f_0 \tau_0^2$). According to Eqs. (14) and (15), the pulsations which are in ''spatial resonance'' with an external force are excited efficiently (they are ''in phase'' with the external force and the latter ''pumps'' them efficiently). On the Kolmogorov segment of the spectrum energy flows to modes which are in ''temporal resonance'' and ''oscillate'' in ''antiphase'' with the external force, i.e., the external force ''quenches'' oscillations with $k \sim 1/f_0 \tau_0^2$ and ''takes energy'' from these modes. Therefore the external force can be said to act simultaneously

as a source of energy and a ''sink'' for energy. Therefore, for $\gamma \ll 1$ and $\Gamma \gg 1$ dissipation is ''switched off'' in the fluid. This could be important in the theory of flapping flight and critical Reynolds numbers.

From the practical standpoint it is important that the decrease of resistance (the critical Reynolds number) associated with the ''switching off'' of viscous dissipation according to Eq. (15), even arises as the source intensity increases, i.e., without any additional requirements on the change of the structure of the boundary.

9. For $\gamma \gg 1$ the quantity Γ always satisfies the inequality $\Gamma \gg 1$. It is easy to show that in this case the specific dissipation rate is determined by expression (15).

10. Taking account of the scaling (8) in the ''switching off'' of dissipation in a turbulent fluid, we shall now determine the integral of motion with which this scaling can be associated, i.e., we shall indicate for an ideal fluid the conserved quantity whose density has the same units as f_0. This quantity is the helicity $G = \int \mathbf{v} \cdot \mathrm{curl}\, \mathbf{v}\, d^3 \mathbf{r}$. Therefore the formation of Eq. (8) and the switching off of dissipation could be due to helicity fluctuations near the viscous range (the so-called I invariant[7]).

We are deeply grateful to S. I. Anisimov and É. I. Yurchenko for their interest in this work and for a helpful discussion.

[1] S. Moiseev and O. Onishenko, Physica B **228**, 83 (1996).

[2] S. N. Gordienko, Fiz. Plazmy, in press.

[3] S. N. Gordienko, Zh. Éksp. Teor. Fiz. **106**, 436 (1994) [JETP **79**, 241 (1994)].

[4] M. A. Leontovich, Zh. Éksp. Teor. Fiz. **5**, 211 (1935).

[5] S. N. Gordienko and É. I. Yurchenko, JETP Lett. **67**, 668 (1998).

[6] L. D. Landau and E. M. Lifshitz, *Fluid Mechanics*, Pergamon Press, New York [Russian original, Nauka, Moscow, 1986].

[7] A. V. Belyan, S. S. Moiseev, and O. G. Chkhetiani, *Turbulent Viscosity in Helicoidal Turbulence* [in Russian], Institute of Space Research, Russian Academy of Sciences, Moscow, 1992, ß 1845.

Translated by M. E. Alferieff

Spectrum of polariton excitations of a two-dimensional electron plasma in a magnetic field

V. V. Popov,[a] T. V. Teperik, and G. M. Tsymbalov

Saratov Branch of the Institute of Radio Engineering and Electronics,
Russian Academy of Sciences, 410019 Saratov, Russia

Polariton excitations associated with magnetoplasma and cyclotron oscillations in a two-dimensional (2D) electron plasma are studied. In contrast to previous works by other authors, it is concluded that there exists a low-frequency nontransmission band in the spectrum of 2D surface magnetoplasma polaritons. Radiative polariton excitations associated with nonuniform cyclotron oscillations of electrons in a 2D system are investigated. © *1998 American Institute of Physics.* [S0021-3640(98)00815-9]

PACS numbers: 73.50.Jt, 52.40.Db

The term ''polariton'' ordinarily refers to an electromagnetic wave whose spectrum is due to the interaction of an electromagnetic field with a characteristic elementary excitation of the system.[1] In the present letter we study polaritons associated with plasma and cyclotron oscillations in a uniform two-dimensional (2D) electron layer in an external magnetic field H_0 perpendicular to the plane of the layer. The spectrum of characteristic oscillations of such a system if one does not take into account the interaction of the oscillations with transverse electromagnetic fields (electrodynamic retardation effects) is well known (see, for example, Ref. 2) and consists of a uniform cyclotron motion of electrons with frequency

$$\omega = \omega_c = |e| H_0 / m^* c \tag{1}$$

and nonuniform 2D magnetoplasma oscillations at frequency

$$\omega = (\omega_p^2 + \omega_c^2)^{1/2}, \tag{2}$$

where

$$\omega_p = \left[\frac{4 \pi e^2 N_s k}{m^*(\varepsilon_1 + \varepsilon_2)} \right]^{1/2}$$

is the frequency of plasma oscillations in a zero magnetic field, k is the modulus of the two-dimensional wave vector in the plane of the 2D system, e and m^* are, respectively, the electron charge and effective mass, and ε_1 and ε_2 are the permittivities of the media at whose flat interface the 2D electron layer is located. It follows from Eqs. (1) and (2)

210

that characteristic oscillations with frequencies below the cyclotron frequency ω_c do not exist in a 2D plasma. In other words, The spectrum of magnetoplasma oscillations (2) contains a gap at low frequencies $0 < \omega < \omega_c$.

In Refs. 3 and 4 it was shown that in the system under study magnetoplasma polariton excitations arise at frequencies below the cyclotron frequency when electrodynamic retardation effects are taken into account. The dispersion curves of 2D magnetoplasma polaritons lie to the right of the straight line $\omega = ck/\sqrt{\varepsilon_1}$ ($\varepsilon_1 \geqslant \varepsilon_2$). This signifies that 2D magnetoplasma polaritons are essentially nonradiating surface electromagnetic waves. In the region of large values of the wave numbers the dispersion of 2D magnetoplasma polaritons can be described to a high degree of accuracy by Eq. (2), obtained in the electrostatic approximation. The dispersion curves presented in Refs. 3 (for the case $\varepsilon_1 = \varepsilon_2$) and 4 (for $\varepsilon_1 \neq \varepsilon_2$) arrive at the point $\omega = 0$ as $k \to 0$. At the same time, the results of the calculations performed in Ref. 5 attest to the presence of a low-frequency gap in the spectrum of magnetoplasma oscillations at the surface of an ionic crystal with a 2D electron layer. Unfortunately, the final formulas obtained in Ref. 5 do not permit passing to the limiting case of frequency-independent permittivity. This creates the impression that the low-frequency gap in the spectrum of 2D magnetoplasma polaritons arises only as a result of the fact that in Ref. 5 the frequency dependence of the dynamic permittivity of the ionic crystal is taken into account. Actually, as will be shown below, a low-frequency gap is also present in the spectrum for $\varepsilon_{1,2} = $ const, if $\varepsilon_1 \neq \varepsilon_2$ and $\omega_c \neq 0$.

In contrast to magnetoplasma oscillations, uniform cyclotron motion of electrons in the plane of a 2D system must be accompanied by electromagnetic radiation from the cyclotron currents into the surrounding media. The complex frequency of a uniform ($k = 0$) cyclotron oscillation, taking account of radiation damping was calculated in Ref. 6. In the present letter we investigate nonuniform radiating cyclotron oscillations (radiating polaritons). These oscillations can be described only on the basis of an electrodynamic approach.

We shall assume that the 2D electron layer lies in the plane $z = 0$ at the interface of two media with permittivities ε_1 and ε_2. The z axis is directed along the external magnetic field into the medium 2. We choose the spatiotemporal dependence of the fields in the media to be of the form $\exp(-i\omega t + ikx \pm \alpha_{1,2}z)$, where the upper and lower signs in front of the transverse wave numbers $\alpha_{1,2}$ refer, respectively, to media 1 and 2. The fields are assumed to be uniform in the y direction.

The dispersion relation describing polariton excitations in our structure is obtained by solving Maxwell's equations in the media 1 and 2 with boundary conditions in the plane $z = 0$, which take account of the response of the magnetoactive 2D electron plasma. Since the procedure for obtaining the dispersion relation is quite standard, we immediately give the final result:

$$\frac{\alpha_2}{\alpha_1}(1 - Z_1\sigma_1) + \frac{\alpha_1\varepsilon_2}{\alpha_2\varepsilon_1}(1 + Z_2\sigma_1) + \frac{\varepsilon_2}{\varepsilon_1}[(1 + Z_2\sigma_1)(1 - Z_1\sigma_1) - Z_1Z_2\sigma_2^2] + 1 = 0,$$

$$(3)$$

where

$$\alpha_{1,2} = \pm \sqrt{k^2 - \left(\frac{\omega}{c}\right)^2 \varepsilon_{1,2}}, \quad Z_1 = i \frac{4\pi\omega}{\alpha_2 c^2}, \quad Z_2 = i \frac{4\pi\alpha_2}{\omega\varepsilon_2}. \tag{4}$$

The components $\sigma_{1,2}$ of the conductivity tensor of an electron plasma in a magnetic field are determined in the local approximation (the Drude model) by the expressions

$$\sigma_1 = \frac{e^2 N_s}{m^*} \frac{(1 - i\omega\tau)\tau}{(\omega_c\tau)^2 + (1 - i\omega\tau)^2}; \quad \sigma_2 = \frac{e^2 N_s}{m^*} \frac{\omega_c\tau^2}{(\omega_c\tau)^2 + (1 - i\omega\tau)^2},$$

where τ is the phenomenological momentum relaxation time of electrons in the 2D electron layer. We note that the dispersion relations obtained in Refs. 3–5 can be put into the form (3). However, to investigate the solutions $\omega(k)$ of the system (3) and (4) the choice of the signs in front of the radicals in the expressions for the transverse wave numbers $\alpha_{1,2}$, which is made on the basis of physical considerations, is important. At the same time, this question was essentially not discussed in Refs. 3–5.

Neglecting electron scattering ($\tau \to \infty$), the dispersion relation (3) can be put into the form

$$\left(\omega^2 - \frac{\eta_0 \alpha_1 \alpha_2}{\alpha_1 \varepsilon_2 + \alpha_2 \varepsilon_1}\right)\left(1 + \frac{\eta_0}{(\alpha_1 + \alpha_2)c^2}\right) - \omega_c^2 = 0, \tag{5}$$

where $\eta_0 = 4\pi N_s e^2 / m^*$.

Let us consider first the surface magnetoplasma polaritons by investigating Eqs. (4) and (5). In this case the real solutions $\omega(k)$ are sought. The transverse wave numbers $\alpha_{1,2}$ must be real and positive, which corresponds to the field of the wave decaying away from the 2D electron layer in both media and absence of electromagnetic radiation in a direction transverse to the plane of the 2D electron layer. It is obvious that these conditions hold only if $k > \omega\sqrt{\varepsilon_1}/c$ and if the positive signs are chosen in front of the radicals in Eqs. (4) (for definiteness, we take $\varepsilon_1 \geq \varepsilon_2$). Hence it follows that for any positive wave number k the frequency of the surface wave, determined as the root of Eq. (5), lies in the segment $0 \leq \omega \leq \omega_1$, where $\omega_1 = ck/\sqrt{\varepsilon_1}$. If this root exists (and is unique), then the left-hand side of Eq. (5), (which we denote by $f(k,\omega)$) should have different signs for $\omega = 0$ and $\omega = \omega_1$. From Eq. (5) it follows, taking account of the expressions chosen for $\alpha_{1,2}$, that

$$f(k,0) = -\left[\omega_c^2 + \frac{\eta_0 k}{\varepsilon_1 + \varepsilon_2}\left(1 + \frac{\eta_0}{2kc^2}\right)\right] < 0$$

for any $k \geq 0$. At the same time,

$$f(k,\omega_1) = \left[\frac{k^2 c^2}{\varepsilon_1}\left(1 + \frac{\eta_0}{c^2 k}\sqrt{\frac{\varepsilon_1}{\varepsilon_1 - \varepsilon_2}}\right) - \omega_c^2\right] > 0$$

only in the region $k_0 \leq k < \infty$, where

$$k_0 = \frac{1}{2}\left[\sqrt{a^2 + \frac{4\omega_c^2 \varepsilon_1}{c^2}} - a\right], \quad a = \frac{\eta_0}{c^2}\sqrt{\frac{\varepsilon_1}{\varepsilon_1 - \varepsilon_2}}. \tag{6}$$

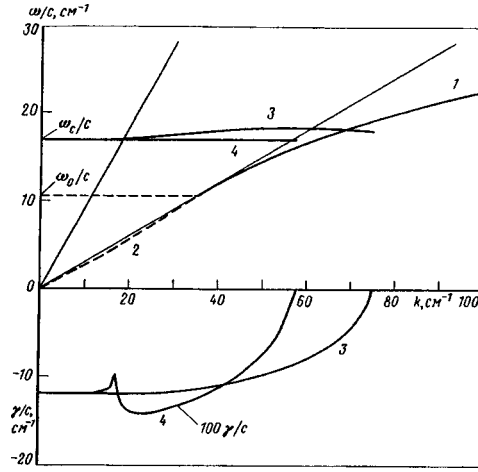FIG. 1. Dispersion curves of 2D magnetoplasma and cyclotron polaritons: *1* — Surface magnetoplasma polaritons; *2* — ''pseudosurface'' polaritons; *3,4* — cyclotron polaritons; N_s, cm^{-2}:10^{12} (*1,2,3*); 10^{10} (*4*). $m^* = 0.07 m_0$, where m_0 — mass of a free electron. Thin solid lines: $\omega = kc/\sqrt{\varepsilon_{1,2}}$ ($\varepsilon_1 = 12.8$; $\varepsilon_2 = 1$).

For $k = k_0$ the root of Eq. (5) $\omega = \omega_0 = ck_0/\sqrt{\varepsilon_1}$ and, as follows from expression (4), $\alpha_1 = 0$.

Figure 1 displays a plot of the dispersion curve obtained for 2D surface magnetoplasma polaritons (curve *1*) by solving Eq. (5) numerically by the method of dividing the segment $[0, \omega_1]$ in half. We note that the systematic application of the procedure of halving the segment makes it possible to conclude that the root of Eq. (5) with $\alpha_{1,2} > 0$ is unique. The dispersion curve *1* terminates at the point (k_0, ω_0), touching the straight line $\omega = kc/\sqrt{\varepsilon_1}$. It follows from Eq. (6) that $k_0 = 0$ (and therefore also $\omega_0 = 0$) only if $\omega_c = 0$ or $\varepsilon_1 = \varepsilon_2$ ($\lim_{\varepsilon_1 \to \varepsilon_2} k_0 = 0$). The condition $\omega_0 < \omega_c$ holds for any values of ω_c and $\varepsilon_{1,2}$. Curves of ω_0 versus the magnetic field for different values of ε_1 and $\varepsilon_2 = 1$ are presented in Fig. 2.

We note that a real solution of the dispersion relation (5) can be formally obtained also in the region of wave numbers $0 < k < k_0$ (curve *2* in Fig. 1). However, this solution is obtained only if the minus sign is chosen in front of the radical in Eq. (4) for α_1. It is obvious that such a solution is physically meaningless, since it corresponds to ''pseudosurface'' waves whose field grows exponentially in the medium 1 away from the 2D electron layer. It is possible that in Ref. 4 this solution was also adopted as a continuation of the dispersion branch of surface waves, which led the author to the erroneous conclusion that there is no low-frequency gap in the spectrum of 2D magnetoplasma polaritons.

Let us now study radiating polaritons, associated with cyclotron oscillations of electrons in the 2D system. The dispersion curves for these polaritons (curves *3* and *4* in Fig. 1) are obtained by switching to complex frequencies $\omega \to \tilde{\omega}$, where $\tilde{\omega} = \omega + i\gamma$ in Eqs. (4) and (5) and taking the minus signs in front of the radicals in Eq. (4). The dispersion curves $\omega(k)$ of the cyclotron polaritons lie essentially completely in the region $\omega > kc/\sqrt{\varepsilon_1}$. The imaginary part of the frequency γ is the radiation damping constant of the
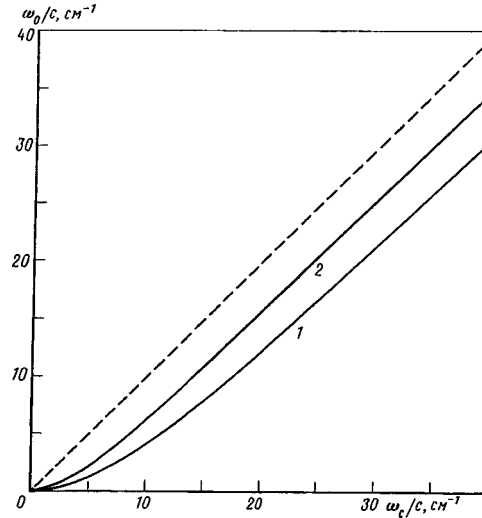
FIG. 2. Limiting frequency ω_0 versus the magnetic field $\omega_c(H_0)$ with $\varepsilon_2 = 1$ and ε_1: 3.8 (curve *1*) and 12.8 (curve *2*). Dashed line: $\omega_0 = \omega_c$.

oscillations. For radiating polaritons $\alpha_{1,2}$ are complex quantities. Here $\mathrm{Re}\,\alpha_{1,2} < 0$, which corresponds to the amplitudes of the electromagnetic field in both media increasing away from the 2D electron layer, while the signs of the imaginary parts of α_1 and α_2 ($\mathrm{Im}\,\alpha_{1,2} < 0$) correspond to outgoing electromagnetic waves from the 2D electron layer in media 1 and 2. Such an amplitude–phase pattern of the field is characteristic for characteristic radiating oscillations in open electrodynamic systems.[7] The high amplitude of the electromagnetic field at points located farther away from a plasma layer arises because of the fact that the radiation field arriving at these points at a given moment in time is due to radiative decay of oscillations in the 2D system at earlier times, when the amplitude of these oscillations was larger.

One can see from Fig. 1 that radiation damping of the cyclotron polaritons increases practically as the surface electron density. As the density increases, the dispersion curve $\omega(k)$ of cyclotron polaritons penetrates farther into the region $k > \omega \sqrt{\varepsilon_1}/c$. For small values of N_s a minimum of the radiation damping arises for a value of the wave number corresponding to the point of intersection of the dispersion curve $\omega(k)$ of a cyclotron polariton and the straight line $\omega = ck/\sqrt{\varepsilon_2}$ characterizing the dispersion of an uniform plane wave in the medium 2. The lower the surface electron density, the deeper the minimum is. The physical reason for the appearance of a minimum of the radiation damping is as follows. At low electron density the radiation damping is much lower than the characteristic frequency of the oscillations. It follows from expression (4) that in this case $\mathrm{Re}\,\alpha_2 \ll \mathrm{Im}\,\alpha_2$, i.e., the field in medium 2 is an almost uniform plane wave, emitted at an angle $-\tan^{-1}(\mathrm{Im}\,\alpha_2/k)$ with respect to the plane of the 2D system. For $\omega = ck/\sqrt{\varepsilon_2}$ we obtain, taking account of the relation (4), $\tan^{-1}(\mathrm{Im}\,\alpha_2/k) \simeq 0$, which corresponds to the emission of a wave along the axis of dipoles which are formed as a result of the nonuniform oscillations of electrons in the plane of the 2D system. It is obvious

that in this case the intensity of the electromagnetic radiation decreases (it is proportional to the radiation damping of the characteristic oscillations).

In the terminology introduced in Ref. 8, the radiating cyclotron oscillations can be classified as virtual polaritons. These excitations cannot exist in the system for a sufficiently long time, since they are subjected to radiative decay, but they can be observed in the form of absorption resonances in the transmission spectrum of an external electromagnetic wave passing through a 2D electron layer. In this case, oblique incidence of a wave must be used in order to excite nonuniform cyclotron oscillations.

[a]e-mail: popov@ire.saratov.su

---

[1] V. M. Agranovich and D. A. Mills (eds.), *Surface Polaritons*, Elsevier, New York, 1982 [Nauka, Moscow, 1985].

[2] V. B. Shikin, Zh. Éksp. Teor. Fiz. **98**, 2086 (1990) [Sov. Phys. JETP **71**, 1172 (1990)].

[3] K. W. Chiu and J. J. Quinn, Phys. Rev. B **9**, 4724 (1974).

[4] M. S. Kushwaha, Solid State Commun. **67**, 993 (1988).

[5] Kh. K. Granada, Yu. A. Kosevich, and A. M. Kosevich, JETP Lett. **14**, 747 (1988).

[6] O. R. Matov, O. F. Meshkov, O. V. Polishchuk, and V. V. Popov, Zh. Éksp. Teor. Fiz. **109**, 876 (1996) [JETP **82**, 471 (1996)].

[7] L. A. Vaĭnshteĭn, *Open Resonators and Open Waveguides* [in Russian], Sov. Radio, Moscow, 1966.

[8] A. Harstein, E. Burstein, J. J. Brion, and R. F. Wallis, Solid State Commun. **12**, 1083 (1973).

Translated by M. E. Alferieff

Size effect in the resistance of narrow superconducting BSCCO (2212) whiskers near the Berezinskiĭ–Kosterlitz–Thouless transition

I. G. Gorlova,[a] S. G. Zybtsev, A. M. Nikitina, and V. Ya. Pokrovskiĭ

Institute of Radio Engineering and Electronics, Russian Academy of Sciences, 103907 Moscow, Russia

V. N. Timofeev

A. A. Baĭkov Institute of Metallurgy, Russian Academy of Sciences, 117911 Moscow, Russia

S. Aukkaravittayapun[b]

Department of Physics, University of Nottingham, Nottingham NG7 2RD, UK

The temperature dependence of the resistance and the current–voltage characteristics are measured for $Bi_2Sr_2CaCu_2O_x$ whiskers of different width, including whiskers possessing a width step. As the width decreases, the resistivity of the whiskers below the Berezinskiĭ–Kosterlitz–Thouless transition temperature increases, while above the transition it decreases. This effect is explained by two-dimensional vortices leaving the sample through its edge and confirms the existence of vortex pairs in layered high-T_c superconductors. © *1998 American Institute of Physics.* [S0021-3640(98)00915-3]

PACS numbers: 74.72.Hs, 74.25.Fy

A Berezinskiĭ–Kosterlitz–Thouless (BKT) type of transition is observed in the most highly anisotropic high-T_c superconducting compounds (HTSCs) — $Bi_2Sr_2CaCu_2O_x$ and $Tl_2Sr_2CaCu_2O_x$ (see Ref. 1). The transition occurs at a temperature T_C which is 2–3 K lower than the Ginzburg–Landau superconducting transition temperature T_{C0}.[2,3] For $T_C < T < T_{C0}$ free two-dimensional magnetic vortices arise in the superconducting layers, which causes the samples to have a finite resistance. Below T_C vortex–antivortex pairs arise in fluctuation processes. A nonzero electric current I can result in breaking of the pairs and the appearance of free vortices. If a pair reaches a critical size r_0, which depends on the current and temperature, as a result of a thermal fluctuation, then dissociation of the vortices occurs. At zero current the binding energy of a pair in the BKT model is proportional to the logarithm of the distance between the vortices, i.e., thermal pair breaking is impossible, and as $I \rightarrow 0$ the resistance also tends to zero. However, the situation changes if the finite dimensions of the sample are taken into account. If the size of a vortex–antivortex pair reaches the width of the sample, one vortex will leave the

sample, while the other will become free, and its dissipative motion under the influence of the current gives rise to a resistance. Such a process was studied theoretically in Ref. 4, where it was shown that the finite resistance

$$R = 4\pi^{3/2} R_0 [\Gamma(1+a/2)/\Gamma(1/2+a/2)](\pi\xi/w)^a, \tag{1}$$

where w is the width of the sample, R_0 is the normal-state resistance, $\xi(T)$ is the coherence length, and $a = 2(T_{C0}-T)/(T_{C0}-T_C)$, is observed in sufficiently narrow samples below T_C. At the same time, additional barriers at the boundaries of the sample, which prevent the vortices from escaping,[5] can lead to the opposite effect also — a sharper drop of the resistance and a finite critical current in narrow samples. We note that an increase in the critical current with a decrease of the cross section of $Bi_2Sr_2CaCu_2O_x$ whiskers has been observed at liquid-helium temperatures.[6]

Our work is devoted to searching for and investigating the dependence of the conducting properties of $Bi_2Sr_2CaCu_2O_x$ crystals near the superconducting transition on their width. We chose filamentary single crystals (whiskers) as the object of investigation. The whiskers were grown, by the method described in Ref. 6, from a quenched charge at temperature 855 °C in an oxygen flow in powders of ultrapure oxides Bi_2O_3 (99.999%), $SrCO_3$ (99.999%), $CaCO_3$ (99.999%), and CuO (99.99%), mixed in the ratio Bi:Sr:Ca:Cu = 1.5:1:1:2. The width of the whiskers grown varies over wide limits, while the narrowest whiskers have a width of about 1 μm, which, according to relation (1), could be sufficient for observing excess resistance.

We investigated the temperature dependences of the resistance of 14 single-phase whiskers of width 1–10 μm. Comparing the forms of the transitions in these samples showed that, as a rule, the resistance below T_{C0} drops more slowly in the narrowest whiskers ($w < 3$ μm). However, the variance in T_{C0} and the small variations in the form of the dependence $R(T)$ above T_{C0} as well as individual structural defects in the samples did not permit reaching an unequivocal conclusion. To determine the effect of the whisker width on the form of the superconducting transition it was necessary to compare whiskers having identical compositions and structure but different widths. We noted that some of the whiskers grown have a width step of constant thickness (Fig. 1). Investigation of four such samples in a transmission electron microscope showed that they are single crystals, and the crystallographic orientation is identical on both sides of a step (Fig. 1b). A defect is usually observed near a step (a dislocation in the sample presented in Fig. 1b), but the defect structure does not differ much in the wide and narrow parts of a sample. For this reason, as will become clear below, comparing the conducting properties of such samples on different sides of a step made it possible to observe the differences due to the whisker width.

We investigated three samples with a width step. All dimensions of these samples were determined after measurements with a scanning electron microscope (SEM). All three samples were about 0.15 μm thick. Five silver contacts were deposited on each sample. Four-probe measurements of the conducting properties of sectors 2–3 and 3–4 on different sides of the step were performed on these samples (see Fig. 1a). Contact No. 3 covered the region of the step. The sectors were 70–120 μm long. To measure $R(T)$ an ac current was passed through the contacts 1–5, and the voltages between the contact pairs 2–3 and 3–4 were measured simultaneously with two synchronous detectors. Virtually identical temperature dependences of the resistivity $R(T)$ were observed above
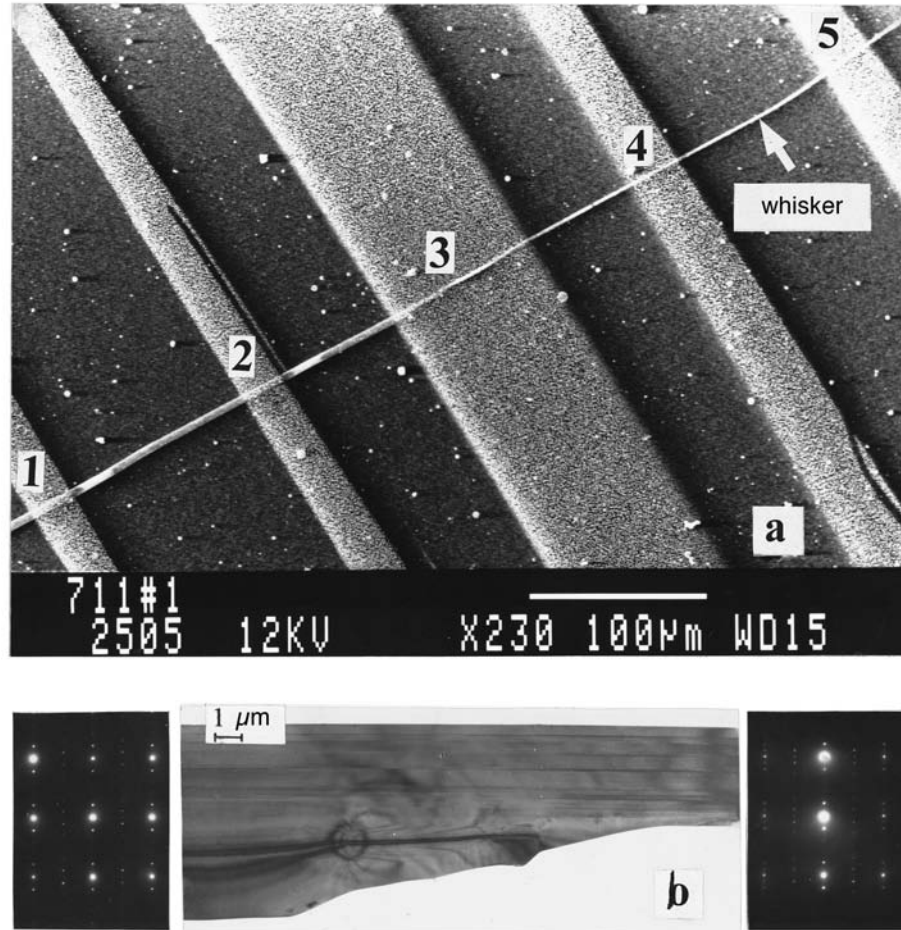
FIG. 1. a) SEM photograph of the arrangement of sample No. 1 with a width step. The numbers 1–5 designate contact strips. b) Light-field photomicrograph of one of the samples near a width step in the reflection (020). The diffraction patterns of the corresponding parts of the sample are presented on the left- and right-hand sides.

T_{C0}, but below T_C the resistivity was observed to drop off more slowly in narrow sectors. Figure 2a displays the temperature dependences of the resistance for two sectors of sample No. 1: $R_{23} \equiv R_W$ and $R_{34} = R_N$. The resistance R_W of the wide sector is multiplied by 2.65, which corresponds to the width ratio of the samples w_{23}/w_{34}: $w_{23} = 4.3\,\mu$m and $w_{34} = 1.6\,\mu$m. As one can see from the figure, the dependences are identical in the interval from room temperature almost up to T_{C0}. The temperature $T_{C0} \approx 77$ K for both sectors can be estimated from the maximum of dR/dT. However, below the transition in a narrow part of the sample the resistance is observed to drop off more slowly. This is clearly seen in Fig. 2b, where the same dependences $R(T)$ are presented on a semiloga-rithmic scale in the region of the dropoff of the resistances. One can see that the depen-dences are qualitatively different: In the wide sector a critical dropoff of the resistance $R_W \propto \exp[-C/(T-T_{C0})^{1/2}]$, characteristic for a BKT transition (with $T_C \approx 73.4$ K, dashed
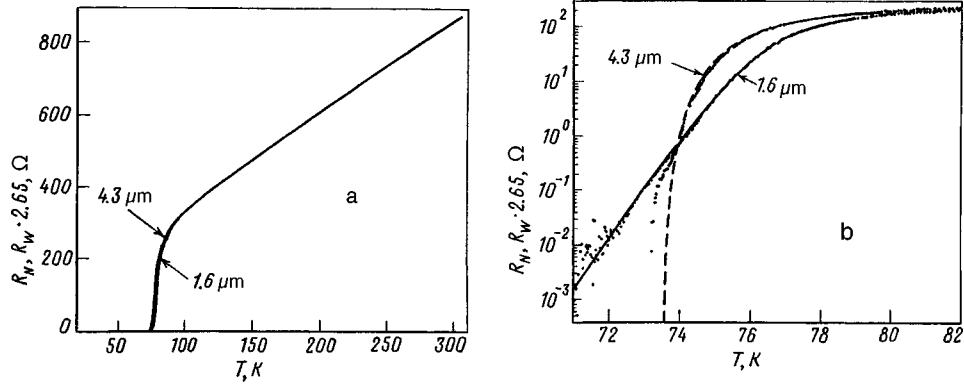
FIG. 2. Temperature dependences of the resistance of the wide and narrow sectors of sample No. 1: a) on a linear scale, b) on a semilogarithmic scale near $T=T_{C0}$. The dashed curve represents the dependence $R_W = 1.2 \times 10^3\ \Omega \cdot \exp[-6.2(T-73.4\ \text{K})^{-1/2}]$. The solid line represent Eq. (1) with $\xi(0) = 85$ Å, $T_{C0} = 76.5$ K, $T_C = 73.4$ K, $\xi(T) = 0.74\xi(0)/(1-T/T_{C0})^{1/2}$.

curve in Fig. 2b) is observed, whereas in the narrow sector the resistance drops off more slowly. The solid line in Fig. 2b shows the approximation of $R_N(T)$ by expression (1). The quantity R_0 in Eq. (1) was obtained by using an approximate Bardeen–Stefan relation $R \sim R_0 \xi^2 n_f$, where n_f is the density of free vortices. In order of magnitude, R_0 equals the normal-state resistance.

The temperature dependences $R(T)$ in the wide and narrow sectors of the samples No. 2 ($w_{23} = 4.4\ \mu$m, $w_{34} = 2.6\ \mu$m) and No. 3 ($w_{23} = 14\ \mu$m, $w_{34} = 3.9\ \mu$m) showed a similar correspondence. The coherence length $\xi(0)$ can be estimated by comparing $R_N(T)$ with relation (1) varying T_{C0}, T_C, and R_N over reasonable limits. In all three samples the values of $\xi(0)$ agree in an order of magnitude with the data available for BSCCO ($\xi(0) \sim 50$ Å). Therefore $R(T)$ in narrow samples deviates from the dependence characteristic for a BKT transition, and the dropoff of $R(T)$ is described well by relation (1).

We note that above T_C the screening of vortex pairs by free vortices must be taken into account. Indeed, at $T = T_C$ it follows from Eq. (1), taking account of the Bardeen–Stefan ratio, that $\sqrt{n_f} \sim 1/w$, i.e., the distance between the vortices is of the order of the width of the sample, and relation (1) is no longer applicable. As one can see from Fig. 2b, somewhat above T_C the curves $R(T) \times w$ for the narrow and wide sectors intersect, and subsequently the resistance of the narrow sector is less than that of the wide sector. The same thing is observed in samples Nos. 2 and 3. We note that relation (1) explains only the growth of the resistivity with decreasing w. We assume that the decrease in R for $T_{C0} < T < T_C$ can be explained qualitatively by the fact that the sample edges provide an additional possibility not only for breaking of vortex pairs but also for escape of free vortices. The equilibrium value of n_f, which for $T_{C0} < T < T_C$ is established by pair generation and recombination processes, can decrease as a result of an outflow through the edges, and in consequence the resistivity of the narrow sample is lower than that of the wide sample.

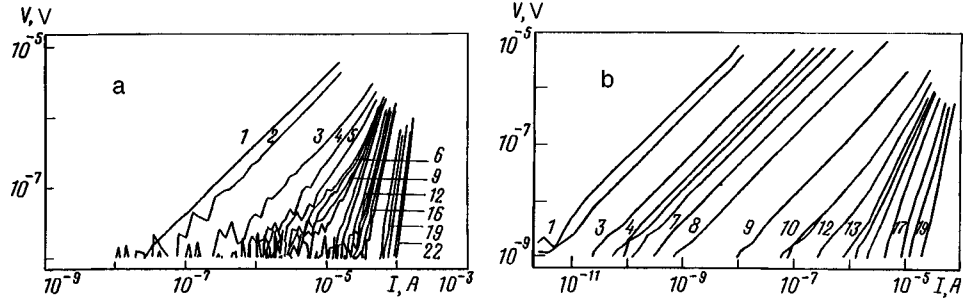The ratio of R_N and R_W also remains the same at temperatures several degrees above

FIG. 3. IVCs of whiskers: a) of width 10 μm at temperatures: *1* – 82.51 K, *2* – 79.75 K, *3* – 76.77 K, *4* – 75.94 K, *5* – 75.84 K, *6* – 75.69 K, *7* – 75.6 K, *8* – 75.5 K, *9* – 75.4 K, *10* – 75.31 K, *11* – 75.23 K, *12* – 75.03 K, *13* – 74.87 K, *14* – 74.85 K, *15* – 74.71 K, *16* – 74.5 K, *17* – 74.34 K, *18* – 72.16 K, *19* – 71.71 K, *20* – 71.2 K, *21* – 70.36 K, *22* – 70.05 K; b) of width 1.5 μm at temperatures: *1* – 84.95 K, *2* – 78.5 K, *3* – 75.2 K, *4* –74.1 K, *5* – 73.5 K, *6* – 72.7 K, *7* – 71.8 K, *8* – 71.2 K, *9* – 70.6 K, *10* – 70.34 K, *11* – 70.33 K, *12* – 70.25 K, *13* – 70.18 K, *14* – 70.15 K, *15* – 71.06 K, *16* – 70.01 K, *17* – 69.8 K, *18* – 69.67 K, *19* – 69.44 K.

T_{C0}. A similar effect (lower excess conductivity in wide samples) was noted in Ref. 6, but it was shown later[7] that it is due predominately to the presence of defects: twins or polycrystalline layer on the surface. In our case the effect is an order of magnitude weaker than in Ref. 6, and it is observed in a narrower temperature range: As T increases above 90 K, R_{34} and R_{23} are virtually identical, in contrast to the results of Ref. 6.

A characteristic feature of the BKT transition below T_C is the power-law character of the current–voltage characteristics (IVCs), $R \propto I^a$, and the dependence of the exponent $a(T)$ with a jump from $a=2$ to $a=0$ at $T=T_C$ (Nelson–Kosterlitz jump).[2] The existence of a resistance tail in narrow samples signifies that in these samples, for sufficiently low currents, the IVCs are of an Ohmic character, i.e., the derivative $d\log(R)/d\log(I)$ remains equal to zero below T_C also. As current increases, the critical pair size $r_0(I)$ decreases. When the current density reaches

$$j_0 \sim \pi ckT/\Phi_0 dw \tag{2}$$

(d is the thickness of the two-dimensional layer, c is the speed of light, Φ_0 is the magnetic flux quantum, and k is Boltzmann's constant), r_0 becomes equal to w. As the current increases further, the sample width no longer influences pair breaking.[6] For samples Nos. 1 and 2, Eq. (2) gives $j_0 = 10^5$ and 6×10^4 A/cm^2, respectively. Indeed, at these currents we observed a deviation of the IVC from Ohm's law. We were not able to perform measurements of the IVCs on these samples at sufficiently high currents, but among the experimental samples we were able to find a pair of whiskers, wide and narrow, where the IVCs have a power-law character and the influence of the width on the character of the IVCs is evident.

Figure 3 shows the IVCs of two samples — 10 μm wide (Fig. 3a) and 1.5 μm wide (Fig. 3b) — at different temperatures. From the maximum of dR/dT, the values of T_{C0} equal 79 K and 78 K, respectively. The dropoff of $R(T)$ in the narrow sample can be described by relation (1) with $\xi(0) \approx 50$ Å. In both samples the IVCs are described well by a power-law function. In the narrow sample, the transition to linear IVCs occurs at currents $\sim 10^{-6}$ A in the range $T \approx 70.2 - 70.6$ K, which is 7–8 K lower than T_{C0},
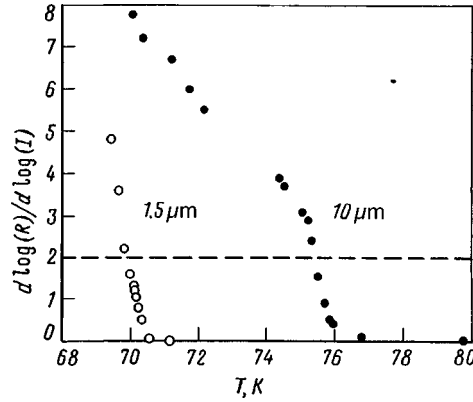
FIG. 4. Average value of $d \log(R)/d \log(I)$ as a function of T for the samples presented in Figs. 3a,b: * — w = 10 μm (averaged with $V = 10^{-6}$–10^{-7} V); $\bigcirc$ — $w = 1.5$ μm (averaged with $V = 10^{-6}$–10^{-8} V).

i.e., in the temperature range obviously below T_C, which in BSCCO should be 2–3 K below T_{C0}.[2] The corresponding quantity $j_0 \sim 10^{3-4}$ A/cm^2 is close to the estimate (2).

The curves $d \log(R)/d \log(I)$ versus T, obtained from the IVCs (Fig. 3), are displayed in Fig. 4. In the wide sample, the dependence is characteristic for a BKT transition with a somewhat broadened Nelson–Kosterlitz jump at $T_C \approx 75.7$ K. In the narrow sample, the exponent grows much more sharply, and at low temperatures its value approaches the value obtained in the wide sample. This indicates that at low temperatures and high currents the width of the sample does not influence pair breaking.

In summary, the dependence $R(T)$, just as the character of the IVCs in the most perfect samples, agrees with the theory of Ref. 4.

We note that the columnar defects (CDs) produced in BSCCO whiskers by irradiation with heavy ions[8] also lead to changes in the dependences $R(T)$ that are similar to those described above: In the irradiated sectors a smoother (exponential) dropoff of the resistance was observed below T_C, while above T_C, conversely, the resistance was lower than in the unirradiated samples. The sample with CDs can be represented as a network of narrow samples which are interconnected with one another in a complicated manner. The characteristic width of such samples equals approximately the average distances between the CDs — about 0.2 μm.[8] Substituting $w = 0.2$ μm into Eq. (1) satisfactorily describes the dependence $R(T)$ observed in Ref. 8 below T_{C0}. Therefore the effect of CDs probably reduces to the size effect, to which the present paper is devoted.

The observation of a size effect in samples of the order of several microns wide attests to the presence of vortex–antivortex pairs in them, since the characteristic radius of other possible excitations in high-T_c superconductors is incomparably shorter.

ics,'' area ''Superconductivity'' (Project 98049), and Jumelages 19 (Russian Fund for Fundamental Research 98-02-22061).

[a] e-mail: gorl@mail.cplire.ru

[b] Permanent address: National Metal and Materials Technology Center, Bangkok, 10400 Thailand

[1] P. Minnhagen, Rev. Mod. Phys. **59**, 1001 (1987).

[2] S. N. Artemenko, I. G. Gorlova, and Yu. I. Latyshev, JETP Lett. **49**, 654 (1989).

[3] S. Martin, A. T. Fiory, R. M. Fleming *et al.* Phys. Rev. Lett. **62**, 677 (1989).

[4] S. N. Artemenko and W. Wonneberger, Phys. Rev. B **47**, 12361 (1992).

[5] L. Miu, Phys. Rev. B **50**, 13849 (1994).

[6] Yu. I. Latyshev, I. G. Gorlova, A. M. Nikitina *et al.*, Physica C **216**, 471 (1993).

[7] I. G. Gorlova and V. N. Timofeev, Physica C **255**, 131 (1995).

[8] S. Aukkaravittayapun, I. G. Gorlova, P. J. King *et al.*, Czech. J. Phys. **46-S3**, 1647 (1996).

Translated by M. E. Alferieff

High-temperature superconductors as heterostructures

V. V. Kapaev and Yu. V. Kopaev[a]

P. N. Lebedev Physics Institute, Russian Academy of Sciences, 117924 Moscow, Russian

The wave-function envelope method is used to describe the electronic states of the cuprate high-T_c superconductors (HTSCs). In this method the 2D electronic states of the CuO_2 layers of a unit cell play the role of quantum wells, while the 2D states of the reservoir play the role of quantum barriers. Because of the different anisotropy of the 2D effective masses of the wells and barriers, some states on the Fermi surface (line) belong to CuO_2 layers and some states belong to the reservoir layers. This behavior of the electronic states explains characteristic features of HTSCs, such as the existence of regions on the Fermi surface with strongly different relaxation times, the weak suppression of d-type superconducting pairing by nonmagnetic scattering, and the coincidence of the angular dependence of the superconducting order parameter and the angular dependence of the electronic density of states (forward scattering predominating). The change in the signs of the components of the effective masses along the Fermi surface can result in the formation of hole pairs (biholes) or electron pairs (bielectrons) on account of the Coulomb interaction in the case of a negative reduced mass of the pairs. © *1998 American Institute of Physics.* [S0021-3640(98)01015-9]

PACS numbers: 74.76.Bz, 74.25.Jb

    The wave-function envelope method is widely used to describe the electronic states of semiconductor heterostructures, e.g., quantum wells and systems consisting of quantum wells. In this method the wave function in each layer of a heterostructure is expanded in the electron wave functions of the corresponding layer, and the Schrödinger equation, with the the effective mass of the corresponding layer appearing in the kinetic energy operator and the role of the potential energy being played by the difference in the dispersion relations of the longitudinal (along the layers) motion of the electrons in the materials of the neighboring layers, is solved for the expansion coefficients (the envelope), which depend on the coordinate along the direction normal to the layers. This method gives good quantitative agreement with experiment, even in the case of very thin (several atomic layers) quantum wells and barriers.

    This is certainly the main method for describing artificial heterostructures based on high-temperature superconductors (HTSCs).[1] However, a HTSC itself can be treated as a heterostructure.[1] The point is that according to the generally held point of view concerning cuprate HTSCs the conductivity and superconductivity in these materials are deter-

mined by the properties of the individual CuO_2 layers (LaSrCuO), CuO_2 bilayers separated by a layer of Y atoms (YBaCuO), and triple CuO_2 layers separated by layers of Ca atoms (BiSrCaCuO). Thus these layers play the role of quantum wells. The corresponding LaO, BaO, and BiO layers, however, play the role of reservoirs (barriers), on doping which, for example, with strontium atoms in LaSrCuO and oxygen atoms in YBaCuO or BiSrCaCuO, the carriers (holes) enter the CuO_2 layers. A similar situation occurs in semiconductor heterostructures when the barriers are doped.

The envelope method is quite well substantiated for HTSCs with three or more CuO_2 layers (five or more atomic layers) per unit cell, though qualitatively (and possibly quantitatively also) the main results of the present work will also hold for one and two CuO_2 layers. If instead of the envelope method one employs band caluclations to take into account the carrier hops between the CuO_2 and reservoir layers, not only do technical difficulties arise on account of the large unit cell but there are also questions raised by the fact that the coherence length in the direction of the c axis, perpendicular to the layers, is less than the size of the unit cell in this direction. A more serious objection to such an approach is that electron–electron correlations, leading to antiferromagnetic ordering, play the main role in the CuO_2 layers. In the envelope method these correlated states can be chosen instead of Bloch band states (as is done below). As a first approximation to the envelope method, we call attention to Ref. 2, where hybridization of the dispersion relations obtained for isolated layers is taken into account in the tunneling-Hamiltonian method.

In what follows, the dispersion relation for systems with two and three CuO_2 layers per unit cell is chosen to be the same as for systems with one CuO_2 layer. This is justified, first, by the fact that the hopping integral between CuO_2 layers separated by a layer of Y or Ca atoms, for example, is itself less than the hopping integrals between the nearest neighbors in a CuO_2 layer; second, taking account of the electron–electron correlations in a CuO_2 layer results in sharp suppression of the hopping integral between neighboring layers, and the spectrum of renormalized quasiparticles of a multiple CuO_2-layer structure reduces to the analogous spectrum of Bloch carriers for an isolated layer.[3]

A distinguishing feature of the crystal structure of cuprate HTSCs is that the hopping integrals between the nearest neighbors in the CuO_2 layers occur along the edges of a square, while in the reservoir layers they occur along the diagonals. For this reason, the constant-energy contours near the corresponding half-fillings are squares turned relative to one another by 45 degrees. The dispersion relations in the CuO_2 layer (ε_w) and in a reservoir layer (ε_b) can be represented in the nearest-neighbor approximation as

$$\varepsilon_w(k) = \frac{\Delta_w}{4}[2 - \cos(k_x a) - \cos(k_y a)],$$

$$\varepsilon_b(k) = U_0 + \frac{\Delta_b}{2}[1 - \cos(k_x a)\cos(k_y a)],$$

where $k = (k_x, k_y)$ is the wave vector in the plane of the layers, $\Delta_{w,b}$ are the widths of the bands in a CuO_2 layer (well) and in a reservoir layer (barrier), respectively, and U_0 is the barrier height at $k = 0$. There is thus a large difference in the anisotropic effective masses for the CuO_2 and reservoir layers. For this reason, for a small difference U_0 in the
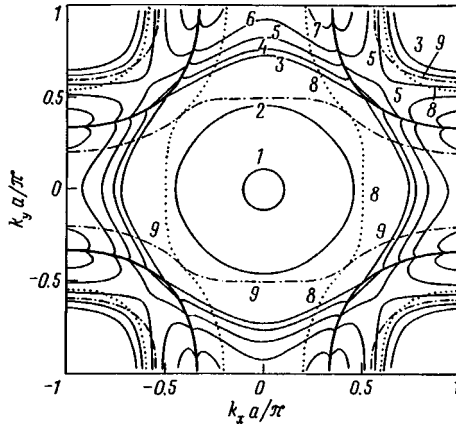
FIG. 1. Constant-energy contours (1–7) and contours of a change in sign of the effective mass (m_x — 8, m_y — 9) for the incoherent case neglecting electron–electron correlations for $h_w = h_b = 5.8$ Å, $U_0 = 0.5$ eV, $\Delta_w = 2$ eV, $\Delta_b = 1$ eV; curves 1–7 are for $E/\Delta_w = 0.10$, 0.30, 0.50, 0.52, 0.55, 0.58, and 0.62.

positions of the corresponding bands at $k = 0$ (which is treated below as an adjustable parameter whose magnitude depends strongly not only on the difference of the atomic levels of the layers but also on the difference of the electron–electron correlations in these layers), the potential energy, which is proportional to the difference in the kinetic energies along the layers, can change sign along a constant-energy contour. As a result, near half-filling some states at the Fermi surface will correspond to states predominantly localized in a CuO_2 layer, while some states will be localized in the reservoir region (transformation of states). This qualitative result does not depend on the method used to describe such states. The difference in the anisotropy of the effective masses of different layers also remains when the hops to non-nearest neighbors are taken into account. For semiconductor heterostructures this result was obtained in Ref. 4. Since for cuprate HTSCs the possibility of both coherent and incoherent motion along the c axis is being discussed,[5] we shall examine both cases separately.

For the incoherent case, when electron–electron correlations are neglected (as is valid for overdoped systems), for finding the constant-energy contours it is sufficient to solve the problem of the spatial quantization levels in an individual well of width h. On account of the difference of the anisotropies of ε_w and ε_b, the reservoir layer starts to play the role of a well at certain values of k. The thick lines in Fig. 1 show the contours of such a transformation: At the corners of the Brillouin zone, which are bounded by these contours, the states belong to the reservoir layer and away from the corners they belong to the CuO_2 layer. Curves 1–7 are constant-energy lines. As one can see from the figure, in the region near half-filling ($E \approx 0.5\Delta_w$), part of the constant-energy contour corresponds to states localized in the CuO_2 layer and part corresponds to states localized in the reservoir. The form of the contours is virtually independent of U_0, Δ_w, and Δ_b, i.e., the conclusions drawn are of a quite general character. The dotted lines in Fig. 1 represent the contours of a change in the sign of the effective-mass components m_x and m_y (lines 8 and 9, respectively): $1/m_{x,y} = \hbar^{-2} \partial^2 E / \partial k_{x,y}^2$. Thus, the effective-mass components can have different signs on different sections of a constant-energy contour. For
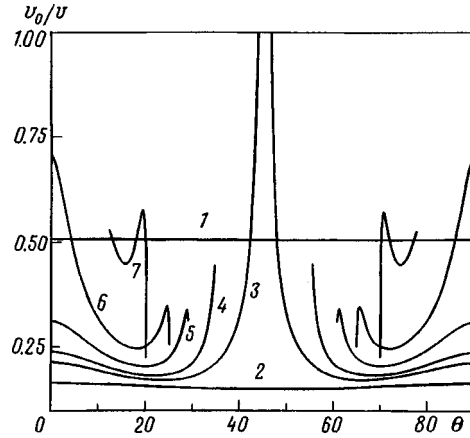
FIG. 2. Angular dependence of the density of states. The parameters are the same as in Fig. 1, $v_0 = \sqrt{U_0/2\pi^2 m_{zw}}$.

this reason, hole pairs (bihole) in the case of hole doping or electron pairs (bielectron) in the case of electron doping can form as a result of the Coulomb interaction. For this, the effective mass of a pair consisting of states with different signs of the masses should be negative. The observed inverse hydrogenlike series in the optical spectra of BiI_3 (Ref. 6) can be interpreted as a manifestation of such pairs formed from particles with different energies. In our case, however, the pairs are formed from states on the Fermi surface and can belong to different layers. There exists a quite wide interval of values of the parameters of the system where as the temperature decreases, Bose condensation of such pairs occurs, leading to superconductivity.

The angular dependences of the quantity $1/v(k) = \hbar/|\nabla_k E|$, proportional to the density of states, are shown in Fig. 2. As one can see from the figure, together with the characteristic feature at $\theta = 0$ and $90°$ of the CuO_2 layers at half-filling (van Hove singularities), there appear additional maxima near the points of a transformation of the states. Such features lead to the formation of two maxima in the curve of the total density of states versus the energy.

If the coherence length along the c axis is much longer than the period of the structure, then minibands which characterize the motion along the c axis arise as a function of the wave vector k_z. In this case, it is natural to choose as the criterion for finding carriers predominantly in a CuO_2 layer or in the reservoir, the ratio of the probabilities in the well and barrier: $\eta = W_w/W_b$. The calculations show that the qualitative form of the constant-energy contours in this case is the same as in the incoherent case.

Figure 3 shows the contour $E = 0.52\Delta_w$ for $k_z = 0$ (the solid lines correspond to $\eta > 1$, the dashed lines correspond to $\eta < 1$). The curves 3 and 4 are constant-energy contours of the higher size-quantization subbands. We note that similar contours (not shown in Fig. 1), corresponding to resonances in the continuous spectrum, are present in the incoherent case considered above. On account of this, the electronic states on them have much shorter lifetimes than localized states.

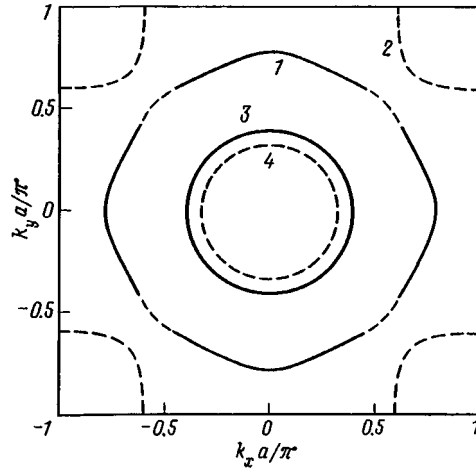The picture remains qualitatively the same if antiferromagnetic ordering in the CuO_2

FIG. 3. Constant-energy contours of a superlattice for $E=0.52\Delta_w$ for $k_z=0$, curves *1,2* — first subband, *3,4* — second and third size-quantization subbands. The parameters of the structure are the same as in Fig. 1.

layers, which occurs with underdoping, is switched on. In this case the wave functions and the dispersion relation of the correlated state in a CuO_2 layer can be written in the form

$$\psi = u\,\psi_k + v\,\psi_{k+Q},$$

$$\varepsilon = \frac{1}{2}\left\{\varepsilon_w(k) + \varepsilon_w(k+Q) \pm \sqrt{[\varepsilon_w(k) - \varepsilon_w(k+Q)]^2 + 4\delta}\right\},$$

where δ is the dielectric gap and Q is the nesting vector. Figure 4 shows a family of
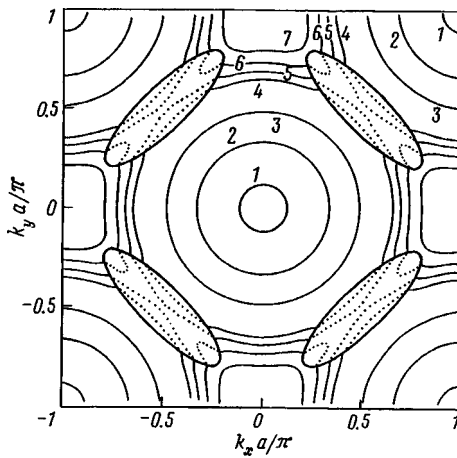
FIG. 4. Constant-energy contours taking account of the dielectric gap for $\delta=0.1$ eV, $\Delta_b=0.5$ eV, $Q = \pi/a(1.1)$; curves *1–7* are for $E/\Delta_w=0.10$, 0.20, 0.30, 0.40, 0.42, 0.44, and 0.46; all other parameters are the same as in Fig. 1.

constant-energy contours for the incoherent case and the bottom subband (minus sign in ε). Just as in the absence of antiferromagnetic ordering, in a certain energy range a transformation of the states on the constant-energy contour occurs (the solid lines correspond to localization in a CuO_2 layer, and the dotted lines correspond to localization in the reservoir layer).

In the case of optimal doping, the long-range antiferromagnetic order is absent, but short-range order remains considerable, and the behavior of carriers on the Fermi surface is qualitatively identical to the case of light doping (Fig. 4).

The above-described character of hole states, where on a part of the Fermi surface carriers belong to one layer, while on the remaining part of the Fermi surface carriers belong to a different layer, makes it possible to understand a number of characteristic features of HTSCs. Specifically, to explain the characteristic features of the frequency and temperature dependences of the conductivity and Hall effect, two substantially different relaxation times are introduced phenomenologically on different sections of the Fermi surface.[7] If these sections of the Fermi surface belong to different layers, the difference in the scattering intensities is natural.

Angle-resolved photoemission experiments in the normal and superconducting phases show that the angular dependence of the d-type superconducting gap is identical to that of the density of states in the normal phase. This is explained by the fact that the electron–electron interaction becomes weaker as the scattering angle increases — forward scattering predominates. Then the value of the gap at some point on the Fermi surface will be determined only by states in some interval of angles near a given state (momentum decoupling).[8] In our opinion, this interval of angles is determined by the region of the Fermi surface, belonging to a definite layer, since leaving this interval corresponds to scattering from one layer into another, and scattering is small to the extent that the overlap integrals of the wave functions between the CuO_2 and reservoir states is small.

The same effect explains the experimentally observed order-of-magnitude weaker suppression of d-type pairing by scattering by nonmagnetic impurities than expected theoretically. If the zeros of d-type superconducting gap lie on the part of the Fermi surface corresponding to the reservoir layer, then scattering from regions belonging to CuO_2 layers and having a large gap into the region of the zeros of the gap, which results in depairing, will be strongly suppressed.

[a]e-mail: kopaev@sci.lebedev.ru

[1] I. Bozovic and J. N. Eckstein, in *Physical Properties of High Temperature Superconductor,* Vol. V, edited by D. M. Ginsberg, World Scientific, Singapore 1996.
[2] R. Combescot, Phys. Rev. B **57**, 8632 (1998).
[3] M. Sugihara, M. A. Ikeda, and P. Entel, Phys. Rev. B **57**, 11760 (1998).
[4] V. V. Kapaev and Yu. V. Kopaev, JETP Lett. **65**, 202 (1997).
[5] A. A. Abrikosov, Phys. Rev. B **57**, 7488 (1998).

[6] E. F. Gross, I. N. Ural'tsev, and R. I. Shekhmamet'ev, JETP Lett. **13**, 357 (1971).
[7] A. Zheleznyak, V. Yakovenko, H. Drew, and I. Mazin, Phys. Rev. B **57**, 3089 (1998).
[8] G. Varelogiannis, Phys. Rev. B **57**, R732 (1998).

Translated by M. E. Alferieff

Tunneling investigations of single crystals of the single-layer cuprate $Bi_2Sr_2CuO_z$ in high magnetic fields

S. I. Vedeneev

P. N. Lebedev Physics Institute, Russian Academy of Sciences, 117924 Moscow, Russia

The coexistence of a superconducting gap and a normal-state gap (pseudogap) is observed in tunneling experiments with high-quality single crystals of the single-layer cuprate $Bi_2Sr_2CuO_z$. At temperatures $T < T_c$ the normal-state gap, whose width is close to that of the superconducting gap, does not vanish in magnetic fields $H > H_{c2}$. The large smearing of the gap structure in the tunneling spectra and the high conductance of tunnel junctions at zero bias voltage are due to the strong angular dependence of the superconducting- and normal-state gaps. The results of the investigations are in good agreement with recently published angle-resolved photoemission data. © *1998 American Institute of Physics.* [S0021-3640(98)01115-3]

PACS numbers: 74.76.Bz, 74.72.Hs, 74.25.Fy

The successful use of tunneling spectroscopy for studying the superconducting state of ordinary superconductors is now familiar. However, in application to high-T_c superconductors (HTSCs) this method has encountered great difficulties due to the extremely short coherence length ξ and high nonuniformity of the experimental samples. To date, well-reproducible results have been obtained only for the layered cuprate $Bi_2Sr_2CaCu_2O_{8+\delta}$ (Bi2212). Earlier, we performed tunneling investigations of Bi2212 single crystals by the break-junction method.[1] The experiments showed that good-quality tunnel junctions (TJs) — junctions with very low leakage currents and well-resolved gap structure — in the *ab* plane can be prepared from Bi2212 crystals. Photoemission experiments with high angular resolution (APRES)[2–4] confirmed the magnitude of the energy gap found by the tunneling method,[1] but at the same time they revealed a strong angular dependence of the gap which corresponds to $d_{x^2-y^2}$ symmetry of the order parameter. Moreover, a pseudogap (gap in the quasiparticle spectrum) was observed in photoemission experiments on underdoped Bi2212 at temperatures T above the superconducting transition temperature T_c. This gap is attributed to the formation of superconducting pairs without phase coherence.

The single-layer cuprate $Bi_2Sr_2CuO_z$ (Bi2201) with a low value of T_c is a very promising material for studying the superconducting and normal properties of HTSCs at low temperatures. But the situation with its tunneling investigations turned out to be more complicated. The first measurements of the energy gap in Bi2201 in experiments with point tunnel contacts based on imperfect Bi2201 crystals were performed a long time
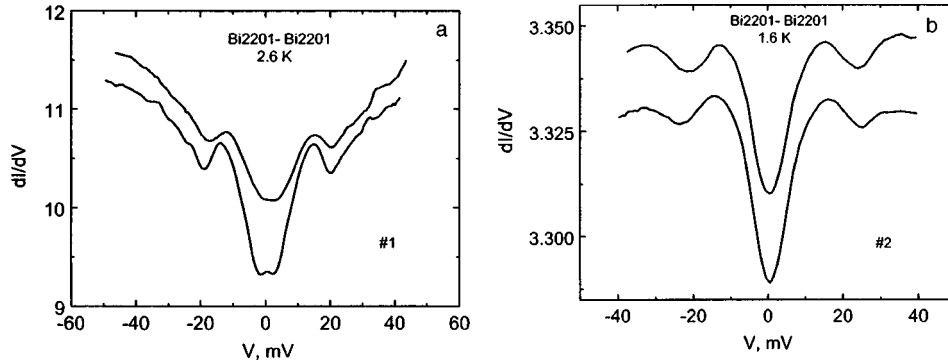
FIG. 1. Differential conductances $dI/dV(V)$ of four tunnel junctions at temperatures 2.6 and 1.6 K. The junctions were prepared from two single crystals (Nos. 1 and 2). For clarity, in both cases the upper curves are shifted relative to the bottom curves .

ago,[5] but despite numerous attempts it has proved impossible so far to produce tunnel junctions of satisfactory quality, even using the break-junction method. Since ξ_{ab} in Bi2201 is larger than in Bi2212 and reaches 40 Å, on account of the proximity effect it is very difficult to prepare a good tunneling barrier in liquid helium. Two strongly anisotropic superconducting energy gaps of width 10 ± 2 and 7 ± 3 MeV, respectively, have been observed recently in APRES experiments[6] in optimally doped and underdoped $Bi_2Sr_{2-x}La_xCuO_{6+\delta}$. The authors of Ref. 6 also discovered a pseudogap above T_c and proposed that the pseudogap and the superconducting gap have a pair interaction of the same nature. In the present letter we report tunneling investigations of high-quality Bi2201 single crystals in magnetic fields up to 23 T. The results confirm the existence of superconducting and normal gaps.

$Bi_{(2+x)}Sr_{2-(x+y)}Cu_{(1+y)}O_z$ single crystals with Bi/Sr = 1.4–1.5 (the excess Bi occupied Sr positions) were grown in closed cavities in a KCl fluxed melt.[7] On account of the prolonged growth process, the crystals had a high degree of cationic ordering. The dimensions of the crystals were (0.7–1.5) mm $\times$ (0.4–0.7) mm $\times$ (1.5–5) μm. The half-width of the main reflections of the rocking curves in the x-ray investigations of the crystals did not exceed 0.3–0.1°. The lattice parameters were equal to $a = 5.360$ Å and $c = 24.615$ Å and the superlattice period was equal to $\tilde{a} = 4.75a$. The superconducting transition widths ΔT_c between the points of 10% and 90% resistance were equal to 0.5–1 K. The values obtained for ΔT_c and T_c in dc resistance measurements and in magnetic susceptibility measurements were virtually identical. The temperature dependence of the resistance of the crystals in the ab plane was linear with slope $\Delta\rho_{ab}/\Delta T = 0.5-1.5$ $\mu\Omega \cdot$ cm/K at high temperatures and below 20–40 K it saturated to the residual resistance. The residual resistivity $\rho_{ab}(0)$ lay between 80 and 180 $\mu\Omega\cdot$cm. Break-junction type TJs were prepared directly in liquid helium by the method described earlier.[1] The current–voltage ($I-V$) characteristics and their derivatives dV/dI were measured by the standard phase sensitive modulation method. On the basis of a special check,[1] it can be assumed that in TJs with this geometry the tunneling current in the ab plane was measured.

The typical differential conductances $dI/dV(V)$ of the four TJs, fabricated from two single crystals (Nos. 1 and 2), at temperatures 2.6 K and 1.6 K are shown in Fig. 1. For

clarity, in both cases the upper curves are shifted relative to the lower curves. Although the TJs had low (a) and high (b) resistance, they showed very high conductance at zero bias voltage, the gap structure in the tunneling spectra was strongly ''smeared,'' and the conductance itself $dI/dV(V)$ in the case of the low-resistance TJs (a) had a V shape. Nothing like this was observed in our tunneling experiments with Bi2212 single crystals.[1] In a recent work,[8] having analyzed different current-leakage channels in TJ-based HTSCs and their influence on the spectra obtained, the authors proposed a procedure for extracting the real tunneling density of states. However, in this case the conductance of the TJ at $V = 0$ mV is too high (it equals 80–90% of the conductance at large values of V) to be explained by leakage currents. Despite many attempts, the same tunneling spectra with gap structure and low conductance at $V = 0$ mV as in the case of Bi2212 single crystals could not be obtained.[1] Taking this into consideration, it is likely that the anomalies observed in the tunneling spectra in Fig. 1 are due to a strong anisotropy of the superconducting gap recently found in Bi2201 in APRES experiments.[6] In underdoped $Bi_2Sr_{2-x}La_xCuO_{6+\delta}$ crystals the authors observed a smeared, but reproducible, 7 ± 3 meV superconducting gap along the $(\pi,0)$ symmetric line in $\mathbf{k}$ space and a zero gap $45°$ away from this line. For the SIS TJs studied here the distance between the two main maxima on the $dI/dV(V)$ curves equals $4\Delta_{p-p}$ and, as one can see in Fig. 1, the superconducting gap $2\Delta_{p-p}$ lies in the region 13.5–15 meV and $\Delta_{p-p} \approx 6.5 - 7$ meV. In TJs of this geometry, the spectra obtained reflect the tunneling density of states, integrated over the polar angle in $\mathbf{k}_{ab}$ space.[9] The strong angular dependence of the energy gap with zero values in certain directions should result in a high density of states inside the gap (and therefore in a high conductance of the TJs at zero bias voltage) and strong smearing of the gap structure with the maximum value of Δ_{p-p}. This agrees completely with the APRES data.[6] Both our and the APRES spectra have a smeared gap structure, which is difficult to describe by a simple BCS model. To determine the value of Δ we employed the phenomenological parameter Γ that takes account of pair breaking[10] and obtained $\Delta = 3.5 - 4$ meV. This is very close to the value of Δ which we found in earlier experiments with Bi2201-based point TJs.[5]

To determine the relation between Δ and T_c, we measured the conductance $dI/dV(V)$ of TJs at different temperatures. The results are shown in Fig. 2. For clarity, the curves are shifted relative to the upper curve. One can see that as temperature increases, the gap-associated features (marked by arrows) become broadened even more strongly and vanish. Since T_c for this sample was equal to 3.5 K, and the gap features vanished at a temperature close to T_c, it is natural to infer that the observed gap structure is related with the superconducting gap in Bi2201. It is also seen in Fig. 2 that $4\Delta_{p-p}$ decreased somewhat as temperature increased, but because of the smeared nature of the structure we could not determine the temperature dependence of Δ.

It is well known[1] that tunneling spectra obtained for ordinary superconductors when studying high-resistance TJs with good tunneling barriers should be flat with bias voltages exceeding Δ/e, as follows from the Fermi liquid model. The ''V'' shape of the conductance $dI/dV(V)$ of low-resistance TJs is due to the decrease in the height of the tunneling barrier under the action of an increasing bias voltage. However, as follows from Fig. 2, as temperature increases, the curve $dI/dV(V)$ changes from flat to V-shaped as $dI/dV(V)$ increases. Once again this could be due to a decrease in the height of the tunneling barrier in the TJ or an increase in ξ in Bi2201 as a result of an increase in the
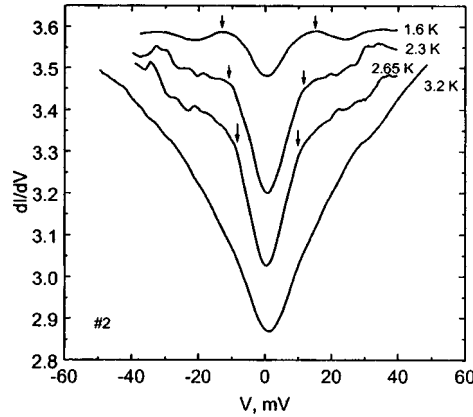
FIG. 2. Tunneling conductance $dI/dV(V)$ of a junction at different temperatures for sample No. 2. The curves are shifted relative to the top curve. The gap structure is marked by arrows.

temperature. To rule out this possibility, we measured the tunneling spectra of our break-junction TJs in constant magnetic fields above the upper critical field H_{c2} in Bi2201 at the given temperature. The experiments were performed in the geometry $\mathbf{B}\|\mathbf{c}, \mathbf{J}\|\mathbf{ab}$.

The effect of a magnetic field on the conductance $dI/dV(V)$ at 1.4 K is shown in Fig. 3a. The behavior of the break-junction TJs based on Bi2201 and Bi2212[1] differs sharply. In the first place, as the magnetic field increased, the conductance $dI/dV(V)$ decreased and the curves $dI/dV(V)$ shifted in the direction of high tunneling with a decrease of the conductance at $V = 0$ mV. In the second place, the gap feature associated with the superconducting state practically vanished even in a 5 T field, while according to the results of magnetotransport measurements, which we performed on this crystal, at 1.4 K $H_{c2} = 14$ T. In the case of Bi2212 in magnetic fields, we observed only a weak smearing of the tunneling spectra with no change in shape, as expected for $H < H_{c2}$. In tunneling experiments, a region $\sim \xi$ near the tunneling barrier is investigated. For break-junction TJs in a mixed state the conductance $dI/dV(V)$ reflects the total tunneling density of states of vortices with a normal core and a density of states of the superconductor near the vortices which is broadened by the local magnetic field. Therefore the gap structure can be smeared even when $H \ll H_{c2}$. It can be expected that at constant temperature the transmittance of the tunneling barrier does not change and the general form of the tunneling conductance should remain unchanged. Figure 3b shows the differential resistance $dV/dI(V)$ at two extreme points $V = 0$ mV and $V = 40$ mV, determined from Fig. 3a, as a function of the squared magnetic field. The dependences are quadratic in the field with no saturation in a large range of fields, just as for the magnetoresistance of compensated metals in the transverse geometry ($\mathbf{B}\|\mathbf{c}, \mathbf{J}\|\mathbf{ab}$). This can serve as an indication that the normal electrons make a determining contribution to the tunneling spectra obtained.

In tunneling investigations of ordinary superconductors in magnetic fields $H > H_{c2}$ the differential conductance $dI/dV(V)$ near the gap is constant. In this case the curves $dI/dV(V)$ in Fig. 3a retained their shape with a strongly smeared gap feature even in the normal state of the TJ in fields $H > H_{c2}$. In addition, the position of this feature on the
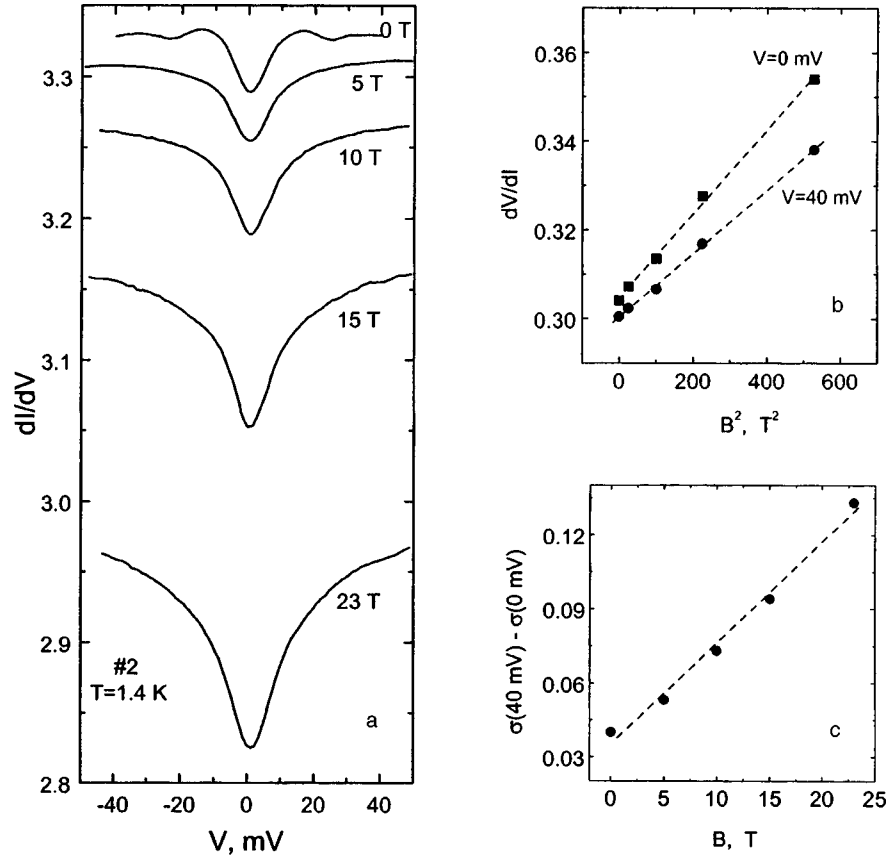
FIG. 3. (a) Effect of a magnetic field on the tunneling conductance $dI/dV(V)$ at 1.4 K. (b) Dependence on the squared magnetic field of the differential conductance $dV/dI(V)$ of a tunnel junction at two extreme points $V=0$ mV and $V=40$ mV, determined from Fig. 3a. (c) Difference of the differential conductances $dI/dV(V)$ at two extreme points $V=40$ mV and $V=0$ mV, determined from Fig. 3a, as a function of the magnetic field.

voltage axis was close to $4\Delta_{p-p}$. Once again this agrees well with the APRES data.[6] Although for $H>H_{c2}$ we cannot determine from Fig. 3 the magnitude of the gap accurately, we can say that the normal-state gap remains right up to 23 T — the maximum field in our experiments. Figure 3c shows the difference of the values of the differential conductance $dI/dV(V)$ at two extreme points $V=40$ mV and $V=0$ mV, determined from Fig. 3a as a function of the magnetic field. One can see that the magnitude of the zero ''dip'' in the curves $dI/dV(V)$ increases linearly with the magnetic field. The effect of a magnetic field on the gap structure of the superconducting and normal states can be clearly seen in Fig. 4, where the second derivatives $d^2I/dV^2(V)$ of the tunneling current in different magnetic fields are displayed. For $H=0$ T the zeros of $d^2I/dV^2(V)$ at $|eV| =2\Delta_{p-p}$ (marked by arrows) correspond to the superconducting gap. As the magnetic field increases, the superconducting gap vanishes and the normal-state gap remains. But the gap structure in the curves $d^2I/dV^2(V)$ is not washed out in a field, as happened for Bi2212,[1] but rather it becomes sharper. The normal-state gap could be due to the anti-
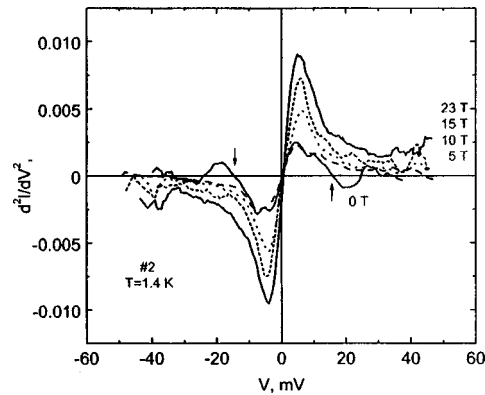
FIG. 4. Effect of a magnetic field on the gap structures of superconducting and normal states in the second derivatives $d^2I/dV^2(V)$ of the tunneling current in different magnetic fields.

ferromagnetic interaction, which could be important in underdoped HTSC materials. The decrease of this interaction with increasing magnetic field results in sharpening of the gap structure.[11] But it is more likely that the normal-state gap is a pseudogap. This is being widely discussed in the literature. Since in our Bi2201 crystals the paramagnetic limit equals 24 T even for $\Delta_0 = 3.5$ meV, the pseudogap could be related with superconducting pairs without phase coherence, which could exist both above T_c (Fig. 2) and above H_{c2} at $T < T_c$ (Fig. 3). Then the smearing of the gap structure and the high conductance of TJs with $V = 0$ mV are due to the strong angular dependence and to the normal-state gap.[6] Impurity scattering, which plays an important role in the smearing of the normal-state gap, decreases in a magnetic field, sharpening the tunneling spectra.

[1] S. I. Vedeneev, K. A. Kuznetsov, V. A. Stepanov, and A. A. Tsvetkov, JETP Lett. **57**, 352 (1993); S. I. Vedeneev, A. G. M. Jansen, P. Samuely *et al.*, Phys. Rev. B **49**, 9823 (1994).

[2] J. M. Harris, Z.-X. Shen, P. J. White *et al.*, Phys. Rev. B **54**, 15665 (1996).

[3] D. S. Marshall, D. S. Dessan, A. G. Loeser *et al.*, Phys. Rev. Lett. **76**, 4841 (1996).

[4] H. Ding, T. Yokoya, J. C. Campuzano *et al.*, Nature (London) **382**, 51 (1996).

[5] S. I. Vedeneev, P. Samuely, A. G. M. Jansen *et al.*, Z. Phys. B – Cond. Matt. **83**, 343 (1991).

[6] J. M. Harris, P. J. White, Z.-X. Shen *et al.*, Phys. Rev. Lett. **79**, 143 (1997).

[7] J. I. Gorina, G. A. Kaljujnaia, V. I. Ktitorov *et al.*, Solid State Commun. **91**, 615 (1994); V. P. Martovitsky, J. I. Gorina, and G. A. Kaljujnaia, Solid State Commun. **96**, 893 (1995).

[8] P. Mallet, D. Roditchev, W. Sacks *et al.*, Phys. Rev. B **54**, 13324 (1996).

[9] K. Kitazawa, Science **271**, 313 (1996).

[10] R. C. Dynes, V. Narayanamurti, and J. P. Garno, Phys. Rev. Lett. **41**, 1509 (1978).

[11] P. J. White, Z.-X. Shen, C. Kim *et al.*, Phys. Rev. B **54**, 15669 (1996).

Translated by M. E. Alferieff

Free and localized positively charged excitons in the emission spectrum of GaAs/AlGaAs quantum wells

O. V. Volkov[a] and I. V. Kukushkin

Institute of Solid-State Physics, Russian Academy of Sciences, 142432 Chernogolovka, Moscow Region, Russia

K. von Klitzing and K. Eberl

Max-Planck-Institut für Festkörperforschung, 70569 Stuttgart, Germany

The recombination emission spectra of an excitonic complex (A^0X) localized on a neutral acceptor, which have previously been attributed to a positively charged exciton (X^+), are investigated. Satellites arising around the main luminescence line as a result of recoil processes during recombination of the complex which leave the surviving hole in an excited state are observed and investigated. It is shown in a computational model based on the Luttinger Hamiltonian that the energy splittings between the main line and the satellites correspond to an in-barrier impurity center located a definite distance from the well. It is shown that as the magnetic field increases, a transition is observed from the singlet ground state of the complex to a multiplet state. © *1998 American Institute of Physics.* [S0021-3640(98)01215-8]

PACS numbers: 78.55.Cr, 78.66.Fd, 71.35.Ji

1. Despite the fact that GaAs/AlGaAs — single quantum wells (SQWs) — have been studied quite well experimentally, a number of photoluminescence lines which are observed in these structures are still a subject of debate. This is due both to the complexity of quantum systems consisting of more than two particles and to the lack of detailed information about the structure itself, specifically, about the impurities present in it and their spatial distribution. Some of the most interesting objects active in photoluminescence are positively and negatively charged excitonic complexes (trions) X^+ and X^-, arising in quantum wells when the density of the main carriers is low.[1,2] As was shown in Refs. 3 and 4, these formations are not free, but rather they are localized in the Coulomb potential of charged impurities present in the barrier and form A_b^0X and D_b^0X complexes. However, the question of the specific arrangement of these impurities has remained open.

A distinguishing feature of quantum electron–hole systems consisting of more than two particles is the possibility of recombination, as a result of which the remaining particle can be found in not only the ground but also an excited state. Here, replicas of the main luminescence line which are shifted to lower energies by the amount of the splitting between the ground and excited states of the system after the recombination event in the emission spectrum. In the case of a D^0X complex in GaAs such replicas (dielectronic

satellites) were studied in detail in Ref. 5. Size quantization and the possibility of spatial separation of impurity centers (in a barrier) and charge carriers (in a well) modify the energy spectrum of neutral impurities in SQWs. As a result, for a $D_b^0 X$ complex (exciton bound on a neutral donor in the barrier) the satellites associated with transitions to an excited state D_b^0 have a virtually linear cyclotron shift relative to the main line. This experimental fact was used to prove the two-particle nature of the recombination line corresponding to a $D_b^0 X$ complex.[6] Satellites of a recombination line of an excitonic complex have not been previously observed in a hole system, and the relation of such a line to positively charged excitons X^+ was established by analogy with the electronic system.[2] We have observed and investigated such satellites in a series of quantum wells ranging in width from 150 to 300 Å. Analysis of the energy splitting between the main recombination line of an excitonic complex and its satellites made it possible to determine the characteristic arrangement of the acceptors on which localization of positively charged excitons with the formation of an $A_b^0 X$ complex occurs. A transition from the singlet ground state of an excitonic complex to a multiplet state was observed as the magnetic field increased. This transition is manifested as a change in the intensities of the components of the emission spectrum.

2. We investigated undoped GaAs quantum wells 150, 200, 250, and 300 Å wide, with $Al_{0.3}Ga_{0.7}As$ barriers. The structures were grown an undoped GaAs substrate by molecular-beam epitaxy (MBE). The sample with the 150 Å wide well contained a series of quantum wells separated by a superlattice with AlGaAs/GaAs layer thicknesses of 50 Å/30 Å. All other samples contained a single quantum well. In the samples with the 200 and 250 Å wells, the well was grown on a superlattice with layer thicknesses of 100 Å/30 Å; in the sample with the 300 Å well the AlGaAs layer located closest to the well on the superlattice side was 500 Å thick. The characteristic width of the luminescence lines in the experimental structures was equal to 0.1–0.2 meV in a magnetic field ~ 10 T, indicating that the structures were of high quality. Optical excitation of the system was performed with a Ti/Sp laser with photon energy 1.65 eV or He/Ne laser with photon energy 1.96 eV. Despite the fact that we investigated undoped quantum wells, all structures contained a low-density two-dimensional channel (with charge carrier density 10^9–10^{10} cm^{-2}), where the sign of the charge carriers could be changed by varying the photoexcitation energy.[4] In the present work we investigated mainly quantum wells with a low-density p-channel. The spectral instrumentation consisted of a Ramanor U-1000 double monochromator, which combined with a semiconductor detector with charge coupling (CCD) gave a resolution of 0.03 meV. The measurements were performed at a temperature of 1.5 K in the range of magnetic fields 0–11 T.

3. Figure 1a shows the photoluminescence spectrum measured for a 200 Å SQW in a zero magnetic field. The spectrum consists of two spectral lines — a free exciton line (X) and the line of an excitonic complex, which in the case of a two-dimensional (2D) low-density hole channel consists of an exciton localized on a neutral acceptor in the barrier ($A_b^0 X$).[4] The presence of two equivalent holes in an $A_b^0 X$ complex (just as in X^+) allows recombination of the complex with a transition of the remaining hole to an excited state. In the process, satellites of the main recombination line, which reflect the spectrum of the excited states of an A_b^0 center (or a free hole in the case X^+), should appear in the emission spectrum. We actually observed such satellites in the emission spectra of all experimental samples in a perpendicular magnetic field.
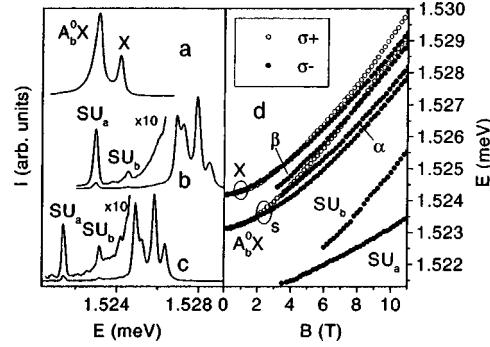
FIG. 1. (a) Photoluminescence spectra, measured in a 200 Å SQW in a zero magnetic field. (b, c) Photoluminescence spectra measured in 200 Å(b) and 250 Å (c) SQWs in a 9.5 T magnetic field in σ polarization. (d) Energy of optical transitions versus the magnetic field, measured for a 200 Å SQW in two circular polarizations.

The luminescence spectra, measured for 200 Å and 250 Å SQWs in σ polarization in a 9.5 T magnetic field are displayed in Figs. 1b and 1c. Two lines, designated as SU_a and SU_b, are clearly seen in the spectra. The experiments performed on samples where the carrier type in the well could be changed by photoexcitation[4] showed that the SU_a and SU_b lines are associated exclusively with the p-channel and vanish completely from the spectra in the case of inversion of carrier type. Figure 1d shows the magnetic field dependences of the optical transition energies measured in two circular polarizations for a 200 Å SQW. It should be noted that the spectral properties, which we measured, of the $A_b^0 X$ line are identical to the results which were obtained earlier for similar structures by other authors[2,7] and which were attributed to radiation of a free trion (X^+). However, the satellite line which we observed makes it possible to rule out unequivocally such an interpretation, since the observed splittings between the main line and the replicas $SU_{a,b}$ do not tend to zero in a zero magnetic field, which is characteristic of excited states A_b^0 and not of a free hole. Since the spectral position of the replicas $SU_{a,b}$ in SQWs of different width is related to the emission lines of the SQWs (see Fig. 3a below) and in sufficiently narrow wells the radiation energy exceeds the band gap in GaAs, it must be concluded that the $SU_{a,b}$ lines are associated with recombination processes in SQWs. As one can see from Fig. 3a, the characteristic cyclotron mass corresponding to the SU_a line ($\sim 0.4 m_e$) is much greater (by a factor of 5) than the electron mass, indicating a hole Auger process. Therefore it must be inferred that the $SU_{a,b}$ line arises as a result of the recombination of a $A_b^0 X$ complex, for which the remaining hole is in an excited state of the impurity center. The magnitude of the splitting in the zero magnetic field limit serves as a measure of localization of the complex and makes it possible to determine the specific arrangement of the impurity center. To solve this problem, we developed a computational method which is based on a 4×4 Luttinger Hamiltonian[8] and takes account of both the real geometry of the well and the finite height of the potential barriers. The matrix elements of the Hamiltonian were calculated in a cylindrical gauge similarly to Ref. 9, but in contrast to this and other calculations we expressed the three-dimensional basis functions as a product of solutions, which are known in a numerical form and were obtained by the relaxation method, of one-dimensional differential equations.[10] The calculations gave an accuracy of not less than 0.1 meV. As the band parameters of the
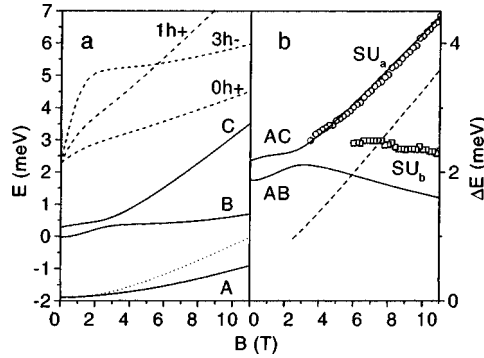
FIG. 2. (a) Magnetic field dependence, calculated for a 200 Å SQW with the distance to the acceptor equal to 100 Å, of the energies of the three lowest states of an A_b^0 center with total angular momentum $J_z = +3/2$ (solid lines). The dotted line shows the energy of the ground state with $J_z = -3/2$. The dashed lines show the energy of the corresponding quantum states of a free hole. (b) Magnetic field dependence of the splitting between the lines of $A_b^0 X$ and $SU_a (\bigcirc)$, $SU_b (\square)$ in σ polarization, as measured for a 200 ÅSQW. The solid lines show the computational results for an A_b^0 center (a); the dashed line shows the computational results for the splitting between the $1h+$ and $0h+$ levels of a free hole.

materials, we employed one of the generally accepted sets employed in Ref. 9.

The calculations showed that the presence of an acceptor on the boundary of a SQW does not correspond to the experimentally observed splittings, since it gives a much larger splitting between the ground and first excited states of an A_b^0 center in the case $B = 0$. At the same time, we obtain good agreement with experiment by setting the distance L between the SQW boundary and the acceptor equal to the distance to the nearest AlGaAs/GaAs interface near the superlattice adjoining the quantum well. This assumption is fully justified, since the breaking of chemical bonds at the boundary of two materials in itself creates charged centers, and moreover the local stress fields produce conditions for diffusion of impurities out of the interior. Figure 2a displays the computational results for the three lowest energy levels A_b^0 with the total angular momentum projection $J_z = M_z + S_z = +3/2$ (the ground state of a center belongs to this group), which were obtained for a 200 Å SQW and $L = 100$ Å. The same figure shows (dashed lines) free-hole energy levels into which the levels A, B, and C pass in the limit $L \to \infty$. As one can see from Fig. 2b, the energy ΔE of splitting off of the replica SU_a from the main line of $A_b^0 X$ matches well the difference of the energies of the levels A and C. The spectral shift of the replica SU_b and the splitting between the levels A and B agree somewhat more poorly, but the magnitude of this splitting was found to depend strongly on the specific choice of the Luttinger parameters, which are not known with adequate accuracy. At the same time, the free-hole splitting ΔE $(L \to \infty)$ shown in Fig. 2b (dashed line) differs radically from the dependence observed in our experiment. The measured and computed magnetic-field dependences, obtained for wells of different width, of the splitting off energy of the replica SU_a are compared in Fig. 3a and show good agreement.

The model presented above touches upon a number of interesting questions, which have not been completely investigated. It is obvious that if acceptors are concentrated on an AlGaAs/GaAs interface far from the SQW, then they should also exist on the boundary of the well itself. There arises the question: Why is the exciton complex localized
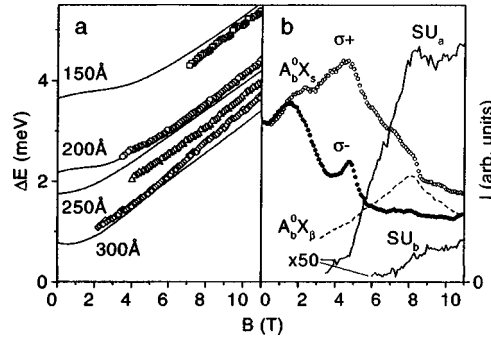
FIG. 3. (a) Magnetic field dependence, measured for 150 Å (□), 200 Å (○), 250 Å (△), and 300 Å(◇) SQWs, of the splitting between the $A_b^0 X$ and SU_a lines in σ polarization. The lines show the dependence of the splitting calculated for the same quantum wells with distances to the acceptor 50, 100, 100, and 500 Å, respectively. (b) Magnetic field dependence of the intensity, measured in a 200 Å SQW, of the spectral components of the emission line of an $A_b^0 X$ complex of the singlet type (s) in two circular polarizations (symbols) and of a β multiplet (dashed line) as well as the replicas $SU_{a,b}$ (solid lines) in σ polarization.

mainly on distant acceptors? The most likely explanation is that in charged quantum wells, where the free-hole density is much higher than the exciton density, virtually all acceptors in and close to the well it each trap two holes and form A^+ centers. Exciton localization on such a center is energetically unfavorable because of the Pauli principle. At the same time, it is well known that as the acceptor center moves away from the well boundary into the barrier, the binding energy of the second hole in an A^+ center decreases rapidly and vanishes when $L > 2.5 a_B$.[11] For this reason, at a certain distance of the acceptor from the well, localization of an exciton should become energetically more favorable.

Another question concerns the nature of the ground state of the $A_b^0 X$ complex (and X^+) and its variation with increasing magnetic field. It is well known that in a zero field the ground state of such a complex is a singlet (i.e., a wave function with $J = M^e - M^h - S^h = 0$).[2] This means that when a complex with electron spin $S_z^e = +1/2$ recombines, a σ-polarized photon should be emitted, and in the final state the A_b^0 center should have total angular momentum $J_z = -3/2$. However, this set of levels has no splittings corresponding to the experimental results, for all possible values of L. This circumstance forces us to infer that the replicas $SU_{a,b}$ arise in the process of recombination of an $A_b^0 X$ complex of a multiplet type. Indeed, in the case of X^- the triplet state becomes bound in magnetic fields greater than ~ 2 T, but the singlet state remains a ground state in the entire experimentally studied range of magnetic fields.[1] At the same time, it is known that in the strong-field limit the ground state of a two-electron system should be a triplet state.[12] In the case of a complex containing two holes, aside from a singlet with $J = 0$, several multiplets with $J = 1$, 2, and 3 are possible. The spectra which we obtained do indeed contain two additional lines, denoted in Fig. 1d by the symbols α and β. They appear in σ polarization above the singlet (s). Previous authors have attributed the β line to the triplet state X^+,[2] though in the present case the value of J is not obvious *a priori*. A much larger spin splitting of a hole compared with the electron can radically change the ratio of the energies of the singlet and multiplet states in a magnetic field. The change in the type of ground state (from singlet to multiplet) may not be accompanied by

crossing of the spectral luminescence lines, since they have different final states in recombination. The singlet has a final state with $J_z = -3/2$ (shown by the dotted line in Fig. 2a), while multiplets can recombine in a state with $J_z = +3/2$ (the line *A* in Fig. 2a). The energy difference of these two states plus the electron Zeeman splitting ΔE^e equals the difference of the energies of the $\sigma+$ and $\sigma-$ components of the recombination line of the singlet. For this reason, the multiplet state lies at a lower energy than the singlet state, where the corresponding line in σ polarization is more than ΔE^e lower than the $\sigma+$ component of the singlet. Changes should also be expected to occur in the magnetic field dependences of the intensity of the spectral lines, shown in Fig. 3b for a 200 Å SQW. As one can see from the figure, the intensity of the singlet components has a pronounced maximum near $B = 4.8$ T. The above-indicated condition for an α multiplet holds here (Fig. 1d). The intensity of the replicas $SU_{a,b}$ starts to increase in the same field. This confirms the assumption that they are related with recombination of not a singlet but rather an α multiplet. The second special point near $B = 8.1$ T is related with the equality of the energies of the singlet and β multiplet. A resonance transfer of energy gives rise to a maximum of the intensity of the β multiplet, while a sharp drop is observed in the intensity of the singlet. We observed a similar behavior for the other samples investigated, and in addition the dependence of the critical fields on the well width was found to be quite weak. It should be noted that a multiplet state is optically inactive in the strong-field limit.[12] This could be the reason why the intensity of the luminescence of an α multiplet is relatively low (Fig. 1b and 1c), despite the fact that the multiplet corresponds to the ground state of the system. At the same time, the smallness of the matrix element of the transition to the ground state of an A_b^0 center produces conditions for observing replicas associated with transitions to excited states.

4. In summary, we observed and studied in the emission spectrum of an excitonic complex localized on a neutral acceptor satellites of the main recombination line which are associated with transitions to an excited state of an impurity center after a recombination event. It was shown that the observed energy splittings between the replicas and the main line correspond to the arrangement of an acceptor in the barrier at a definite distance from the well. It was demonstrated that the replicas are due to radiation from the multiplet state that becomes the ground state of the exciton complex as the magnetic field increases.

[a] e-mail: volkov@issp.ac.ru

---

[1] A. J. Shields, M. Pepper, D. A. Ritchie and M. Y. Simmons, Adv. Phys. **44**, 47 (1995).
[2] A. J. Shields, J. L. Osborne, M. J. Simmons *et al.*, Phys. Rev. B **52**, R5523 (1995).
[3] O. V. Volkov, V. E. Zhitomirskiĭ, I. V. Kukushin *et al.*, JETP Lett. **66**, 766 (1997).
[4] O. V. Volkov, V. E. Zhitomirskiĭ, I. V. Kukushin *et al.*, JETP Lett. **67**, 744 (1998).
[5] J. Rorison, D. C. Herbert, P. J. Dean, and M. S. Skolnik, J. Phys. C **17**, 6435 (1984).
[6] G. Finkelstein, H. Shtrikman, and I. Bar-Joseph, Phys. Rev. B **53**, 12593 (1996).
[7] J. L. Osborne, A. J. Shields, M. Pepper *et al.*, Phys. Rev. B **53**, 13002 (1996).
[8] J. M. Luttinger, Phys. Rev. **102**, 1030 (1956).
[9] G. E. W. Bauer and T. Ando, Phys. Rev. B **38**, 6015 (1988).

[10] O. V. Volkov, V. E. Zhitomirskii, I. V. Kukushkin *et al.*, Phys. Rev. B **56**, 7541 (1997).
[11] H. L. Fox and D. M. Larsen, Phys. Rev. B **51**, 10709 (1995).
[12] J. J. Palacios, D. Yoshioka, and A. H. MacDonald, Phys. Rev. B **54**, R2296 (1996).

Observation of self-generation of dark envelope solitons for spin waves in ferromagnetic films

B. A. Kalinikos[a)] and N. G. Kovshikov

St. Petersburg State Electrotechnical University, 197376 St. Petersburg, Russia

C. E. Patton

Colorado State University, Fort Collins, Colorado, USA

We have performed experiments in which self-generation of dark envelope solitons for spin waves at microwave frequencies were obtained. Stable self-generation of dark solitons was observed in a ring consisting of tangentially magnetized yttrium iron garnet film and a microwave signal amplifier. © *1998 American Institute of Physics.*
[S0021-3640(98)01315-2]

PACS numbers: 75.30.Ds, 75.70.Ak

It is well known that two types of envelope solitons can propagate in nonlinear waveguiding dispersive media — bright solitons and dark solitons (see, for example, Ref. 1). Most experimental works concern bright solitons. Here bright solitons in optical fibers[2] as well as solitons for spin waves in ferromagnetic films (see, for example, Refs. 3–6 and the literature cited there) are in the leading position. At the same time, the generation and propagation of dark optical solitons (detailed information about which can be found in the recent review Ref. 7) and spin-wave solitons (we know of only one work, Ref. 8) have clearly not been adequately investigated.

In the present letter we report the experimental observation of the generation of dark envelope solitons for spin waves at microwave frequencies. Just as in Ref. 6, where generation of bright solitons was obtained, a ring consisting of an yttrium iron garnet film (YIG) and a microwave signal amplifier was used for the experiment. We underscore that an external microwave signal was not introduced into the circuit. In other words, self-generation of dark microwave solitons was observed.

Previous experiments devoted to the investigation of bright envelope solitons of both weakly and strongly dispersive spin waves have found a good explanation in the nonlinear Schrödinger equation (NES) model. For this reason, this model was used to formulate the experiment described. According to the NES model,

$$i(\partial u/\partial t + V_g \partial u/\partial x) + (D/2)\partial^2 u/\partial^2 x - N|u|^2 u = 0, \tag{1}$$

dark envelope solitons can be observed in waveguiding media if the dispersion and nonlinear coefficients of the carrying wave have the same signs. A quasisurface spin wave propagating in tangentially magnetized ferromagnetic films in a direction perpen-

dicular to the bias magnetization field satisfies this requirement. In the case of single-crystal YIG films, which have free surface spins, such a wave has monotonic dispersion $\omega(k)$ in the long-wavelength region of the spectrum $kL \ll 1$.[9] Its dispersion coefficient $D = \partial^2\omega/\partial^2 k$ and nonlinear coefficient $N = \partial\omega/\partial|u|^2$ are negative.

The experiments were performed on samples in the form of narrow, 1.5 mm wide, strips of YIG films (spin-wave ''waveguides''). The waveguides were cut from single-crystal YIG films of thickness $L = 5.2\,\mu$m grown on a (111) gadolinium-gallium garnet substrate. The spin waves were excited and detected with the standard ''delay line'' arrangement[3,4] with short-circuited exciting and detecting microstrip antennas, each of width 50 μm and length equal to the width of the film waveguide. The distance between the antennas, formed photolithographically on mobile ceramic substrates, could be regulated. The spin-wave waveguides were placed on top of the antennas.

The spin-wave delay line described above was connected with a wideband microwave signal amplifier (the working frequency band of the amplifier was greater than 300 MHz) and a microwave signal modulator into a closed circuit — a ring. We underscore that for all microwave signal levels employed the amplifier always operated in a clearly linear regime. Therefore the nonlinear properties of the ring were determined by the nonlinearity of the spin system of the ferromagnetic film. The modulator was used for periodic ''interruption'' of the ring for short time intervals several to ten nanoseconds in duration. Having in mind a comparison with theory, it is important to note that the modulator employed could not give complete interruption of the ring. The attenuation introduced by the modulator relative to the constant (maximum) level of the circulating microwave signal was equal to 41 dB. In other words, in the existing terminology[2,7] the modulator supported a generation regime for gray solitons.

An apparatus similar to that described in Ref. 6 was used for measurements. The experiments can be conventionally divided into two stages. At the first stage the waveguiding properties of the ring were investigated. Specifically, the spectrum of the resonance frequencies of the ring was measured with different gains of the circulating microwave signal. These measurements were performed without modulation of the ring. At the second stage generation processes, where the modulator provided modulation of the signal in the ring, were investigated.

Figure 1a shows the amplitude–frequency characteristic of the ring, measured with a gain slightly below the threshold for the appearance of microwave generation in the ring. This characteristic reflects the resonance properties of the ring in a regime with almost complete compensation of losses in it. The wave numbers k_n of the resonant spin waves can be found from the condition $k_n d + \phi = 2\pi n$, where d is the distance between the spin-wave antennas, ϕ is the phase shift of the signal due to the part of the circuit outside the ferromagnetic film, and n is an integer. This resonance condition makes it possible to determine the dispersion relation $\omega(k)$ of the spin waves according to the experimental peaks in Fig. 1a. Such an equation was found in the course of the work as the dispersion relation of the lowest quasisurface wave mode.[9] A calculation using the obtained dispersion relation gave the following spin-wave parameters: group velocity $V_g = 2.9 \times 10^6$ cm/s, dispersion coefficient $D = -3310$ cm/rad$\cdot$s, and nonlinear coefficient $N = -9.2 \times 10^9$ rad/s. (The values of the parameters V_g, D, and N are given for the central carrying frequency, which is determined below.)
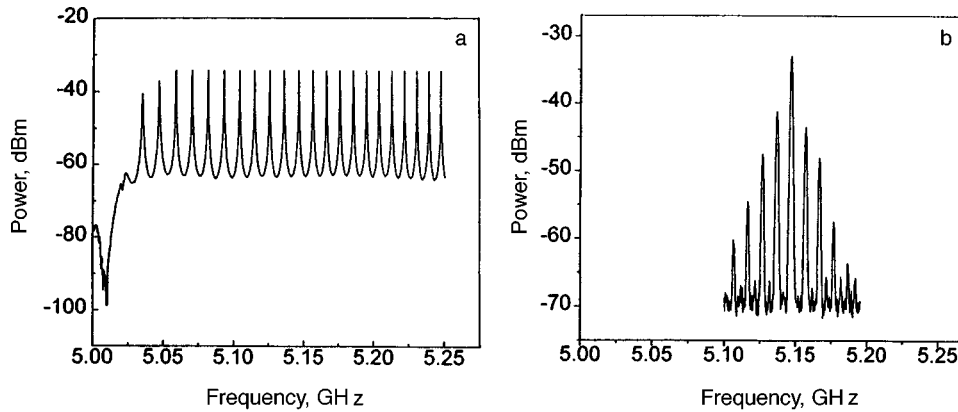
FIG. 1. Amplitude–frequency characteristic of the experimental ring (a) and frequency spectrum of the self-generated train of dark solitons (b).

At the second stage, experiments on self-generation of envelope solitons for spin waves were performed. The experiments were performed in a regime of periodic modulation of the ring by square ''dark'' pulses. In the experiments the envelope of the generated signal and its phase characteristic as well as the frequency spectrum of generation were measured simultaneously. To obtain stable self-generation several adjustments were made: 1. The distance d between the input and output antennas was adjusted to ensure that the circulation time t_0 of the microwave spin-wave pulses in the ring equals the external modulation period (here $t_0 = d/V_g + t_e$, where t_e is the propagation time of a microwave pulse outside the ferromagnetic film). 2. The ring gain was adjusted to compensate losses and achieve stable self-generation of dark microwave solitons. 3. The duration τ_{in} of the external pulses fed into the modulator was adjusted to obtain temporal profiles of the amplitude and phase of the envelope of the microwave signal that correspond to dark solitons.

It is important to note that in terms of frequencies the first condition corresponds to the condition that the spectral frequencies of the generated train of nonlinear pulses equal the characteristic frequencies of the ring. Satisfaction of this condition for a nonlinear propagation regime of spin-wave pulses was one of the main ideas of this experiment.

The results illustrating the regime of self-generation of dark solitons are presented in Fig. 2. The oscillograms shown in this figure were recorded with a periodic sequence of dark square pulses with duration $\tau_{in} = 22$ ns and clock rate 10 MHz fed to the modulator. The measurements were performed for the following parameters: distance between the input and output antennas $d = 2.3$ mm, total circulation time of the microwave pulses along the ring $t_0 = 100$ ns, and pulse propagation time outside the ferromagnetic film $t_e = 20$ ns. The power of the spin waves at the exit of the delay line was equal to 0.9 mW. Figure 2a shows a self-generated sequence of microwave pulses — dark spin-wave envelope solitons, while Fig. 2b shows its phase characteristic. (The measurements were performed with an HP70820A microwave transition analyzer.) The frequency spectrum of this sequence is displayed in Fig. 1b; the spectrum was obtained with a HP859E spectrum analyzer. As follows from the measurement results, in the case described self-
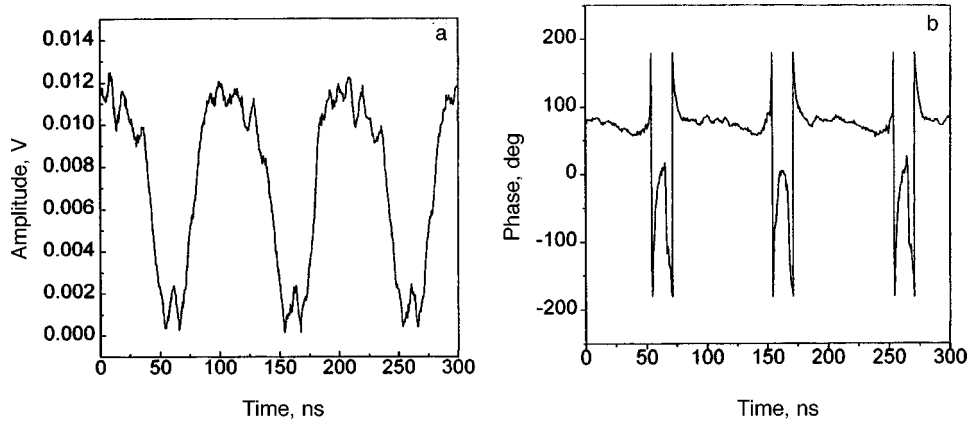
FIG. 2. Temporal profile of the envelope of a train of dark solitons (a) and its phase characteristic (b).

generation of dark solitons was observed with nonlinear self-synchronization of more than 10 ring modes.

We note that the phase characteristic was recorded with a 5146.6 MHz reference signal fed into the HP70820A. This frequency was set exactly equal to the central carrying frequency of the self-generating train of dark solitons (see Fig. 1b). The phase characteristic in Fig. 2b demonstrates two sharp changes in the phase of the carrying microwave signal (by 180° each), which occur ''inside'' the dark pulses; this is direct evidence of their soliton character. The propagation velocity of the dark solitons in a YIG film, within the limits of the measurement error which we estimate to be 10%, equals the group velocity of spin waves at the central frequency.

We shall now give a more detailed description of the data in Fig. 2. We note that each pulse of the self-generated sequence is always obtained with two minima in its profile (at the ''bottom'' of the pulse) (see Fig. 2a). Rapid changes in phase correspond to a change in the signal amplitude near these minima: one by $+180°$ and the other by $-180°$. This behavior of the signal phase indicates that the observed nonlinear dark pulses can be interpreted as pairs of dark solitons. (We note that the abrupt 360° phase kicks, which correspond to the vertical lines in Fig. 2b, are purely instrumentation effects: They are due to a characteristic operational feature of the HP70820A and should be ignored.) On the whole, the two fast 180-degree phase changes occurring during a dark pulse compensate one another and the resulting phase of the carrying microwave signal does not change. This experimental fact corresponds to the theory of the generation of a pair of dark solitons from a square pulse.[7,10,11]

We note in passing that the above-described behavior of the phase of a pair of dark solitons is fundamentally different from the case of bright solitons, where the phase of the carrying signal remains constant over the duration of the spin-wave soliton.[6]

In conclusion, we note that the obtained nonlinear pulsed spin-wave self-generation confirms theoretical ideas about dark envelope solitons. We believe that both the above-described experiments on self-generation of dark spin-wave solitons and the experiments

presented in Ref. 6 on self-generation of bright spin-wave solitons can be extended to diverse continuous and discrete waveguiding media.

[a]e-mail: borisk@borisk.usr.etu.spb.ru

[1] M. Remoissenet, *Waves Called Solitons: Concepts and Experiments,* Spinger-Verlag, Berlin, 1996.

[2] J. R. Taylor (Ed.), *Optical Solitons – Theory and Experiment*, Cambridge University Press, Cambridge, 1992.

[3] B. A. Kalinikos, N. G. Kovshikov, and A. P. Slavin, Zh. Éksp. Teor. Fiz. **94**, 159 (1986) [Sov. Phys. JETP **67**, 303 (1986)].

[4] M. Chen, M. A. Tsankov, J. M. Nash, and C. E. Patton, Phys. Rev. B **49**, 12773 (1994).

[5] R. Marcelli and P. DeGasperis, IEEE Trans. Magn. **MAG-30**, 26 (1994).

[6] B. A. Kalinikos, N. G. Kovshikov, and C. E. Patton, Phys. Rev. Lett. **80**, 4301 (1998).

[7] Yu. S. Kivshar and B. Luther-Davies, ''Dark optical solitons: physics and applications,'' Phys. Rep. **298** (2–3), pp. 81–197 (1998).

[8] M. Chen, M. A. Tsankov, J. M. Nash, and C. E. Patton, Phys. Rev. Lett. **70**, 1707 (1993).

[9] B. A. Kalinikos, M. P. Kostylev, N. V. Kozhus, and A. N. Slavin, J. Phys.: Condens. Matter **2**, 9861 (1990).

[10] S. A. Gredeskul and Yu. S. Kivshar, Phys. Rev. Lett. **62**, 977 (1989).

[11] V. F. Dmitriev and B. A. Kalinikos, Izv. Vyssh. Uchebn. Zaved. Fiz. **31**, 24 (1988).

Translated by M. E. Alferieff

Free and localized excitons in the luminescence spectrum of C_{60} crystals at high pressure

K. P. Meletov[a)] and V. D. Negriĭ

Institute of Solid-State Physics, Russian Academy of Sciences, 142432 Chernogolovka, Moscow Region, Russia

The luminescence spectra of C_{60} single crystals are studied at $T \cong 10$ K and pressure up to 4.0 GPa. It is observed that as the pressure increases, one fine-structure band in the spectrum intensifies sharply and dominates at pressures $P \geqslant 1.7$ GPa. The pressure shift of this band is much larger than the shift of other bands in the spectrum, and its magnitude correlates with the pressure dependence of the band gap. It is shown that this band could be due to radiative recombination of free Frenkel excitons. © *1998 American Institute of Physics.*
[S0021-3640(98)01415-7]

According to the quantum-chemical calculations of the structure and electronic spectrum of C_{60}, the first excited singlet state of the molecule possesses $^{1}T_{1g}$ symmetry and optical dipole transitions are forbidden for it.[1,2] The allowed transitions correspond to states with $^{1}T_{1u}$ symmetry and lie appreciably higher in energy. This explains the quite low fluorescence quantum yield of C_{60}: $\sim 10^{-5}$ and $\sim 7 \times 10^{-4}$ for solutions and crystals, respectively.[3,4] The fluorescence of C_{60} solutions is due to electronic-vibrational transitions involving non-fully symmetric intramolecular vibrations, allowed in the Herzberg–Teller approximation.[5] The increase of the luminescence quantum yield of C_{60} in the condensed state is due to the formation of defects of a various kinds, which results in partial lifting of the symmetry forbiddenness of optical transitions. The low-temperature luminescence spectrum of C_{60} single crystals of high purity and perfection has a line structure, separate bands of which are due to radiative recombination of excitons localized on traps of various depths.[6] The structure and intensity of the luminescence spectrum depends strongly on the defect density of the crystals, irradiation by light in a definite wavelength range, and thermobaric treatment of the samples.[7,8] Experiments on second-harmonic generation near the $^{1}T_{1g}$ molecular electronic transition, specifically, data on its spectral and temperature dependences, attest to the presence of Frenkel excitons in the spectrum of collective excitations of the C_{60} crystal.[9] Some bands in the luminescence spectrum of C_{60} crystals could be due to radiative recombination of free Frenkel excitons, and their classification requires special experiments. As is well known, the pressure shift of levels in molecular crystals is substantially different for localized and extended excitonic states, which makes it possible to distinguish them in experiments at high pressure.[10,11]
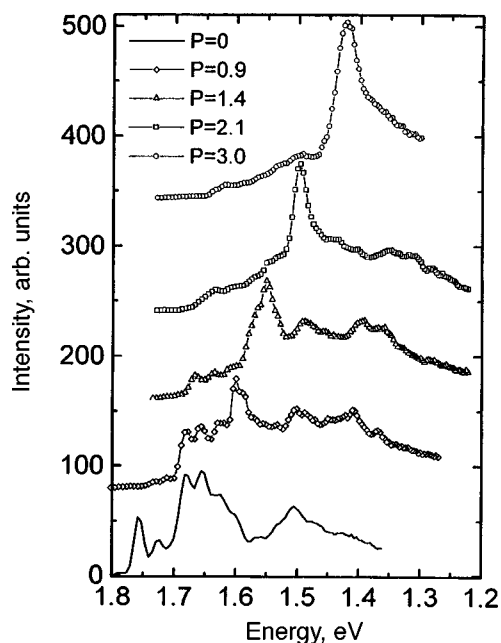
FIG. 1. Luminescence spectra of C_{60} single crystals at $T \cong 10$ K and pressures up to 3.0 GPa.

In this connection, in the present work we measured the low-temperature luminescence spectrum of perfect C_{60} crystals at high pressure. The pressure shift of different fine-structure bands in the luminescence spectrum was determined, and the contribution of free and localized excitons in the secondary-emission spectrum was determined on the basis of these data.

High-quality single crystals, grown in an evacuated quartz tube from vapors of C_{60} powder of purity not worse than 99.99%, were used to measure the luminescence spectrum.[7] The measurements of the spectra were performed on a DFS-12 monochromator with a cooled FÉU-62 and a 5S1 photon-counting system. The automated system included a TV camera to obtain a monochomatic image of the sample with magnification ~ 150, employed for precise monitoring of the position of the laser spot on the sample. The luminescence was excited with a helium–neon laser, whose power was limited in order to exclude photochemical processes.[12] High-pressure measurements in liquid-helium vapors were performed using a miniature chamber with diamond anvils of the Merrill–Bassett type, placed in a helium optical thermostat. A 4:1 methanol–ethanol mixture was used to transmit the pressure.[13] The magnitude of the pressure was determined from the position of the R_1 luminescence line of ruby to within ~ 0.05 GPa.[14] The measurements were performed on crystals with a mirror-smooth surface and dimensions $\sim 100 \times 100 \times 40 \ \mu$m, close to those of the working volume of the high-pressure chamber.

The luminescence spectra of C_{60} single crystals at $T \simeq 10$ K and pressure up to 3.0 GPa are presented in Fig. 1. The initial luminescence spectrum under normal pressure has a characteristic fine structure, identical to that observed earlier in Refs. 6 and 7. It starts
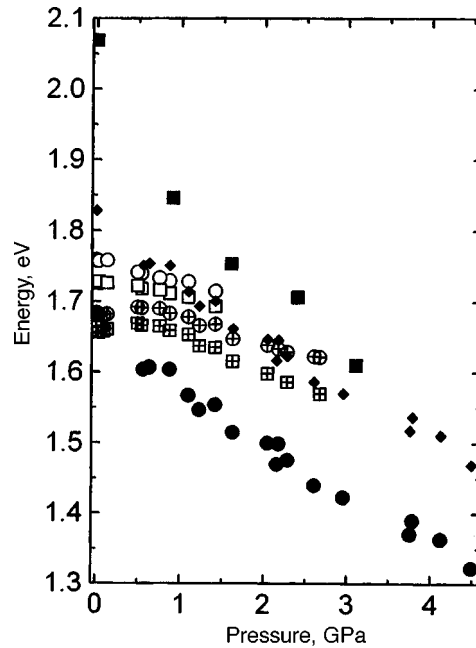
FIG. 2. Pressure dependence of the spectral position of the bands in the low-temperature luminescence spectrum of C_{60} crystals.

with the bands corresponding to radiative recombination of excitons localized on impurity or defect centers, collectively referred to Ref. 6 as X traps. In accordance with the designations of this work, the initial bands of the spectrum correspond to X_2 and X_3 traps, as well as the so-called ''bulk-emission'' C band. As the pressure increases, the spectrum shifts in the direction of lower energies, and intensity is gradually redistributed in favor of the C band. At pressures $P \geqslant 1.7$ GPa the C band becomes appreciably more intense than all other bands in the spectrum, and as the pressure increases further, this band dominates the spectrum. At the same time, the bands corresponding to X traps become weaker, the weakening being especially appreciable for X_2 traps even at the initial pressure. All changes are reversible, and the initial pattern of the spectrum is restored when the pressure is removed.

The pressure dependence of the spectral position of the main luminescence band is displayed in Fig. 2. The open circles and squares show the data for X_2 traps, and the same symbols with crosses show the data for X_3 traps. The filled circles correspond to the C band, while the filled squares show the pressure dependence of the band gap, obtained earlier from the absorption spectra.[15] The filled diamonds in Fig. 2 show the spectral position shifted with respect to the C band in the direction of higher energies by the frequency $\Omega = 1183$ cm^{-1} of the F_{1u} phonon. All bands in the luminescence spectrum of C_{60} are shifted in the direction of lower energies. On the whole this is characteristic for crystals with van der Waals interaction.[11,15] The rate of the pressure shift of the bands corresponding to X traps is approximately three times lower than for the C band. At the same time, the pressure dependence of the position of the C band is close to that of the

band gap of the crystal. It should also be noted that the pressure dependence of the position of the X_3 traps changes at ~ 0.5 GPa from a weakly increasing dependence to a decreasing one. This feature is due to a phase transition of orientational ordering in C_{60} crystals at high pressure. A phase transition at this pressure was observed in calorimetric investigations of C_{60}[16] and then in Raman scattering experiments at high pressure.[17,18]

The activation character of the temperature dependence of the X-trap bands in the luminescence spectrum[6] undoubtedly indicates that they are centers of localization of excitons. The data obtained in the present work on the pressure dependence of the luminescence spectrum attest to the different nature of the C band and the X-trap bands. The sharp intensification of the C band with increasing pressure and the high rate of the pressure shift and its correlation with the pressure dependence of the band gap attest to the fact that this band could be due to radiative recombination of free Frenkel excitons. Experiments on second-harmonic generation in C_{60} crystals show that the energy of the lowest state, corresponding to free excitons with $^1T_{1g}$ symmetry, equals ~ 1.827 eV. Zero-phonon optical transitions corresponding to radiative recombination of free excitons from the state $^1T_{1g}$ into the ground state $^1A_{1g}$ are forbidden by the symmetry selection rules. At the same time, the electronic–vibrational transitions between these states are possible: The symmetry selection rules allow participation of non-fully symmetric phonons A_u, H_u, and F_{1u} in them in the Herzberg–Teller approximation.[5] The spectral position and pressure dependence of the intensity of the C band show that this band could be due to such a transition. Indeed, since its energy at normal pressure equals ~ 1.68 eV (data of Ref. 7 and the present work), the frequency of an intramolecular phonon partici-pating in this transition must equal ~ 1185 cm^{-1}. This value is virtually identical to the frequency ~ 1183 cm^{-1} obtained for the F_{1u} phonon from measurements of the infrared absorption spectra of C_{60} films.[19] The increase in the intensity of the C band with in-creasing pressure could be due to a change in the population of the $^1T_{1g}$ state, occurring as a result of a substantial restructuring of the energy spectrum of the crystal at high pressure. At the same time, the Herzberg–Teller transitions in molecular crystals can intensify with increasing pressure. According to Ref. 5, the matrix element of the tran-sition between electronic–vibrational states 00 and nk in the Herzberg–Teller approxi-mation has the form

$$M_{0,nk} = M_{0,n}^0 \int \Psi_{00}(R)\Psi_{nk}(R)dR + \sum_s{}' M_{0,s}^0 \int \Psi_{00}(R)\{W_{ns}(R)/(E_s^0 - E_n^0)\}\Psi_{nk}(R)dR.$$

(1)

Here $M_{0,n}^0$ and $M_{0,s}^0$ are zeroth-order matrix elements for transitions between the ground and excited electronic states 0 and $n \ldots s$; $\Psi_{00}(R)$ and $\Psi_{nk}(R)$ are wave functions of the 00 and nk vibrations; $W_{ns}(R)$ is the matrix element of the linear term in the series expansion of the energy of the molecule in small displacements of the nuclei; E_s^0 and E_n^0 are the eigenenergies in zeroth order; and, the prime on the sum signifies that the sum-mation extends over all s electronic states except $s = n$. The first term in Eq. (1) equals zero, since the electronic transition $^1T_{1g} \Rightarrow {}^1A_{1g}$ is dipole-forbidden. In the second term, the terms in the summation which contain matrix elements of the dipole-allowed transi-tions $^1T_{1g} \Rightarrow {}^1A_{1g}$ are different from zero, while the expressions in the integrand contain wave functions of A_u, H_u, or F_{1u} phonons. The term corresponding to the lowest electronic state of symmetry $^1T_{1u}$, for which the energy denominator $(E_s^0 - E_n^0)^{-1}$ is

maximum, makes the dominant contribution in this sum. Since the energy gap $E_s^0 - E_n^0$ between the $^1T_{1g}$ and $^1T_{1u}$ states decreases with increasing pressure, the Herzberg–Teller matrix element should increase and the transition should intensify. This effect in pure form can be manifested in the absorption spectrum, where the influence of the population of the electronic states on the transition intensities is excluded.

In summary, the pressure dependence of the spectral position and intensity of the C band in the low-temperature luminescence spectrum of C_{60} crystals attests to the fact that this band could be due to radiative recombination of free $^1T_{1g}$ excitons with the creation of a $\Omega = 1183$ cm^{-1} phonon with F_{1u} symmetry.

[a]e-mail: mele@issp.ac.ru

---

[1] F. Negri, G. Orlandi, and F. Zerbetto, Chem. Phys. Lett. **144**, 31 (1988).

[2] F. Negri, G. Orlandi, and F. Zerbetto, J. Chem. Phys. **97**, 6496 (1992).

[3] Y. Wang, J. Phys. Chem. **96**, 764 (1992).

[4] P. A. Lane, L. S. Swanson, Q.-X. Ni *et al.*, Phys. Rev. Lett. **68**, 887 (1992).

[5] G. Herzberg and E. Teller, Z. Phys. Chem. B **21**, 410 (1933).

[6] W. Guss, J. Feldmann, E. O. Göbel *et al.*, Phys. Rev. Lett. **72**, 2644 (1994).

[7] V. D. Negrii, V. V. Kveder, Yu. A. Ossipyan *et al.*, Phys. Status Solidi B **199**, 587 (1997).

[8] I. O. Bashkin, A. N. Izotov, A. P. Moravsky *et al.*, Chem. Phys. Lett. **272**, 32 (1997).

[9] A.-M. Janner, R. Eder, B. Koopmans *et al.*, Phys. Rev. B **52**, 17158 (1995).

[10] S. I. Gaidai, K. P. Meletov, and M. F. Shanov, Phys. Status Solidi B **141**, 211 (1987).

[11] S. I. Gaĭdaĭ and K. P. Meletov, Fiz. Tverd. Tela (Leningrad) **34**, 650 (1992) [Sov. Phys. Solid State **34**, 347 (1992)].

[12] A. M. Rao, P. Zhou, K.-A. Wang *et al.*, Science **259**, 955 (1993).

[13] A. Jayaraman, Rev. Sci. Instrum. **57**, 1013 (1986).

[14] D. Barnett, S. Block, and G. J. Piermarini, Rev. Sci. Instrum. **44**, 1 (1973).

[15] K. P. Meletov, V. K. Dolganov, O. V. Zharikov *et al.*, J. Phys. I France **2,** 2097 (1992).

[16] G. A. Samara, J. E. Schirber, B. Morosin *et al.*, Phys. Rev. Lett. **67**, 3136 (1991).

[17] N. Chandrabhas, M. N. Shashikala, D. V. S. Muthy *et al.*, Chem. Phys. Lett. **197**, 319 (1992).

[18] K. P. Meletov, D. Christofilos, S. Ves *et al.*, Phys. Rev. B **52**, 10090 (1995).

[19] D. S. Bethune, G. Meijer, W. C. Tang *et al.*, Chem. Phys. Lett. **179**, 181 (1991).

Translated by M. E. Alferieff

C$_{60}$ fullerite with a "stretched" fcc lattice

Yu. M. Shul'ga[a)] and B. P. Tarasov

Institute of Chemical Physics, Russian Academy of Sciences, 142432 Chernogolovka, Moscow Region, Russia

It is shown that deuteration of C$_{60}$ fullerite followed by thermal decomposition of the resulting deuteride C$_{60}$D$_{24}$ leads to the formation of an fcc lattice with $a_0 = 14.52$ Å in the final product, which according to the IR spectra consists mainly of C$_{60}$ fullerene molecules. © *1998 American Institute of Physics.* [S0021-3640(98)01515-1]

PACS numbers: 61.48.+c, 81.05.Tp

It is widely known that for the compounds A$_3$C$_{60}$, where A is an alkali metal, the superconducting transition temperature T_c increases together with the lattice constant of the fcc lattice of this compound.[1,2] The structure-forming element in A$_3$C$_{60}$ compounds are fullerene molecules, while the alkali metal atoms "dope" the material with electrons.

Molecular hydrogen cannot be considered as a donor, since as temperature increases, it can enter into a chemical reaction with a fullerene molecule to form a hydride. Moreover, it has been established[3] that the hydride C$_{60}$H$_{36}$ crystallizes in a bcc structure with $a_0 = 11.715$ Å. However, hydrogenation of solid C$_{60}$ fullerene (fullerite) with hydrogen gas at low pressure and temperature preserves the fcc lattice of fullerite.[4] It is also known from the literature that on being heated in vacuum, the fullerene hydride is converted to the initial fullerene.[5,6]

In the present letter we describe data from a study of fullerite subjected to deuteration followed by degassing at 823 K, as a result of which the lattice parameter of the fullerite increased from 14.17 to 14.52 Å.

We employed crystalline C$_{60}$ fullerite with 99.8 mass% purity. Deuteration was conducted at pressure 2.5 MPa and temperature 673 K. Preliminary degassing of the fullerite was performed by heating up to 500 K in vacuum (~ 1 Pa). To improve the efficiency, the deuteration process was conducted in a cyclic thermal regime, i.e., the sample under pressure by deuterium was heated up to 673 K and held at this temperature for 1 h, after which the reaction mixture was cooled to room temperature and the cycle was repeated at least five times. Degassing of the deuteride was conducted in the regime of thermogravimetric analysis: The sample (50 mg) was heated in an inert atmosphere at a rate of 10 deg/min from room temperature up to 823 K.

The diffraction patterns were recorded on an ADP-1 diffractometer (Cu$K\alpha$ radiation). The IR spectra were recorded with a Perkin Elmer 1720X Fourier spectrometer. The samples for investigating the IR spectra were prepared in the form of tablets with
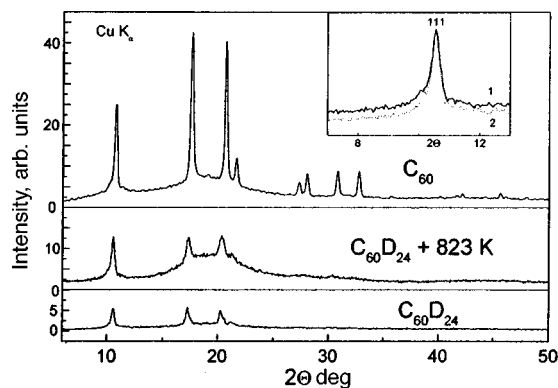
FIG. 1. Powder diffraction patterns of the initial fullerene, fullerene deuteride $C_{60}D_{24}$, and the product of the thermal decomposition of the deuteride. Inset: Superposition of the diffraction patterns of PTDD (1) and $C_{60}D_{24}$ (2).

KBr. The x-ray photoelectron (XPE) spectra, carrying information about the state of a thin (10–40 Å) near-surface layer of the solid, were excited by Al$K\alpha$ radiation ($h\nu = 1486.6$ eV). The preparation of the samples for investigating the XPE spectra is described in detail in Ref. 7. The deuterium content was determined by the standard method of burning the sample in an oxygen stream and performing quantitative analysis of the water formed.

As one can see from Fig. 1, the fcc lattice of the initial fullerite is preserved in the deuteride $C_{60}D_{24}$. However, the diffraction pattern of the deuteride differs from that of the fullerite by both a shift and asymmetric broadening of the main peaks (Fig. 2). The fcc lattice constant in $C_{60}D_{24}$ equals 14.55 Å. Degassing this deuteride at 823 K leads to a slight increase in the intensity and a decrease in the asymmetry of the peaks in its diffraction pattern and to a shift of the centroids of the lines in the direction of shorter interplanar distances (Fig. 1). Nonetheless, the diffraction pattern of the product of thermal decomposition of deuteride (PTDD) differs considerably from the diffraction pattern
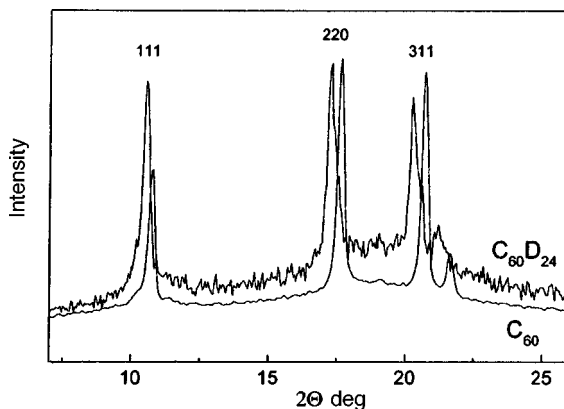

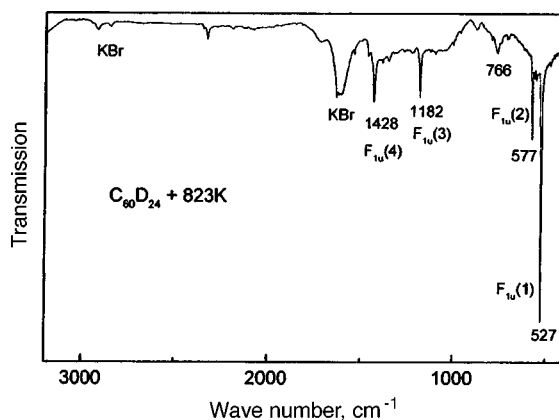FIG. 2. Superposition of the diffraction patterns of the initial fullerene and fullerene deuteride $C_{60}D_{24}$.

FIG. 3. IR spectrum of the product of thermal decomposition of the deuteride $C_{60}D_{24}$. F_{1u} denotes IR-active modes of the C_{60} molecule.

of the initial fullerite. An estimate of the effective size of the crystallites according to the half-widths of the three strongest lines gives values in the range 300–1200 Å for PTDD. The estimate was made under the assumption that for the initial fullerite this quantity exceeds the limit at which the physical broadening of the lines designated is virtually identical to zero. The value of a_0 for PTDD is still quite large (14.52 Å). It may be inferred that doping such a sample with alkali metals can be quite successful. Specifically, one can attempt to obtain by this method the superconductor A_3C_{60} with high T_c and an alkali metal with a low atomic number.

The strongest absorption bands (ABs) in the IR spectrum of PTDD (Fig. 3) have the same position and shape as the IR-active modes (F_{1u}) of the high-symmetry (I_h) C_{60} molecule. This means that under the treatment described above the deuteride is converted into fullerene. The wide AB at ~ 1630 cm^{-1} and the weak ABs at 2845 and 2920 cm^{-1} are due to, respectively, water and hydrocarbon molecules adsorbed by the KBr tablet. The IR spectrum of PTDD also contains a quite intense AB with a maximum at 766 cm^{-1} that is absent in the IR spectrum of the initial fullerite. The presence of a series of bands in the region 700–800 cm^{-1} is often attributed[8] to the formation of fullerene polymers, for example, polymers obtained both by photopolymerization and by the action of high pressures and temperatures on C_{60}. In this range there are a number of ABs, some of which lie close to the AB at 766 cm^{-1} and to other weaker ABs present in the designated region in the PTDD spectrum. The existence of polymer formations in the experimental sample cannot be an obstacle to doping the sample for the purpose of obtaining a superconductor, since it has been shown that Na_2CsC_{60} polymerizes at pressure 300 MPa, and the superconducting properties are preserved in the process.[9]

The XPE spectra of $C_{60}D_{24}$, the product of its thermal decomposition, and pure C_{60} are displayed in Fig. 4. One can see that the position of the maximum of the main peak in the case of the deuteride is shifted to lower binding energies compared with pure C_{60}. The half-width of the C_{1s} peak in the deuteride is larger than in pure C_{60}. In the process of thermal decomposition of the deuteride, this peak becomes narrower and its centroid shifts in the direction of higher binding energies. A satellite is present in the spectra of all
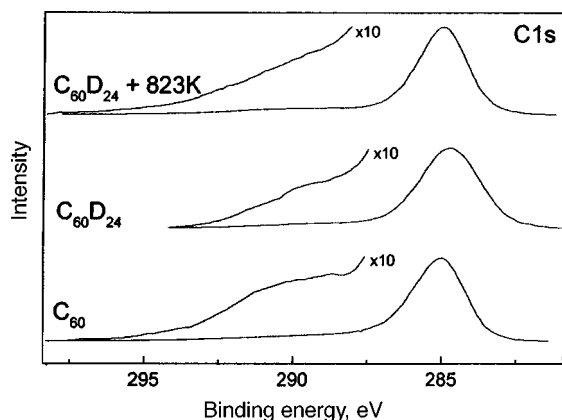
FIG. 4. XPE spectra of C_{60} fullerene, $C_{60}D_{24}$ deuteride, and the product of thermal decomposition of the deuteride.

compounds on the higher binding energy side of the main C_{1s} peak. In the case of C_{60} fullerite this satellite is ordinarily attributed to the excitation of plasma oscillations of π electrons (π plasmons). Deuteration decreases the intensity of the satellite peak and shifts the peak in the direction of the main photoelectron peak. The decrease in intensity correlates with a decrease in the number of π electrons per carbon atom. Thermal decomposition of the deuteride increases the intensity of the satellite to practically the initial state, but the shape of the satellite in PTDD differs somewhat from that in C_{60}.

In summary, our investigations established that the product of thermal decomposition of $C_{60}D_{24}$ at 823 K consists primarily of fullerene, and the distance between the C_{60} balls in it is much greater than in the initial fullerite. Similar results, but with a somewhat weaker effect, were obtained with thermal decomposition of the hydrides $C_{60}H_x$, which form during gas-phase hydrogenation of crystalline fullerite.

This work was supported by the Russian State Program ''Surface Atomic Structures'' (Project No. 95-2.7). We thank A. P. Moravskiĭ for providing the initial fullerite and V. N. Vasil'ets and V. P. Fokin for assisting in the experiments.

[a]e-mail: shulga@icp.ac.ru

[1] R. V. Fleming, A. P. Ramirez, M. J. Rosseinsky et al., Nature (London) **352**, 787 (1991).
[2] K. Tanigaki, S. Kuroshima, J. Fujita, and T. W. Ebbesen, Appl. Phys. Lett. **63**, 2351 (1993).
[3] L. E. Hall, D. R. McKenzie, M. I. Attalla et al., J. Phys. Chem. **97**, 5741 (1993).
[4] B. P. Tarasov, V. P. Fokin, A. P. Moravskiĭ, and Yu. M. Shul'ga, Izv. Akad. Nauk, Ser. Khim. (1998), at press.
[5] C. Jin, R. L. Hettich, R. N. Compton et al., J. Phys. Chem. **98**, 4215 (1994).
[6] A. G. Avent, P. R. Birkett, A. D. Darwish et al., in Fullerene and Atomic Clusters: Proceedings of the International Workshop IWFAC'95, St. Petersburg, June 19–24, 1995, p. 7.
[7] Yu. M. Shul'ga, A. P. Moravskiĭ, A. S. Lobach, and V. I. Rubtsov, JETP Lett. **55**, 132 (1992).
[8] A. M. Rao, P. C. Eklund, L. L. Hodeu et al., Phys. Rev. B **55**, 4766 (1997).
[9] J. Mizuki, M. Takai, H. Takahashi et al., Phys. Rev. B **50**, 3466 (1994).

Translated by M. E. Alferieff

Nearest-neighbor two-point correlation function of the *Z*-invariant eight-vertex model

M. Lashkevich

L. D. Landau Institute of Theoretical Physics, 142432 Chernogolovka, Moscow Region, Russia

Ya. Pugai

L. D. Landau Institute of Theoretical Physics, 142432 Chernogolovka, Moscow Region, Russia; Department of Mathematics, University of Melbourne, Parkville, Victoria 3052, Australia

The nearest-neighbor two-point correlation function of the *Z*-invariant inhomogeneous eight-vertex model in the thermodynamic limit is computed using the free-field representation. © *1998 American Institute of Physics.* [S0021-3640(98)01615-6]

PACS numbers: 05.20.−y

Recently, a free-field construction for correlation functions of the (*Z*-invariant) eight-vertex model[1,2] has been proposed[3] within the algebraic approach to integrable models of statistical mechanics.[1,4-7] The free-field representation provides explicit formulas for multipoint correlation functions on the infinite lattice. However, the resulting expressions given in terms of a certain series of multiple integrals turn out to be rather cumbersome. In this letter we give an explicit expression for the nearest-neighbor two-point correlation function in terms of a single twofold integral, and perform some checks. We also discuss the independence of the integral representations of the free parameter u_0 of the vertex–face correspondence entering into the free-field construction.[3]

Let us briefly recall the notations used in Ref. 3 (see Ref. 1 for a complete definition of the eight-vertex model). The fluctuating variables $\varepsilon = \pm 1$ are situated at edges of the
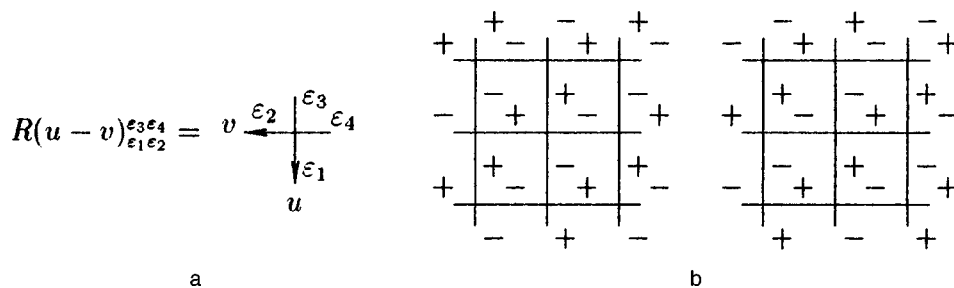

FIG. 1. a: Definition of the weight matrix; b: two degenerate ground states.

square lattice. To each configuration of variables ε_1, ε_2, ε_3, ε_4 ordered around a vertex a local Boltzmann weight $R^{\varepsilon_3\varepsilon_4}_{\varepsilon_1\varepsilon_2}$ is associated, as is shown in Fig. 1a. The nonzero Boltzmann weights can be parametrized as follows:[1]

$$R(u)^{++}_{++}=R(u)^{--}_{--}=a(u)=-i\rho(u)\,\theta_4\left(i\frac{\epsilon}{\pi};i\frac{2\epsilon r}{\pi}\right)\theta_4\left(i\frac{\epsilon}{\pi}u;i\frac{2\epsilon r}{\pi}\right)\theta_1\left(i\frac{\epsilon}{\pi}(1-u);i\frac{2\epsilon r}{\pi}\right),$$

$$R(u)^{+-}_{+-}=R(u)^{-+}_{-+}=b(u)=-i\rho(u)\,\theta_4\left(i\frac{\epsilon}{\pi};i\frac{2\epsilon r}{\pi}\right)\theta_1\left(i\frac{\epsilon}{\pi}u;i\frac{2\epsilon r}{\pi}\right)\theta_4\left(i\frac{\epsilon}{\pi}(1-u);i\frac{2\epsilon r}{\pi}\right),$$

$$R(u)^{-+}_{+-}=R(u)^{+-}_{-+}=c(u)=-i\rho(u)\,\theta_1\left(i\frac{\epsilon}{\pi};i\frac{2\epsilon r}{\pi}\right)\theta_4\left(i\frac{\epsilon}{\pi}u;i\frac{2\epsilon r}{\pi}\right)\theta_4\left(i\frac{\epsilon}{\pi}(1-u);i\frac{2\epsilon r}{\pi}\right),$$

$$R(u)^{--}_{++}=R(u)^{++}_{--}=-d(u)=-i\rho(u)\,\theta_1\left(i\frac{\epsilon}{\pi};i\frac{2\epsilon r}{\pi}\right)\theta_1\left(i\frac{\epsilon}{\pi}u;i\frac{2\epsilon r}{\pi}\right)\theta_1\left(i\frac{\epsilon}{\pi}(1-u);i\frac{2\epsilon r}{\pi}\right),$$

$$\tag{1}$$

where $\theta_j(u;\tau)$ is the standard jth theta function with the basic periods 1 and τ (Im $\tau>0$). The normalization factor $\rho(u)$ is irrelevant for correlation functions.

For definiteness, let us consider the model in the antiferroelectric phase, restricting values of the parameters ϵ, r, u to be real numbers in the region $\epsilon>0$, $r>1$, $-1<u<1$. For fixed r the parameter ϵ measures the deviation from criticality. In the limit $\epsilon \to 0$ the model has a second-order phase transition. In the "low temperature" limit $\epsilon \to \infty$ the system falls into one of two ground states (Fig. 1b) indexed by $i=0,1$.

Let $P^{(i)}_\varepsilon$ be the probability in the thermodynamic limit that the spin in the "central" edge is fixed to be ε. The label (i) indicates that spins at the edges situated "far away" from the origin are the same as in the ith ground state, so that in the low-temperature limit $\epsilon \to \infty$ the probability is nonvanishing for $\varepsilon=(-)^i$. It has been shown[3] that the one-point correlation function

$$g^{(i)}_1=\sum_\varepsilon \varepsilon P^{(i)}_\varepsilon$$

is recovered from the bosonization procedure. The resulting integral representation

$$g^{(i)}_1=(-)^{i+1}2\frac{\vartheta'_1(0)}{\vartheta_4(0)}\int_{C_0}\frac{dv}{2\pi i}\frac{h_4(v)}{h_1(v)}\tag{2}$$

can be reduced to the Baxter–Kelland formula for the spontaneous staggered polarization.[8] Here we used the notations $h_j(u)=\theta_j(u/r;i\pi/\epsilon r)$ and $\vartheta_j(u)=\theta_j(u;i\pi/\epsilon)$. The integration contour C_0 goes over the imaginary period of the theta functions (from some complex v_0 to $v_0+i\pi/\epsilon$), so that $-1<\mathrm{Re}\,v<0$.

Consider now the inhomogeneous eight-vertex model on the lattice where the spectral parameters in two adjacent rows are u_1 and u_2, respectively, while ϵ and r are the same for all sites.[2] Let $P^{(i)}_{\varepsilon_1\varepsilon_2}(u_1,u_2)$ denote the probability of the configuration with two fixed variables, as is shown in Fig. 2a. Here (i) fixes the conditions at infinity, so that $P^{(i)}_{\varepsilon_1\varepsilon_2}\to 0$ unless $\varepsilon_1=-\varepsilon_2=(-)^i$ as $\epsilon \to \infty$. The main statement of this letter is that the free-field construction[3] allows one to express the nearest-neighbor two-point correlation function
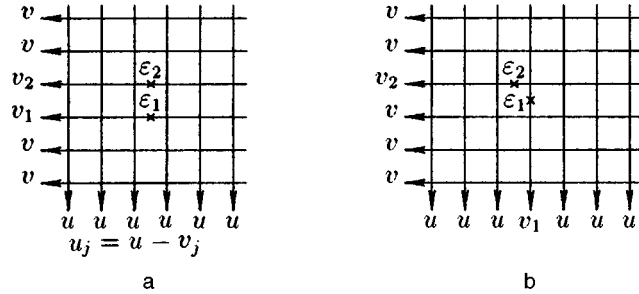
FIG. 2. Probability $P^{(i)}_{\varepsilon_1\varepsilon_2}(u_1,u_2)$. a — Definition; b — equivalent form obtained by rotating the line v_1.

$$g_2^{(i)}(u_1-u_2) \equiv \sum_{\varepsilon_1,\varepsilon_2=\pm} \varepsilon_1\varepsilon_2 P^{(i)}_{\varepsilon_1,\varepsilon_2}(u_1,u_2)$$

in terms of a twofold contour integral as follows:

$$g_2^{(i)}(u) = -2 \frac{(\vartheta_1'(0))^2}{\vartheta_4(0)} \vartheta_1(u) \frac{h_4(u)}{h_1(u)} \int_{C_1} \frac{dv_1}{2\pi i} \int_{C_2} \frac{dv_2}{2\pi i} \frac{\vartheta_4(v_1+v_2-u)}{\vartheta_1(v_1-u)\vartheta_1(v_2-u)}$$

$$\times \vartheta_1(v_1-v_2) \frac{h_4(v_1-v_2+1)}{h_1(v_1-v_2+1)} \prod_{j=1}^{2} \frac{1}{\vartheta_1(v_j)} \frac{h_1(v_j)}{h_4(v_j)}. \tag{3}$$

The integration contours $C_{1,2}$ go over the same imaginary period as C_0, so that $-1 < \operatorname{Re} v_1 < u < \operatorname{Re} v_2 < 1$, $\operatorname{Re} v_2 - \operatorname{Re} v_1 < 1$.

Briefly, to get this formula we applied the standard procedure of computing traces of bosonic operators over Fock spaces[7] and then proceeded as in the one-point function case (see Appendix D of Ref. 3) by applying various identities for theta functions to provide summation over the variables of the related solid-on-solid model, including infinite summation over Fock spaces. We will not go into the technical details of this procedure, since they are more cumbersome than instructive.

Let us only make a remark on the free parameter u_0 in the free-field representation.[3] Although the explicit formulas for the correlation functions in terms of traces of bosonic fields do contain u_0, it is evident on physical grounds that the correlation functions must be independent of u_0. Since the free-field representation is based on certian assumptions, it is important to prove this statement for the resulting integral representations for the correlation functions. It can be easily checked that these expressions are nonvanishing doubly periodic meromorphic functions of u_0 with two generically incommensurate real periods 2 and $2r$, which proves their independence of u_0. We used the fact that $g_2^{(i)}$ is independent of u_0 to fix $u_0 = u_2 + i\pi/2\epsilon$ in Eq. (3). In addition, to make sure, we also obtained the formula for $g_2^{(i)}$ with general u_0 (which turns out to be more cumbersome) and checked numerically that it does not depend on u_0.

To support the validity of the integral representation (3) we compared it with the known results.

• The partition function differentiation method (Ref. 2).[a] The probabilities $P^{(i)}_{\varepsilon_1 \varepsilon_2}$ $\times (u_1, u_2)$ are equal to those shown in Fig. 2b because of the Z invariance. So the correlation function $g_2^{(i)}(u)$ can be calculated as

$$g_2^{(i)}(u) = \left(a \frac{\partial}{\partial a} - b \frac{\partial}{\partial b} - c \frac{\partial}{\partial c} + d \frac{\partial}{\partial d} \right) \log \kappa(a,b,c,d)|_{u,\epsilon,r}. \tag{4}$$

Here κ is the partition function per site as a function of the Boltzmann weights,[1]

$$\log \kappa(a,b,c,d) = \log(c+d) + \sum_{m=1}^{\infty} \frac{(x^{3m} - p^{m/2})(1 - p^{m/2} x^{-m})(x^m + x^{-m} - z^m - z^{-m})}{m(1-p^m)(1+x^{2m})}$$

with $x = e^{-\epsilon}$, $p = x^{2r}$, $z = e^{\epsilon(1-2u)}$, and the derivatives are taken at the point characterized by the parameters u, ϵ, r according to Eq. (1).

We checked numerically that the results of (3) and (4) coincide at least up to the fifth decimal place over a wide range of values of ϵ and r.

• The limiting case $r \to \infty$. In this limit the Boltzmann weights (1) become those of the six-vertex model in the antiferroelectric regime. The integral representation for the correlation functions of the antiferroelectric six-vertex model is known.[9,5] Analytically formula (3) gives another integral representation in this limit, but numerically the results of integration according to the two formulas coincide up to the sixth decimal digit.

• The limiting case $\epsilon \to 0$. This is the critical region of the eight-vertex model. Using the Baxter duality transformation for the Boltzmann weights[1] one can map the model in this region onto the six-vertex model in the gapless regime, whose correlation functions were found in Ref. 10 (see also Ref. 11). Performing the duality transform at the level of correlation functions,[12] one has to compare our answer with the following correlation function:

$$g_2^{JM}(\beta_1 - \beta_2) \equiv -2\langle E^{(1)}_{-+} E^{(2)}_{+-} \rangle (\beta_1, \beta_2)$$

in the notation of Ref. 10 with the identification $\nu = 1/r$, $\beta_j = i\pi u_j$. The integral representation for this quantity can be written as[10]

$$g_2^{JM}(\beta) = -2 \frac{\sinh \beta}{\sinh \nu \beta} \int_{C_-} \frac{dv_1}{2\pi i} \int_{C_+} \frac{dv_2}{2\pi i} \frac{1}{\sinh(v_1 - \beta)\sinh(v_2 - \beta)} \frac{\sinh(v_1 - v_2)}{\sinh \nu(v_1 - v_2 + i\pi)}$$

$$\times \prod_{j=1}^{2} \frac{\sinh \nu v_j}{\sinh v_j}. \tag{5}$$

Here the contours $C_\pm$ are from $-\infty$ to $+\infty$. They are chosen in such a way that $\beta + \pi i$ (resp. β) is above (resp. below) C_+ and β (resp. $\beta - \pi i$) is above (resp. below) C_-. By checking it directly one shows that the limit $\epsilon \to 0$ of Eq. (3) coincides with Eq. (5).

• The $r = 2$ case. With this specification the eight-vertex model is equivalent to two noninteracting Ising models.[1] In this case $-g_2^{(i)}$ coincides with the nearest-neighbor diagonal correlator of the inhomogeneous (Z-invariant) Ising model in the ferromagnetic regime[13] (see also Refs. 2, 14, and 15),

$$-g_2^{(i)}(u)=\langle\sigma_{m,n}\sigma_{m+1,n+1}\rangle=\frac{1}{\pi}\frac{\theta_4\left(0;i\frac{2\epsilon}{\pi}\right)}{\theta_3\left(0;i\frac{2\epsilon}{\pi}\right)}\frac{\theta_2'\left(i\frac{\epsilon}{\pi}u;i\frac{2\epsilon}{\pi}\right)}{\theta_1\left(i\frac{\epsilon}{\pi}u;i\frac{2\epsilon}{\pi}\right)},\tag{6}$$

where $\sigma_{m,n}$ is the spin variable at the site (m,n) of the square lattice. As we show in the Appendix, Eq. (3) reduces to this formula at $r=2$.

We hope that a similar integral representation can be obtained starting from the free-field representation for other multipoint correlation functions, in particular, for two-point functions with a separation of 2 lattice sites or more. It would be also very interesting to understand whether the elliptic algebra approach proposed in Refs. 16 would lead to another bosonization prescription and give a direct procedure for obtaining the integral representations of the correlation functions of the eight-vertex model.

APPENDIX A:

Let us obtain (6) from (3) in the Ising model case $r=2$. The integrand of (3) is antisymmetric with respect to the permutation of v_1 and v_2. This allows one to perform the second integration simply by taking the residues at the pole $v_2=u$. Using the identity

$$\frac{\vartheta_4(u)}{\vartheta_1(u)}\frac{h_1(u)}{h_4(u)}=\frac{\vartheta_4(0)}{\vartheta_1'(0)}\frac{h_1'(0)}{h_4(0)}\frac{h_1(1)}{h_4(1)}\frac{h_4(u+1)}{h_1(u+1)}\quad\text{(for }r=2\text{)},$$

which is valid for $r=2$, the resulting expression can be represented in the following form

$$g_2^{(i)}(u)=2\frac{h_1'(0)}{h_4(0)}\frac{h_1(1)}{h_4(1)}J(u),\quad J(u)=\int_{C_1}\frac{dv}{2\pi i}\frac{h_4(v+1)h_4(v-u+1)}{h_1(v+1)h_1(v-u+1)}.\tag{A1}$$

The function $J(u)$ has the following defining properties:

$$J\left(u+\frac{i\pi}{\epsilon}\right)=J(u),\quad J(-u)=J(u),\quad J\left(\frac{i\pi}{2\epsilon}\right)=\frac{1}{2\epsilon},$$

$$J(u+2)=-J(u)+\frac{h_4(u)h_4(0)}{h_1(u)h_1(0)},$$

and regularity of $J(u)$ on the strip $-2<\mathrm{Re}\,u<2$, which fix it completely to be

$$J(u) = -\frac{1}{2\epsilon} \frac{\theta_2\left(0, i\frac{2\epsilon}{\pi}\right)}{\theta_1'\left(0, i\frac{2\epsilon}{\pi}\right)} \frac{\theta_2'\left(i\frac{\epsilon}{\pi}u; i\frac{2\epsilon}{\pi}\right)}{\theta_1\left(i\frac{\epsilon}{\pi}u; i\frac{2\epsilon}{\pi}\right)}.$$

Passing to the conjugate module in the coefficient at $J(u)$ in Eq. (A1), one gets (6).

[a] We would like to thank Prof. J. H. H. Perk for pointing out to us the possibility of this check.

[1] R. J. Baxter, *Exactly Solved Models in Statistical Mechanics*, Academic Press, 1982.

[2] R. J. Baxter, Philos. Trans. R. Soc. London **289**, 315 (1978).

[3] M. Lashkevich and Ya. Pugai, Nucl. Phys. B **516**, 623 (1998) [http://xxx.lanl.gov/abs/hep-th/9710099].

[4] B. Davies, O. Foda, M. Jimbo *et al.*, Commun. Math. Phys. **151**, 89 (1993).

[5] M. Jimbo and T. Miwa, *Algebraic Analysis of Solvable Lattice Models*, CBMS Regional Conf. Series in Mathematics **85**, AMS, 1994.

[6] M. Jimbo, T. Miwa, and A. Nakayashiki, J. Phys. A **26**, 2199 (1993).

[7] S. Lukyanov and Ya. Pugai, Nucl. Phys. B [FS] **473**, 631 (1996) [http://xxx.lanl.gov/abs/hep-th/9602074].

[8] R. J. Baxter and S. B. Kelland, J. Phys. C **7**, L403 (1974).

[9] M. Jimbo, K. Miki, T. Miwa, and A. Nakayashiki, Phys. Lett. A **168**, 256 (1992).

[10] M. Jimbo and T. Miwa, J. Phys. A **29**, 2923 (1996) [http://xxx.lanl.gov/abs/hep-th/96011135].

[11] S. Lukyanov, Commun. Math. Phys. **167**, 183 (1995) [http://xxx.lanl.gov/abs/hep-th/9307196]; Phys. Lett. B **325**, 409 (1994) [http://xxx.lanl.gov/abs/hep-th/9311189].

[12] M. Yu. Lashkevich, Phys. Lett. B **10**, 101 (1996) [http://xxx.lanl.gov/abs/hep-th/9408131].

[13] R. J. Baxter and I. G. Enting, J. Phys. A **11**, 2463 (1978).

[14] O. Foda, M. Jimbo, T. Miwa *et al.*, J. Math. Phys. **35**, 13 (1994).

[15] J. R. Reyes Martinez, Phys. Lett. A **227**, 203 (1997) [http://xxx.lanl.gov/abs/hep-th/9609135].

[16] M. Jimbo, H. Konno, S. Odake, and J. Shiraishi, http://xxx.lanl.gov/abs/q-alg/9712029; M. Jimbo, H. Konno, S. Odake, and J. Shiraishi, http://xxx.lanl.gov/abs/q-alg/9802002.

Experimental scheme for quantum teleportation of a one-photon packet

S. N. Molotkov

Institute of Solid-State Physics, Russian Academy of Sciences, 142432 Chernogolovka, Moscow Region, Russia

A complete protocol and an optical scheme for experimental implementation of the quantum teleportation of an unknown one-photon wave packet are proposed. © *1998 American Institute of Physics.*
[S0021-3640(98)01715-0]

PACS numbers: 03.67.Hk

Quantum mechanics forbids the cloning (copying) of an unknown quantum state (the no cloning theorem[1]). Is it possible to transmit to a distant user an a priori unknown quantum state without transmitting the state itself? Any measurement performed to obtain classical information about the state for subsequent transmission of this information, generally speaking, changes the state itself without giving complete information about it. The preparation of multiple copies followed by measurements on the copies to obtain exhaustive information is forbidden by the no cloning theorem. Therefore it is impossible to transmit information about an unknown quantum state using only transmission of information along a classical communication channel.

Quantum teleportation removes this restriction, if a quantum communication channel is used in addition to a classical channel. The idea of quantum teleportation for the case of quantum states described by a discrete variable, specifically, for a spin-1/2 particle in an unknown state, was advanced in Ref. 3. Nonlocal EPR[a] correlations are used as the quantum channel.[2,3] The EPR pair is a pair of particles in an entangled state. Entanglement entails a special type of quantum correlations which have no classical analog.

The quantum teleportation protocol proposed in Ref. 4 is as follows. To teleport an *a priori* unknown quantum state which user *A* possesses to a distant user *B*, user *A* generates an EPR pair. One particle of the EPR pair remains with *A*, while the second particle is directed toward the distant user *B*. User *A* performs on the remaining second particle of the EPR pair and on the particle in the unknown state a simultaneous measurement whose outcome yields classical information. Since nonlocal quantum correlations exist initially in the EPR pair, the measurement attaches the state of the unknown particle to the second particle of the EPR pair at the user *B*. The state of the second particle is identical, to within a unitary rotation, to the unknown state. The classical information obtained in the measurement is transmitted by user *A* to user *B* and indicates to user *B* which unitary transformation must be performed in order to obtain the new
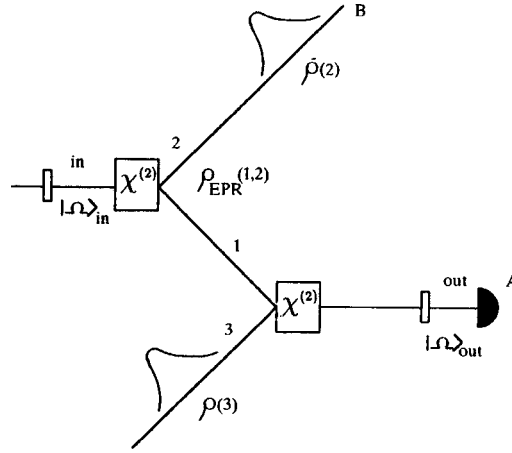
FIG. 1.

state, which will now be an exact copy of the initial unknown state. In the teleportation process the user A does not obtain any information about the unknown teleported state.

Quantum teleportation was recently demonstrated experimentally for a photon in a state with unknown polarization.[5,6]

The question of teleportation of the wave function of a particle in the one-dimensional case, where the continuous dynamical variables are the coordinate and momentum, was investigated in Ref. 7, where a wave function of the form in Ref. 2 was used as the wave function of the EPR pair. Quantum teleportation of a quantum state described by the dynamical variables (x,p) for the case of nonideal EPR correlations was investigated in a recent work[8] (the unknown state in Ref. 8 corresponds to a one-mode state of a photon). A quadratically squeezed state was used as the EPR state, while the homodyne detection procedure essentially corresponded to a measurement.

In the present letter a new scheme (the complete protocol and experimental implementation) is proposed for teleportation of a multimode state — a one-photon wave packet — using an EPR pair in an entangled state in terms of energy–time variables.

To further simplify the formulas we shall assume that the polarization state of the packet is known. The following arguments are also valid for the case of unknown polarization, which can be taken into account by introducing an additional index. The state of a one-photon wave packet can be represented in the form (see, for example, Ref. 9)

$$|1\rangle_3 = \int_0^\infty d\omega\, f(\omega)\hat{a}^+(\omega)|0\rangle = \int_0^\infty d\omega\, f(\omega)|\omega\rangle_3, \tag{1}$$

$$[\hat{a}(\omega),\hat{a}^+(\omega')] = I\delta(\omega-\omega'), \quad \int_0^\infty |f(\omega)|^2 d\omega = 1,$$

where $\hat{a}^+(\omega)$ and $\hat{a}(\omega)$ are creation and annihilation operators of a one-mode Fock state $|\omega\rangle_3$, $|0\rangle$ is the vacuum state, and $f(\omega)$ is the amplitude of the packet. The index 3 indicates the number of the channel (see Fig. 1). The density matrix at an arbitrary

moment in time has the form

$$\rho(3) = \left(\int_0^\infty d\omega e^{-i\omega t} f(\omega) |\omega\rangle_3 \right) \left(\int_0^\infty d\omega_3' \langle\omega| e^{i\omega' t} f^*(\omega') \right). \tag{2}$$

The state of the EPR photon pair in our case can be represented in the form (similar EPR photon pairs are obtained in downward (in energy) parametric conversion processes[10])

$$|\psi_{\text{EPR}}\rangle_{1,2} = \int_0^\infty d\omega |\omega\rangle_1 \otimes |\Omega - \omega\rangle_2, \quad \rho_{\text{EPR}}(1,2) = |\psi_{\text{EPR}}\rangle_{1,2} \,_{1,2}\langle\psi_{\text{EPR}}|, \tag{3}$$

where Ω is the pump frequency and the indices 1, 2 enumerate the channels (see Fig. 1). The normalization of the state (3) is immaterial for what follows.

According to the general scheme of Refs. 11–13, quantum-mechanical measurements are described by positive operators which realize a decomposition of unity. The measurements of observables, which correspond to self-conjugate operators, correspond to orthogonal decompositions of unity. The parameters (time, rotation angle) do not correspond to any self-conjugate operators, so that such measurements are described by nonorthogonal decompositions of unity.[11–13]

The idea of teleportation in application to the present case consists in using entangled measurements of energy–time for a pair of photons, one from an EPR pair and a photon in an unknown state. A measurement is given by a nonorthogonal decomposition of unity:[14]

$$\int \int M(dt d\Omega_+) = \int \int R^+ R (dt d\Omega_+) = I, \tag{4}$$

where R is the "reduction" operator, $M(dt d\Omega_+)$ describes a quantum operation and is a positive-definite operator measure — POVM (for the details see, for example, Refs. 15 and 16). We have[14]

$$M(dt d\Omega_+) = \left(\int d\omega_- e^{i\omega_- t} |\omega_+ + \omega_-\rangle_1 \otimes |\omega_+ - \omega_-\rangle_3 \right)$$

$$\times \left(\int d\omega_-' e^{-i\omega_-' t} \,_3\langle\omega_+ - \omega_-'| \otimes \,_1\langle\omega_+ + \omega_-'| \right) \frac{dt d\omega_+}{2\pi}, \tag{5}$$

where $\omega_\pm = \Omega_\pm / 2$. The integration extends over the frequencies at which the arguments in the Fock states are positive. Note that the frequency ω_+ is a common frequency in the bra and ket states.

According to the general ideology of quantum-mechanical measurements,[10–13,15,16] the application of a quantum operation (measurement) to a system with density matrix ρ transfers the system into a new state

$$\rho \rightarrow R_i \rho R_i^+ / \text{Tr}\{R_i \rho R_i^+\}.$$

The probability of the i-th outcome is given by the formula $\text{Pr} = \text{Tr}\{R_i \rho R_i^+\}$, where $E_i = R_i^+ R_i$ is the POVM element.

In our case, after a measurement by user A the state of the second photon from the EPR pair at user B is given by the density matrix

$$\widetilde{\rho}(2) = \frac{\mathrm{Tr}_{1,3}\{\rho_{\mathrm{EPR}}(1,2)\otimes\rho(3)M(dtd\Omega_+)\}}{\mathrm{Pr}\{dtd\Omega_+\}}, \tag{6}$$

$$\mathrm{Pr}\{dtd\Omega_+\} = \mathrm{Tr}_{1,2,3}\{\rho_{\mathrm{EPR}}(1,2)\otimes\rho(3)M(dtd\Omega_+)\}, \tag{7}$$

$$\widetilde{\rho}(2) = \left(\int d\omega e^{-i(\Omega_+/2+\omega)t}f(\Omega_+-\omega)|\Omega-\omega\rangle_2\right)$$
$$\times\left(\int d\omega' e^{i(\Omega_+/2+\omega')t}{}_2\langle\Omega-\omega'|f^*(\Omega_+-\omega')\right). \tag{8}$$

Formally, the measurement (4) corresponds to the situation where the moment t of the measurement and the frequency Ω_+ are chosen by the experimenter, and the probability of a positive outcome of such a measurement is given by Eq. (7). Teleportation will be ideal if $\Omega_+=\Omega$ is chosen (the detection frequency ω_+ of the detector equals the pump frequency Ω). In this case, as follows from Eq. (6), the state $\widetilde{\rho}(2)$ is identical to $\rho(3)$ to within a phase factor, which can be eliminated by the user B if A reports to B along a classical channel the moment t of detection. We note that if $\Omega_+=\Omega$, the moment t of detection does not depend on the unknown state $\rho(3)$.

Physically, the measurement (4) can be understood as follows. The user A possesses a continuum of detectors which are ''tuned'' to frequencies in the interval $(0,\infty)$ and each of which can be triggered at an arbitrary moment t in time, formally, from $(-\infty, +\infty)$. The probability that a detector at frequency Ω_+ is triggered at a certain moment t is given by formula (7). The triggering probability is time-independent (equally likely at any moment in time) only for one detector, tuned to the frequency Ω. Teleportation will be ideal only in the case that the detector at the frequency Ω is triggered. As follows from Eq. (7), the triggering probability does not depend on the unknown input state. The user A does not obtain any information about the teleported state.

Since measurements can be performed at spatially separated points, the times in the formulas should be understood to be the times presented minus the time of flight ($t\to t -x/c$). As will be seen below, this will not be important in the case of ideal teleportation.

The main difficulty in realizing teleportation of a one-phonon packet lies in realizing the measurement (4). The measurement (4) on a photon pair is intermediate between a measurement of time and frequency. An experimental implementation of this measurement is proposed below. The idea is to convert the photon pair into one photon on which a measurement is performed with an narrow-band photodetector. The latter can be realized experimentally quite simply.

The experimental arrangement is shown in Fig. 1. The first nonlinear crystal with second-order susceptibility χ and a narrow-band filter at frequency Ω serve to generate the EPR pair in channels 1 and 2. An unknown one-photon packet enters the channel 3. The one-photon packet can be prepared by exciting a two-level system with a π pulse in the distant past. The second nonlinear crystal, a narrow-band filter at frequency Ω following it, and then an ordinary photodetector implement the measurement (4). A teleported state appears in channel 2.

Let us consider in succession the evolution of the input states through the optical scheme. The state after the first narrow-band filter in front of the first nonlinear crystal is described by a monochromatic state with density matrix

$$\rho_{in}(in) = |\Omega\rangle_{in\ in}\langle\Omega|, \tag{9}$$

which can be obtained by using the first filter to cut a narrow band out of an auxiliary one-photon packet fed into the entrance *in* (Fig. 1). The interaction of the photons in the nonlinear crystal is described by the Hamiltonian in the interaction representation (see details in Refs. 17 and 18):

$$H_1(t) = \chi \int d\mathbf{x} E_{in}^{(+)}(\mathbf{x},t) E_1^{(-)}(\mathbf{x},t) E_2^{(-)}(\mathbf{x},t) + \text{h.c.}, \tag{10}$$

where all nonessential constants are included in the definition of χ, which, as is ordinarily done,[17,18] will be assumed to be frequency-independent. For what follows, it is convenient to represent the electric-field operators in the form[9]

$$E_i^{(-)}(\mathbf{x},t) = \frac{1}{\sqrt{2\pi}} \int_0^\infty d\omega e^{i(\omega t - \mathbf{kx})} \hat{a}^+(\omega)|0\rangle_i = \frac{1}{\sqrt{2\pi}} \int_0^\infty d\omega e^{i(\omega t - \mathbf{kx})}|\omega\rangle_i, \tag{11}$$

where i is the channel number. We proceed similarly for $E_i^{(+)} = (\mathbf{x},t)$ also. Taking account of Eq. (11) we have

$$H_1(t) = \frac{\chi}{(2\pi)^{3/2}} \int \int \int d\omega_1 d\omega_2 d\omega_{in} e^{it(\omega_1 + \omega_2 - \omega_{in})}|\omega_1\rangle_1$$

$$\otimes |\omega_2\rangle_{2\ in}\left\langle \omega_{in}\right| \int_{vol} d\mathbf{x} e^{-i\mathbf{x}(\mathbf{k}_1 + \mathbf{k}_2 - \mathbf{k}_{in})} + \text{h.c.} \tag{12}$$

The second integral extends over the volume of the crystal. This gives a δ-function of the momenta, and leads to the phase matching condition[18] ($\mathbf{k}_1 + \mathbf{k}_2 = \mathbf{k}_{in}$), which we shall assume to hold (in what follows, this means that $\mathbf{k}_2 \| \mathbf{k}_3$; see Fig. 1). Next, χ is taken to be the renormalized value taking account of the additional factors from the second integral. The first-order susceptibility, which is always present, can be neglected for our purposes, since the terms in the Hamiltonian which are associated with it do not contribute in the *out* channel.

The state after the first crystal in channels 1 and 2 is described by the density matrix

$$\rho_{EPR}(1,2) = S(t)\rho_{in}(in)S^{-1}(t), \tag{13}$$

where $S(t)$ is the S matrix

$$S(t) = e^{i\int_{-\infty}^t H_1(t')dt'} = 1 + S^{(1)} + S^{(2)} + \ldots. \tag{14}$$

In first order in χ we have

$$S^{(1)} = i\chi \int \int d\omega_1 d\omega_{in}|\omega_1\rangle_1 \otimes |\omega_{in} - \omega_1\rangle_{2\ in}\langle\omega_{in}| + \text{h.c.} \tag{15}$$

The upper integration limit in the exponential in S can be replaced by ∞. Physically, this is related essentially with the fact that the entrance state is monochromatic (roughly

speaking, infinitely extended in time), and the teleportation process is formally stationary. To within the normalization, which is unimportant, the state in channels 1 and 2 can be described by the density matrix

$$\rho_{\text{EPR}}(1,2) = \chi^2 \left(\int_0^\infty d\omega |\omega\rangle_1 \otimes |\Omega - \omega\rangle_2 \right) \left(\int_0^\infty d\omega'_1 \langle \omega'|\otimes_2 \langle \Omega - \omega'| \right). \tag{16}$$

A measurement by the photodetector, in front of which a narrow-band at frequency Ω is installed, is formally described by the projector $P(\Omega) = |\Omega\rangle_{out\ out}\langle\Omega|$.

The teleported state in channel 2 after detection by the photodetector is described by the density matrix (once again, to within the normalization)

$$\tilde{\rho}(2) = \text{Tr}_{out}\{S(t)\rho_{in}(in) \otimes \rho(3)S^{-1}(t)P(\Omega)\}, \tag{17}$$

where $S(t)$ is now the complete S matrix of the entire optical scheme:

$$S(t) = \exp\left\{ i \int_{-\infty}^t [H_1(t') + H_2(t')]dt' \right\} = 1 + S^{(1)} + S^{(2)} + \ldots, \tag{18}$$

where $H(t)_2$ is the Hamiltonian for the second nonlinear crystal, which to within a replacement of the indices is similar to $H(t)_1$ in Eq. (12). The S-matrix terms of the form

$$S^{(2)} \propto \chi^2 \left(\int \int d\omega_1 d\omega_{in} |\omega_1\rangle_1 \otimes |\omega_{in} - \omega_1\rangle_{2\ in}\langle\omega_{in}| \right)$$

$$\times \left(\int \int d\omega'_1 d\omega_{out} |\omega_{out}\rangle_{out\ 1}\langle\omega'_3| \otimes_{in}\langle\omega_{out} - \omega'_1| \right) \tag{19}$$

contribute to the teleportation process. Taking account of Eq. (19), the density matrix in channel 2 is identical, to within the normalization, to the initial density matrix of the unknown wave packet:

$$\tilde{\rho}(2) = \chi^4 \left(\int_0^\infty d\omega f(\omega) |\omega\rangle_3 \right) \left(\int_0^\infty d\omega'_3 \langle\omega| f^*(\omega') \right). \tag{20}$$

It also follows from Eq. (17) that the detection probability in the *out* channel does not depend on the unknown state and is proportional to

$$\text{Pr} = \text{Tr}_{2,out}\{S(t)\rho_{in}(in) \otimes \rho(3)S^{-1}(t)P(\Omega)\} \propto \chi^4. \tag{21}$$

In this scheme the classical channel is necessary to report to a distant user the fact that a photodetector has been triggered; in this case teleportation is considered to be successful. The probability (efficiency) of the teleportation process is small to the degree that χ^4 is small. On account of the terms in the S matrix which are of next higher-order in χ in the S matrix, the fraction of spurious photodetector triggerings for which an incorrect state will be teleported is small additionally with respect to the parameter χ^2. We note that formally the teleportation process is stationary (it lasts for an infinitely long time), since it is necessary to prepare a monochromatic input state. In this case the probability of detection by a photodetector in the *out* channel is the same at any moment in time and does not depend on the input state. It is obvious that in this case user A possesses zero information about the teleported state.

Of course, quantum teleportation does not permit transmitting information faster than the speed of light. In this scheme the intuitive and qualitative explanation reduces to the following. Since the input state is monochromatic and, as is always surmised intuitively, is nonlocalized (infinitely extended), the latter fact signifies that the field is seemingly ''preprepared'' in all space, including ''preprepared'' for the spatially distant users *A* and *B* also. A measurement by user *A* transfers the entire system into a new state — it reduces the state vector ''immediately'' and ''everywhere'' for the entire system. Usually, this part is regarded as intuitively unnacceptable. However, this ''immediately'' and ''everywhere'' does not make it possible to transmit information faster than the speed of light. To transmit classical information from *A* to *B* by means of a teleported state, a classical channel from *A* to *B* is required in order to report that the detector has been triggered and teleportation has taken place. The classical communication channel presupposes that a classical object is transmitted from *A* to *B*; the velocity of the object cannot exceed the velocity of light. The question of whether the field is ''preprepared'' is everywhere closely related with the question of photon localizability (more accurately, nonlocalizability) (see, for example, Refs. 19–23). As far as is known, this question has not yet been discussed in detail in the context of quantum teleportation.

We note that the teleportation process can be reformulated in terms of a diagrammatic technique. The averaging is performed not over the ground state, but rather over a ''stationary'' state $|\Omega\rangle \otimes \int_0^\infty d\omega f(\omega)|\omega\rangle$ — the input monochromatic state and the state of a one-phonon packet. In the case of ideal teleportation, such a state is also an output state. In this sense the process is stationary, and the averaging is performed with respect to this stationary state, which need not be the ground state. In this case the diagrammatic technique is constructed similarly to the way this is done in the Keldysh method.[24]

---

[a] The name originates from the well-known Einstein–Podolsky–Rosen effect.[2]

---

[1] W. K. Wootters and W. H. Zurek, Nature (London) **299**, 802 (1982).

[2] A. Einstein, B. Podolsky, and N. Rosen, Phys. Rev. **47**, 777 (1935).

[3] J. S. Bell, *Speakable and Unspeakable in Quantum Mechanics*, Cambridge University Press, Cambridge, England, 1988.

[4] C. H. Bennett, G. Brassard, C. Crepeau *et al.*, Phys. Rev. Lett. **70**, 1895 (1993).

[5] B. Boumeester, Jian-Wei Pan, K. Mattle *et al.*, Nature (London) **390**, 575 (1997).

[6] D. Boschi, S. Branca, F. De Martini *et al.*, Phys. Rev. Lett. **80**, 1121 (1998).

[7] L. Vaidman, Phys. Rev. A **49**, 1473 (1994).

[8] S. Braunstein and H. J. Kimble, Phys. Rev. Lett. **80**, 869 (1998).

[9] R. A. Campos, B. E. A. Saleh, and M. C. Teich, Phys. Rev. A **42**, 4127 (1990).

[10] P. G. Kwait, K. Mattle, H. Weinfurter *et al.*, Phys. Rev. Lett. **75**, 4337 (1995).

[11] A. S. Kholevo, *Probabilistic and Statistical Aspects of Quantum Theory* [in Russian], Nauka, Moscow, 1980.

[12] P. Busch, M. Grabowski, and P. J. Lahti, *Operational Quantum Physics*, Springer Lecture Notes in Physics **31**, 1995.

[13] K. Krauss, *States, Effects and Operations*, Springer-Verlag, Berlin, 1983.

[14] S. N. Molotkov, http://xxx.lanl.gov/abs/quant-ph/9805045.

[15] B. W. Schumacher, Phys. Rev. A **54**, 2614 (1996).

[16] M. A. Nielsen and C. M. Caves, Phys. Rev. A **55**, 2547 (1997).

[17] C. K. Hong and L. Mandel, Phys. Rev. A **31**, 2409 (1985).
[18] P. W. Milonni, H. Fearn, and A. Zeilinger, Phys. Rev. A **53**, 4556 (1996).
[19] T. D. Newton and E. P. Wigner, Rev. Mod. Phys. **21**, 400 (1949).
[20] A. S. Wightman, Rev. Mod. Phys. **34**, 845 (1962).
[21] K. Kraus, in *The Uncertainty Principle and Foundations of Quantum Mechanics*, edited by W. C. Price and S. S. Chissik, Wiley, New York, 1976, p. 293.
[22] H. Bacry in *Lecture Notes in Physics,* edited by H. Araki *et al.*, Springer-Verlag, Berlin, Vol. 308, 1988.
[23] J. A. Brooke and F. E. Schroek, J. Math. Phys. **37**, 5958 (1996).
[24] L. V. Keldysh, Zh. Éksp. Teor. Fiz. **47**, 1515 (1964) [Sov. Phys. JETP **20**, 1018 (1965)].

Translated by M. E. Alferieff